

Journal of Advanced Materials and Processing

Islamic Azad University - Najafabad Branch

Founder: Islamic Azad University - Najafabad Branch

Editor-in-Chief: Dr. Reza Ebrahimi-Kahrizangi Islamic Azad University, Najafabad Branch

Managing Editor: Dr. Masood Kasiri Islamic Azad University, Najafabad Branch

Executive manager: Dr. Hamid Reza Bakhsheshi-Rad Islamic Azad University, Najafabad Branch

Editorial Board:

Dr. Constantin Politis	(Professor of Physics and Materials Science, University of Patras, Greece)
Dr. Seeram Ramakrishna	(Professor of Mechanical Engineering, National University of Singapore)
Dr. Mohd Sapuan b. Salit	(Professor Of Mechanical And Manufacturing Engineering, Universiti Putra Malaysia)
Dr. Mehdi Rafiei	(Associate Professor, Department of Materials Engineering, Najafabad Branch, Islamic Azad University, Najafabad, Iran)
Dr. Reza Ebrahimi-Kahrizangi	(Professor, Department of Materials Engineering, Najafabad Branch, Islamic Azad University, Najafabad, Iran)
Dr. Masoud Kasiri	(Associate Professor, Department of Materials Engineering, Najafabad Branch, Islamic Azad University, Najafabad, Iran)
Dr. Hamid Ghayour	(Associate Professor, Department of Materials Engineering, Najafabad Branch, Islamic Azad University, Najafabad, Iran)
Dr. Seyed Ali Hasanzadeh Tabrizi	(Associate Professor, Department of Materials Engineering, Najafabad Branch, Islamic Azad University, Najafabad, Iran)
Dr. Ahmad Saatchi	(Professor of Materials Engineering, Isfahan University of Technology, Iran)
Dr. Abbas Najafizadeh	(Professor of Materials Engineering, Isfahan University of Technology, Iran)
Dr. Ali Saidi	(Professor of Materials Engineering, Isfahan University of Technology, Iran)
Dr. Hossein Edris	(Associate Professor of Materials Engineering, Isfahan University of Technology, Iran)
Dr. Ali Shafyey	(Associate Professor of Materials Engineering, Isfahan University of Technology, Iran)
Dr. Ebrahim Heshmat Dehkordi	(Associate Professor of Materials Engineering, Atomic Energy Agency of Iran)
Dr. Ramin Ebrahimi	(Professor of Materials Engineering, Shiraz University, Iran)
Dr. Saeed Karbasi	(Professor of Tissue Engineering, Department of Biomaterials, Nanotechnology and Tissue Engineering, School of Advanced Medical Technology, Isfahan University of Medical Sciences, Isfahan, Iran)
Dr. Saheb Ali Manafi	(Professor, Department of Materials Engineering, Shahrood Branch, Islamic Azad University, Shahrood, Iran)
Dr. Behzad Niroomand	(Professor, Department of Materials Engineering, Isfahan University of Technology, Isfahan, Iran)
Dr. Farid Jamali Sheini	(Professor, Department of Physics, Ahvaz Branch, Islamic Azad University, Ahvaz, Iran)

Journal of Advanced Materials and Processing

Vol.9, No.1, Winter 2021.

P-ISSN: 2322-388X

E-ISSN: 2345-4601

Publisher: Najafabad Branch, Islamic Azad University, Iron and Steel Association of Iran

Production manager: Mostafa Salehi

Executive assistant: Leily Rezaei, Seyedeh Razieh Anvari

Address: Journal of Advanced Materials and Processing

Department of Materials Engineering, Najafabad Branch, Islamic Azad University, Najafabad, Isfahan, Iran

P.O. Box: 517

Tel:+98-31-42292512 **Fax:**+98-31-42291008

Website: www.jmatpro.iaun.iau.ir

Email: jmatpro@iaun.ac.ir

Table of Content

✎ **Dissimilar DP780/DP980 Resistance Spot Welded Joints: Microstructure, Mechanical Properties and Critical Diameter3-10**

Bahman Valizadeh, Mehdi Mansouri

✎ **Preparation and Determination of the Characteristics of Hydrogel Membrane of Poly-Vinyl Alcohol, Starch and Chitosan11-20**

Shaghayegh Baghaie, Mohammad T. Khorasani, Ali Zarrabi, Jamal Moshtaghia

✎ **Fabricating the Tribological Properties and Investigating of Ni₃Al-MoS₂ Composite Coating....21-30**

Mahdi Mirzaaghaei, Mohammad-Hossein Enayati, Mahdi Ahmadi

✎ **Influence of Power Law Distribution with Pressure on the Frequencies of Supported Functionally Graded Material Cylindrical Shell with C-SL and F-SS Boundary Conditions31-38**


Mohammadreza Isvandzibaei

✎ **Nanoporous Carbon Spheres Derived from the Leather Leaf as Electrode Materials for Supercapacitors39-48**

Azam Asadi, Hamid Oveisi

✎ **Effect of Tool Pin Shape on Defect-Free FSP and Particles Distribution in SiC/Al6061 Composites49-62**

Mortza Ezzati, Parviz Asadi, Mostafa Akbari

 **DOR: 20.1001.1.2322388.2021.9.1.1.7**

Research Paper

Dissimilar DP780/DP980 Resistance Spot Welded joints: Microstructure, Mechanical Properties and Critical Diameter

Bahman Valizadeh, Mehdi Mansouri**Advanced Materials Research Center, Department of Materials Engineering, Najafabad Branch, Islamic Azad University, Najafabad, Iran*

ARTICLE INFO*Article history:*

Received 19 May 2020
Accepted 2 July 2020
Available online 3 January 2021

Keywords:

*Dissimilar Resistance Spot
Welding
DP780 Dual Phase steel
DP980 Dual Phase steel
critical weld nugget diameter
mechanical behavior*

ABSTRACT

In this research, microstructure and mechanical performance of dissimilar resistance spot welded DP780/DP980 dual-phase steels were studied utilizing optical microscope, microhardness, and tensile shear tests. Resistance spot welding (RSW) was performed in the current range of 7 to 12 kA, with 0.5 kA steps. At welding currents lower than 7 kA low amount of melting led to the very low strength of the joints due to small weld nugget diameter. The results showed that an increase in welding current from 7 kA up to 11 kA, result in an increase in weld nugget diameter. Further increase of welding current (higher than 11 kA), however decreased the weld nugget diameter due to severe melt expulsion. Microstructural studies showed that weld nugget was primarily comprised of martensite, and the heat-affected zone (HAZ) of both sides of the joint was comprised of three different microstructural zones; upper-critical HAZ (UCHAZ), inter-critical HAZ (ICHAZ), and sub-critical HAZ(SCHAZ). Microhardness test showed that at both sides, softening occurred at SCHAZ. The results of the tensile shear test showed that both peak load and fracture energy of the joints followed approximately the same trend as weld diameter with welding current. Two different fracture modes of interfacial failure (IF) and pullout failure (PF) were observed in the tensile-shear test. At welding currents lower than 10 kA, the failure occurred in IF mode, while at higher welding currents, PF was dominant. Weld nugget diameter at welding current of 10 kA; i.e., critical weld nugget diameter, was ~8.5 mm.

* Corresponding Author:

Email Address: MMansouri@pmt.iaun.ac.ir

1. Introduction

The resistance spot welding is one of the most important joining processes in sheet metal joining, particularly in the automotive industry, due to its high operation speed and suitability for automation. In the RSW process, heat is generated due to localized flow of electrical current through the parts being welded, according to Joule's law ($Q=RI^2t$, Where Q is generated heat, R is electrical resistance, and I and t are welding current and time, respectively). This heat causes to rise in the temperature at the interface of the workpieces that results in the melting of the workpieces and finally forming the weld nugget between the workpieces after solidification. It is worth noting that typically there are about 2000-5000 spot welds in a modern vehicle and the vehicle crashworthiness strongly depends on the mechanical performance of these spot welds [1]. On the other hand, weight reduction in the automotive industry, due to its role in the reduction of fuel consumption, has always been of great importance for manufacturers [1,2]. However, reduction of weight without safety considerations is not desirable, and then increase of the vehicle strength/weight ratio has attracted much attention of researchers and car manufacturers [3]. To increase the strength to weight ratio, utilization of low-density materials such as high strength aluminum alloys or using high strength alloy such as Advanced High Strength Steels (AHSS) for different parts of vehicles is very prevalent [4,5]. Among AHSSs, Dual Phase (DP) steels are one of the most utilized AHSSs in the automotive industry. DP steels, due to their special dual-phase microstructure (hard martensitic islands in a ductile ferrite matrix), exhibited both high strength and ductility. These steels that have almost similar physical properties are named by their ultimate tensile strength, e.g., DP780 has an ultimate tensile strength of ~780 MPa [6–8].

But it must be noted that the challenges of DP steel application in the automotive industry depend on their metallurgical interactions with other body parts in similar and dissimilar welding processes. Severe changes in hardness at weld zone and heat-affected zones [1,9] and higher susceptibility to shrinkage voids during solidification [3,10] are the most important challenges in similar and dissimilar welding of DP steels. Additionally, the complex microstructural changes occurring during welding of DP steels make it hard to determine failure mode and implement the standard to predict important quality control parameters such as critical welding diameter. Therefore, adjustment of RSW parameters in order to achieve desirable mechanical properties for spot welds has drawn the attention of many researchers [11]. Considering the substantial role of resistance spot welds in crashworthiness, studying the mechanical and microstructural properties of the spot welds in order to guarantee the occurrence of pullout failure during loading is crucial [2,12]. Therefore, in this research, the microstructural and mechanical properties of dissimilar DP780/DP980 resistance spot welds were investigated. Samples have been welded at different welding currents, then microstructural and mechanical investigations (in terms of peak load and fracture energy in tensile-shear test) have been carried out.

2. Experimental procedure

DP780 and DP980 steel sheets manufactured by inter-critical annealing process (heating the steel up to the two-phase ferrite+austenite region and then quenching of steel in order to promote the transformation of the formed austenite into martensite) were used as starting materials. The thickness of both DP780 and DP980 sheets was 2 mm. Table 1 shows the chemical composition of the DP780 and DP980 steel base metals.

Table.1 The chemical composition of started materials in present study (wt.%).

	%C	%Mn	%Si	%S	%P	%Ni	%Cr	%Fe
DP780	0.11	2.15	0.08	<0.01	<0.01	0.05	0.15	Bal.
DP980	0.14	2.45	0.05	<0.01	<0.01	0.04	0.25	Bal.

Welding specimens were cut to the size of 138 mm × 60 mm according to AWS D8.9 standard (Fig. 1). Oxides and contaminations on the faying surface of samples were removed, and then samples were set in joint lap configuration with an overlap of 45 mm. One spot weld was made at the center of the overlapped area for each joint. The welding process was carried out using a 120 kVA AC RSW machine (CU900, Novin Sazan co., Tehran, Iran) using a 45° truncated cone copper-chromium-zirconium

electrode (group A class II of RWMA classification) with 8 mm face diameter. The welding current was set from 7 to 12 kA with 0.5 kA steps. Other resistance welding parameters including pre-squeezing time (the period of applying a compressive force on the sheets before current passage in order to stabilize pressure and ensure good contact), electrode force (compressive force exerted on the sheets before, during, and after welding), welding time (current passage time) and

holding time (the period of maintaining compressive force after current passage to help better cooling and keeping the integrity of the joint) was set to 15 cycles, 4 kN, 30 cycles and 15 cycles, respectively (each cycle is ~0.02 s).

For each welding current, four samples were welded, three of which were used for tensile-shear test and one used for metallographical studies and microhardness examination. Metallographic samples were prepared using standard metallographic procedures, including grinding, polishing, and etching. Etching was done using 2% Nital solution for the general microstructure and Klemm's I etchant (50 ml water-saturated with $\text{Na}_2\text{S}_2\text{O}_3$ and 1 g $\text{K}_2\text{S}_2\text{O}_5$) to detect retained austenite. Then, the microstructure was examined utilizing the optical microscope (BX51, Olympus, Japan). The volume percentage of ferrite and martensite phases in the microstructure of the base materials was calculated

using ImageJ software. In order to investigate changes in the hardness profile of the welded samples, a microhardness test (Leco PIX2, Struers GMBH, Belgium) was carried out across two lines parallel to the weld interface in several points which were spaced 0.5 mm apart from each other on average. The indentation load and holding time were 100 g and 15 s, respectively. The tensile-shear test was conducted according to AWS D8.9 standard in order to determine the peak load (maximum force endured by the welded sample) and fracture energy (area under the force-displacement diagram up to peak load). The test was carried out by a tension-compression machine (E4486, Instron Inc., USA) with a tension rate of 10 mm/min. The failure mode of the samples after fracture in the tensile-shear test was determined by visual inspection as illustrated in AWS D8.9 standard. Fig. 1 shows the tensile-shear sample schematically.

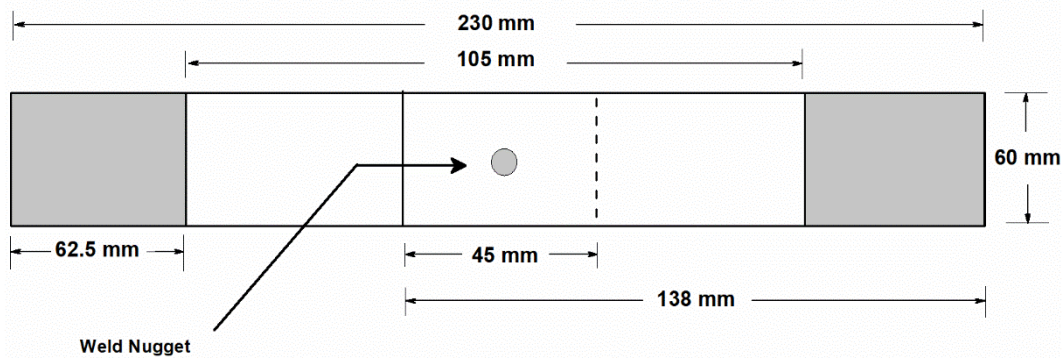


Fig.1. Schematics of a standard tensile-shear test sample.

Peak load is directly extracted from the force-displacement diagram, and fracture energy was calculated using numeral integration (Eq. 1), where F and X are force and displacement, respectively.

$$\text{Fracture energy} = \sum_{n=1}^{n=N} F(n)[X(n) - X(n-1)] \quad (1)$$

Failure modes of welded samples were determined by examining the fractured specimens after the tensile-shear test.

3. Results and discussion

3.1. Macro/microstructure of the weld joints

Fig.2 shows the macrostructure of DP780/DP980 RSW joint welded at 10 kA.

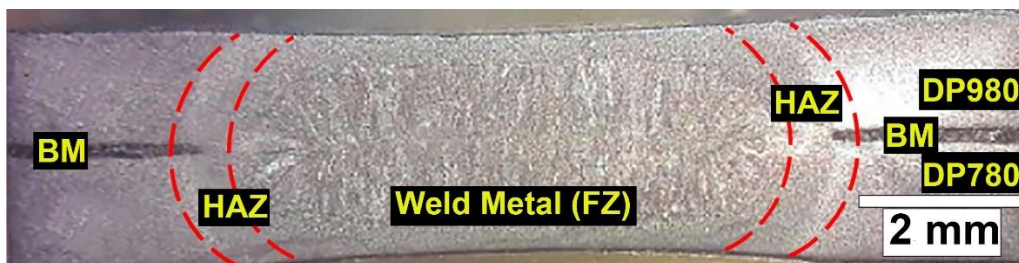


Fig. 2. Macrostructure of DP780/DP980 RSW joint welded at 10 kA.

As demonstrated by Fig. 2, RSW joints exhibit an inhomogeneous microstructure containing weld metal (Fusion Zone, FZ), HAZ (Heat Affected

Zone), and Base Metal (BM). FZ consists of columnar grains, which have grown from the fusion boundary toward the weld centerline and is a result

of the fusion and solidification process. Adjacent to FZ is the HAZ, where no fusion and solidification occur during welding, but as a result of high

temperature, microstructural changes widely occur [1, 10, 13]. Fig.3 shows the microstructure of different zone of the welded sample at 10 Ka.

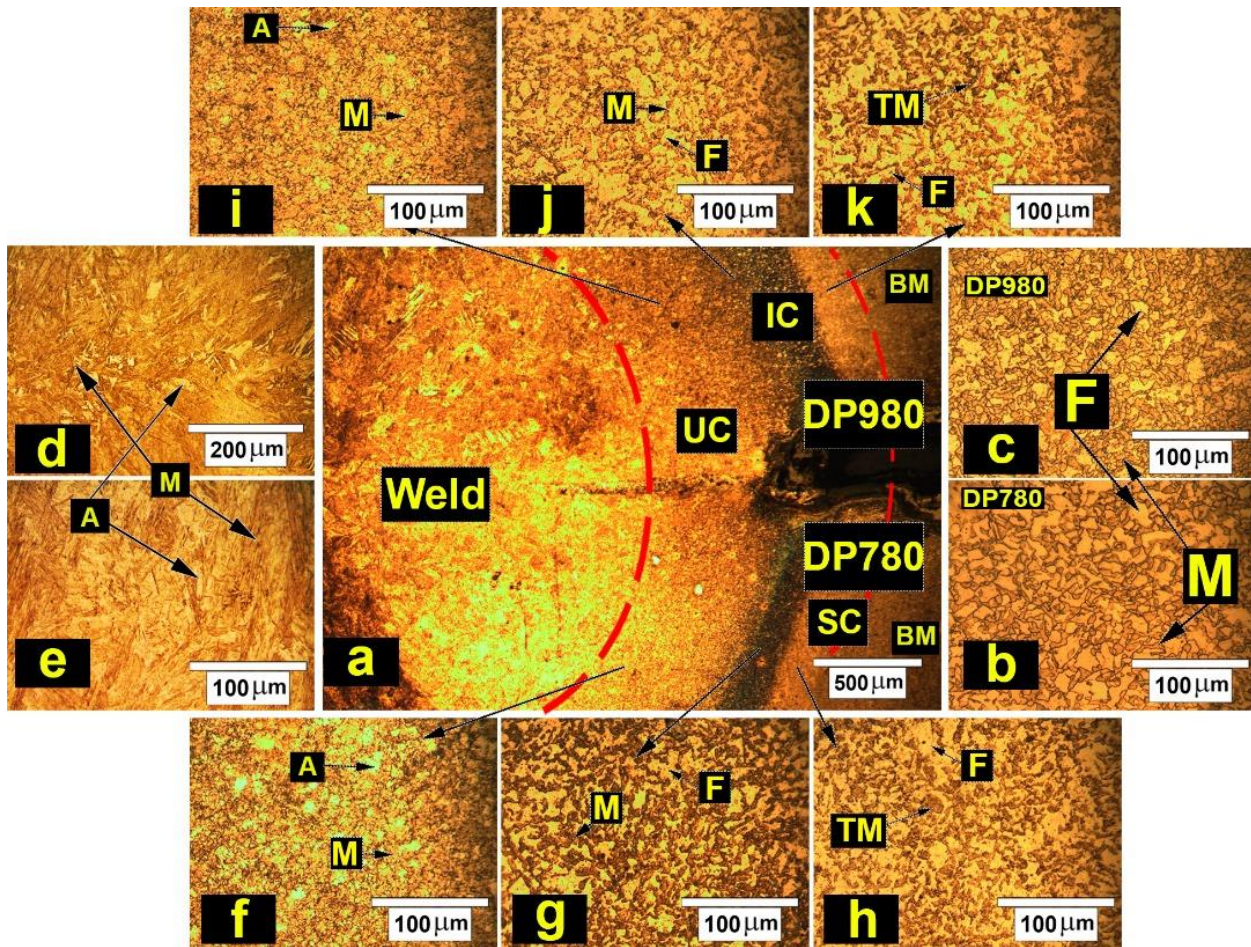


Fig. 3. Microstructure of a) DP780/DP980 resistance spot welded sample at 10 kA, b and c) base materials d and e) FZ, f, g and h) and i, j and k) different regions of HAZ (including upper critical (UC), inter critical (IC) and subcritical (SC)) in DP780 and DP980 sides respectively. A represents retained austenite, F represents ferrite, M represents martensite and TM represents tempered martensite.

Fig.3-b and c show the microstructure of DP780 and DP980 base metals, respectively. In both steels, the microstructure is comprised of martensitic islands in a ferrite matrix. The volume percent of the martensite phase was calculated to be 36% and 43% for DP780 and DP980, respectively.

The microstructure of FZ is presented in Fig.3-d and e. As shown, the FZ microstructure mainly consists of martensite as a result of a very high cooling rate in the RSW process, which is higher than the critical cooling rate for martensite formation. The critical cooling rate at which martensite forms in steels can be calculated from Eq. 2 [10]:

$$\text{Log}V = 7.42 - 3.13C - 0.71Mn - 0.37Ni - 0.34Cr - 0.45Mo \quad (\text{Eq. 2})$$

In this equation, V is the critical cooling rate (in K/h). Assuming that both base metals melt equally to form the weld nugget and using their chemical composition given in table 1, the critical cooling rate for the weld nugget would be ~ 52 °C/s. On the other hand, the analytical results have shown that the cooling rate of a 2 mm thick resistance spot-welded steel sheet is about 3000 °C/s [5]. Then it can be concluded that because of the higher cooling rate of the RSW process (3000 °C/s) that is significantly higher than the critical cooling rate for the weld nugget (~ 52 °C/s) formation of martensite in the FZ is very probable, as shown in Fig.3-d and e. The martensitic structure was also observed at similar and dissimilar joints RSWs of DP steels by other researchers [14–16].

Fig.3-f to fig.3-k show microstructure of different HAZ regions at both DP780 and DP980 sides. Considering microstructural changes, HAZ can be divided into three distinct regions, namely upper critical (UC), inter critical (IC), and subcritical (SC) HAZ [11, 17, 18]. At UCHAZ, the experienced peak temperature by this zone is above the A3 line. Thus the microstructure becomes fully austenitic, and as a result of high temperature near the fusion line, grain growth occurs severely in this region. Austenite grain growth leads to higher hardenability, and austenite transforms into martensite during the cooling cycle. At the ICHAZ region, the peak temperature is lower due to the higher distance from the fusion line, and temperature would not rise above A3 but remains between A3 and A1 (austenite+ferrite region). Therefore, the microstructure would consist of austenite and ferrite, that during cooling, austenite transforms into martensite [1, 18]. At the SCHAZ region, peak temperature would not get higher than the A1 line, so only the tempering of martensite in

the microstructure of the base metals (DP980 and DP780) occurred [19].

3.2. Mechanical properties

3.2.1. Microhardness profile

Fig. 4 shows changes in microhardness profile for the sample welded at 10 kA. As Fig. 4 shows, the average hardness value of FZ is ~410 HV. The high value of hardness at FZ is a result of martensite formation in this region [1, 18]. At the ICHAZ region, both martensite and ferrite are present in the microstructure (Fig.3), and the mean hardness value is lower than FZ (~350-300 HV), but still higher than both DP steel base materials (260 HV and 280 HV for DP780 and DP980 respectively). However, values of hardness at SCHAZ is lower than both base materials (~245 HV). This phenomenon is called HAZ softening and is resulted by tempering of the martensite [19, 20]. Moreover, the amount of softening at the DP980 side is slightly higher, which can be a result of higher martensite content in DP980 base metal.

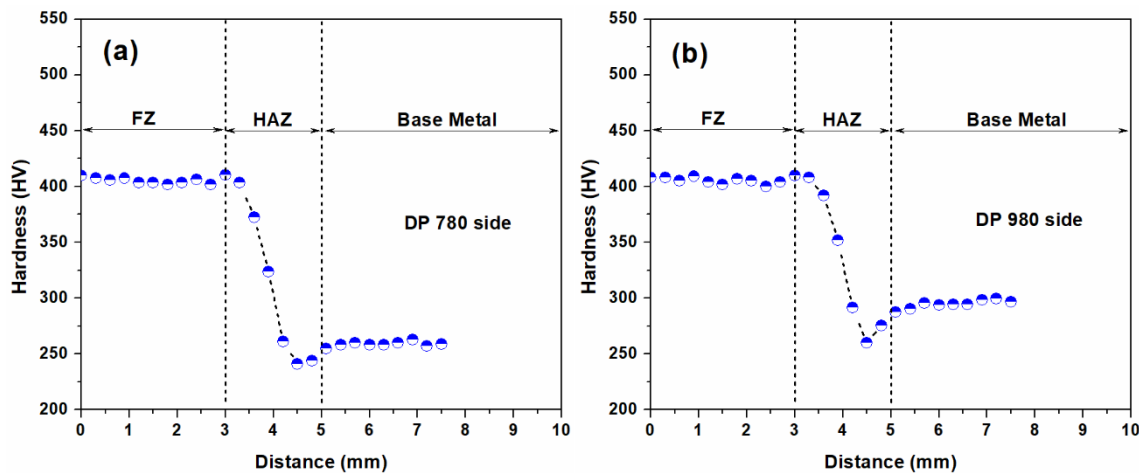


Fig.4. Microhardness profile of different regions of specimen welded at 10 kA, a) DP780 side and b) DP980 side.

3.2.2. Tensile properties and Failure mode

Fig. 5-a shows changes of weld nugget diameter with welding current. Up to 11 kA, weld nugget diameter increases with welding current. The main reason for

the increase is higher heat input and a higher amount of melting, which occurs at the weld interface. Nevertheless, at welding currents higher than 11 kA, the weld nugget diameter decreases as a result of expulsion.

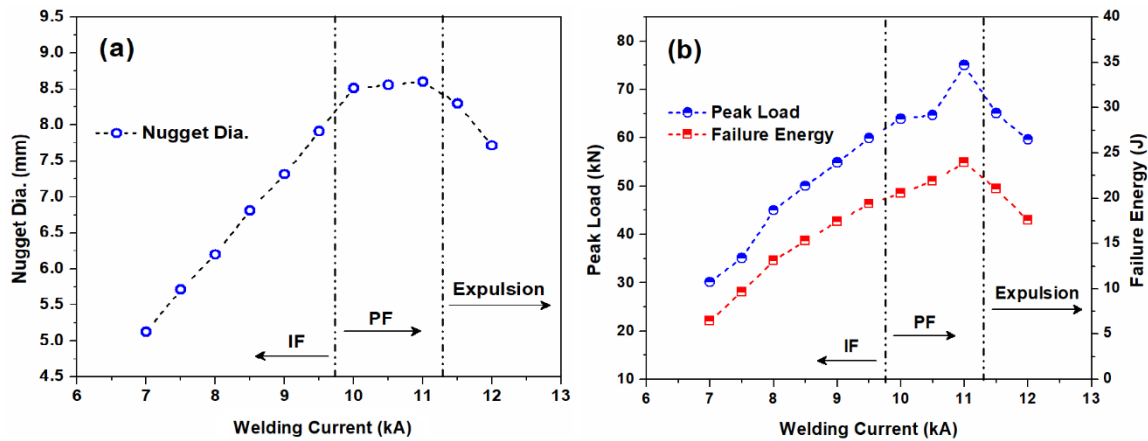


Fig.5. Effect of welding current on (a) Weld nugget diameter and (b) Peak load and failure energy of DP780/DP980 RSWs.

Failure mode was determined by examination of fractured tensile-shear test samples. In Interfacial Fracture (IF) failure mode, the crack propagates through the weld nugget because of the lower strength of weld metal, and the fracture occurs abruptly. On the other hand, at Pullout Fracture (PF) failure mode, failure occurs via withdrawal of the weld nugget from one sheet [1]. Results showed that up to 9.5 kA, the IF mode is the dominant failure mode. By increase in the welding current further than 9.5 kA the failure mode will change to PF mode. The changing of fracture mode is related to the weld nugget diameter. The weld nugget is the load-bearing part of the joint in the tensile-shear test, and the larger the weld nugget becomes, the higher would be the capacity of the joint to endure exerted loads. In weld nugget lower than the critical size, the load-bearing capacity of the weld nugget is lower than its surrounding (i.e., HAZ or BM) due to the small size of the weld nugget then the fracture propagates through the fusion zone (IF mode). By increase in the weld nugget due to an increase in welding current, the load-bearing capacity of the weld nugget increases and becomes more than the load-bearing capacity of the surrounding areas of the weld nuggets. Consequently, the failure occurs via withdrawal of the weld nugget from one sheet, and fracture mode changes from interfacial failure to pullout failure [1]. As shown elsewhere, PF fracture mode exhibits higher peak load and fracture energy than IF mode. Therefore, achieving PF fracture mode is a priority in most spot welding processes [10]. Fig. 5-b shows changes in peak load and fracture energy of the joints welded at different welding currents in the tensile-shear test. Both peak load and fracture energy increase with welding currents up to 11 kA and decrease afterward. The reason for the enhancement of tensile properties can be attributed to an increment of weld nugget diameter, which

increases load-bearing and energy absorption capacity of the joints before expulsion [21, 22].

PF fracture mode in the tensile-shear test usually begins with crack growth around the weld nugget. The difference of mechanical properties between weld nugget and surrounding regions is the main reason for changes in the crack growth path. In fact, the higher load-bearing capacity of the weld nugget leads to alteration of crack growth path from weld nugget (IF mode) to the HAZ (PF mode). Therefore, a critical weld nugget diameter (D_c) is defined as the diameter at which failure mode changes from IF to PF [10, 16].

Multiple theoretical equations have been developed in order to determine D_c [23–26]. For instance, according to the JIS Z3144 standard [25], the minimum weld nugget diameter in order to achieve PF mode can be calculated from Eq. 3.

$$D_c = 5\sqrt{t} \quad (3)$$

In which t is the thickness of base sheets. Utilizing eq.3, the critical nugget diameter calculated for the sheets used in this study becomes ~ 7.1 mm. The actual critical nugget diameter for failure mode transition in this research was ~ 8.5 mm, however, which is far larger than JIS Z3144 standards prediction and certifies that the standard equations cannot predict D_c for the DP780/DP980 RSW joints correctly. The main reason for this is the complexity of microstructure and mechanical properties of dissimilar joints made of DP steels. Thus, the equations which only use geometrical parameters to predict the critical FZ size could not correctly predict D_c for DP steels [23]. In order to address this issue, Pouranvari et al. [28] have developed a model which, in addition to plate thickness, takes into account the mechanical properties of the joints made of AHSS steels. In this model, D_c in the tensile-shear test is calculated using Eq. 4:

$$D_c = \frac{4t}{Pf} \cdot \frac{HPFL}{HFZ} \quad (4)$$

where t is the thickness of the base sheets, P is the porosity factor, f is the tensile strength/shear strength ratio, and $HPFL$, HFZ is the hardness of pullout failure location and FZ (in Vickers), respectively. As mentioned in section 3.2.1, the values of $HPFL$ and HFZ are 300 and 410 Vickers, respectively. Values of P and f are 1 and 0.5, respectively. Using this equation, D_c is calculated to be 8.8 mm, which is very similar to the experimental results achieved in this research.

4. Conclusion

In this research, the microstructural and mechanical properties of dissimilar DP780/DP980 resistance spot welds are investigated. The most remarkable achieved results are:

- 1) Microstructure of the weld nugget is mainly martensitic.
- 2) At both steels, the heat-affected zone is comprised of three distinct regions, namely upper critical, inter critical, and sub-critical heat affected zones. The difference in heat input and a peak temperature of these regions results in different microstructures, which contain martensite, martensite + ferrite, and tempered martensite + ferrite, for UCHAZ, ICHAZ, and SCHAZ, respectively.
- 3) Microhardness test results showed that the hardness of the fusion zone is ~410 HV. Additionally, softening was observed at the SCHAZ regions.
- 4) Changes in weld nugget diameter with welding current showed that nugget diameter first increases with welding currents up to 11 kA, and then decreases as a result of expulsion.
- 5) Values of peak load and fracture energy of the joints increase with welding currents up to 11 kA and then decrease. At 11 kA, the values of peak load and fracture energy are 80 kN and 30 J, respectively.
- 6) The results showed that changing from IF to PF mode occurred at welding currents of 10 kA. The critical weld nugget diameter was 8.5 mm.

References

- [1] Pouranvari M, Marashi SPH (2013) Critical review of automotive steels spot welding: process, structure and properties. *Sci Technol Weld Join* 18:361–403. <https://doi.org/10.1179/1362171813Y.0000000120>
- [2] Pouranvari M, Marashi SPH (2012) Weld nugget formation and mechanical properties of three-sheet resistance spot welded low carbon steel. *Can Metall Q* 51:105–109 <https://doi.org/10.1179/1879139511Y.0000000028>

- [3] Pouranvari M, Mousavizadeh SM, Marashi SPH, et al (2011) Influence of fusion zone size and failure mode on mechanical performance of dissimilar resistance spot welds of AISI 1008 low carbon steel and DP600 advanced high strength steel. *Mater Des* 32:1390–1398
- [4] Pouranvari M, Marashi SPH (2012) On failure mode of resistance spot welded DP980 advanced high strength steel. *Can Metall Q* 51:447–455. <https://doi.org/10.1179/1879139512Y.0000000034>
- [5] Gould JE, Khurana SP, Li T (2006) Predictions of microstructures when welding automotive advanced high-strength steels. *Weld J (Miami, Fla)* 85:
- [6] Hernandez BVH, Kuntz ML, Khan MI, Zhou Y (2008) Influence of microstructure and weld size on the mechanical behaviour of dissimilar AHSS resistance spot welds. *Sci Technol Weld Join* 13:769–776. <https://doi.org/10.1179/136217108X325470>
- [7] Ghaemifar S, Mirzadeh H (2017) Enhanced mechanical properties of dual-phase steel by repetitive intercritical annealing. *Can Metall Q* 56:459–463. <https://doi.org/10.1080/00084433.2017.1361223>
- [8] Shukla N, Roy H, Show BK (2016) Effect of prior austempering heat treatment on the microstructure, mechanical properties and high-stress abrasive wear behaviour of a 0.33% C dual-phase steel. *Can Metall Q* 55:13–22. <https://doi.org/10.1080/00084433.2015.1113671>
- [9] Zhang H, Qiu X, Bai Y, et al (2014) Resistance spot welding macro characteristics of the dissimilar thickness dual phase steels. *Mater Des* 63:151–158. <https://doi.org/10.1016/J.MATDES.2014.05.060>
- [10] Abadi MMH, Pouranvari M (2014) Failure-mode transition in resistance spot welded DP780 advanced high-strength steel: Effect of loading conditions. *Mater Tehnol* 48:67–71
- [11] Khan MI, Kuntz ML, Zhou Y (2008) Effects of weld microstructure on static and impact performance of resistance spot welded joints in advanced high strength steels. *Sci Technol Weld Join* 13:294–304. <https://doi.org/10.1179/174329308X271733>
- [12] Pouranvari M (2011) Influence of welding parameters on peak load and energy absorption of dissimilar resistance spot welds of DP600 and AISI 1008 steels. *Can Metall Q* 50:381–388. <https://doi.org/10.1179/1879139511Y.0000000008>
- [13] Zhang H, Wei A, Qiu X, Chen J (2014) Microstructure and mechanical properties of resistance spot welded dissimilar thickness DP780/DP600 dual-phase steel joints. *Mater Des* 54:443–449.

<https://doi.org/10.1016/J.MATDES.2013.08.027>

[14] Liang J, Zhang H, Qiu X, Shi Y (2015) Characteristics of the Resistance Spot Welding Joints in Dissimilar Thickness Dual-phase Steels. *ISIJ Int* 55:2002–2007.

<https://doi.org/10.2355/isijinternational.ISIJINT-2015-151>

[15] Di H, Sun Q, Wang X, et al (2017) Microstructure and properties in dissimilar/similar weld joints between DP780 and DP980 steels processed by fiber laser welding. *J Mater Sci Technol* 33:1561–1571.

<https://doi.org/10.1016/j.jmst.2017.09.001>

[16] Pouranvari M, Marashi SPH, Mousavizadeh SM (2010) Failure mode transition and mechanical properties of similar and dissimilar resistance spot welds of DP600 and low carbon steels. *Sci Technol Weld Join* 15:625–631.

<https://doi.org/10.1179/136217110X12813393169534>

[17] Gao S, Li Y, Yang L, Qiu W (2018) Microstructure and mechanical properties of laser-welded dissimilar DP780 and DP980 high-strength steel joints. *Mater Sci Eng A* 720:117–129. <https://doi.org/10.1016/J.MSEA.2018.02.057>

[18] Wei ST, Lv D, Liu RD, et al (2014) Similar and dissimilar resistance spot welding of advanced high strength steels: welding and heat treatment procedures, structure and mechanical properties. *Sci Technol Weld Join* 19:427–435.

<https://doi.org/10.1179/1362171814Y.0000000211>

[19] Pouranvari M, Marashi SPH (2010) Key factors influencing mechanical performance of dual phase steel resistance spot welds. *Sci Technol Weld Join* 15:149–155.

<https://doi.org/10.1179/136217109X12590746472535>

[20] Liu C, Zheng X, He H, et al (2016) Effect of

work hardening on mechanical behavior of resistance spot welding joint during tension shear test. *Mater Des* 100:188–197.

<https://doi.org/10.1016/J.MATDES.2016.03.120>

[21] Zhang H, Senkara J (2012) Resistance welding: fundamentals and applications. CRC Press, Boca Raton

[22] Wei ST, Liu RD, Lv D, et al (2016) Effect of joint configuration on resistance spot weldability of galvanised DP780 steel sheets. *Sci Technol Weld Join* 21:178–185.

<https://doi.org/10.1179/1362171815Y.0000000081>

[23] Pouranvari M, Marashi SPH (2011) Failure mode transition in AHSS resistance spot welds. Part I. Controlling factors. *Mater Sci Eng A* 528:8337–8343. <https://doi.org/10.1016/J.MSEA.2011.08.017>


[24] American Welding Society. Joint Committee on Automotive Welding., American Welding Society. Technical Activities Committee., American National Standards Institute. Test methods for evaluating the resistance spot welding behavior of automotive sheet steel materials

[25] (2017) JIS Z 3144: Routine test of resistance spot and projection welds, 13th ed. Japanese Standards Association (JSA)

[26] Y. J. Chao (2003) Failure mode of spot welds: interfacial versus pullout. *Sci Technol Weld Join* 8:133–137

[27] Sun X, Stephens E, Khaleel M (2006) Effects of Fusion Zone Size on Failure Modes and Performance of Advanced High Strength Steel Spot Welds. *SAE Trans.* 115:509–516

[28] Pouranvari M, Marashi SPH, Safanama DS (2011) Failure mode transition in AHSS resistance spot welds. Part II: Experimental investigation and model validation. *Mater Sci Eng A* 528:8344–8352. <https://doi.org/10.1016/J.MSEA.2011.08.016>

 **DOR: 20.1001.1.2322388.2021.9.1.2.8**

Research Paper

Preparation and Determination of the Characteristics of Hydrogel Membrane of Poly-Vinyl Alcohol, Starch and Chitosan

Shaghayegh Baghaie¹, Mohammad T. Khorasani^{2*}, Ali Zarrabi³, Jamal Moshtaghi⁴

1. Department of Biomedical Engineering, Science and Research Branch, Islamic Azad University, Tehran, Iran

2. Biomaterial Department of Iran Polymer and Petrochemical Institute, Tehran, Iran

3. Faculty of Advanced Sciences and Technologies, Department of Biotechnology, University of Isfahan, Iran

4. Department of Biology, University of Isfahan, Isfahan, Iran

ARTICLE INFO

Article history:

Received 25 June 2020

Accepted 15 August 2020

Available online 10 January 2021

Keywords:

Chitosan

Hydrogel

Polyvinyl Alcohol

Starch

ABSTRACT

In this study, a new kind of crosslinking film of polyvinyl alcohol, starch, and chitosan was obtained by alternating freeze-thaw cycles, and its various properties such as swelling rate, water vapor transmission rate, mechanical properties, and morphology were checked using electron microscopy. The results of this study showed that the hydrogel, made by providing a damp environment and the ability to pass water vapor in the range 720-1680 g/m², has acceptable mechanical properties so that the fracture stress in polyvinyl alcohol was equal to 0.642 kgf/ mm², which reached 0.372 kgf/ mm² with the introduction of starch and 0.2475 kgf/ mm² with the addition of chitosan. When we add starch and chitosan to polyvinyl alcohol at the same time, the fracture stress reaches 0.261 kgf/ mm². In the sample containing pure polyvinyl alcohol, the elastic strain is equal to 6.157 and with the addition of starch, this value reaches 4.625 and with the addition of chitosan, this value reaches 5.70. Adding starch and chitosan to polyvinyl alcohol increases the modulus and toughness and decreases the flexibility of the polyvinyl alcohol hydrogel membrane. Images of SEM from a cross-section of hydrogel membrane fracture show that hydrogel membranes containing polyvinyl alcohol are very smooth and monotonous; however, when starch and chitosan are added to polyvinyl alcohol, the porosity will increase.

* Corresponding Author:

E-mail Address: m.khorasani@ippi.ac.ir

1. Introduction

Hydrogels are three-dimensional solids similar to solids that are capable of absorbing large amounts of water while maintaining their dimensional stability [1]. The amount of water adsorbed in the hydrogels is related to the presence of specific groups such as COOH, OH, CONH₂, CONH and SO₃H, while their resistance to dissolution is due to crosslinks between the network chains [2]. Other factors such as capillary effect, pH, osmotic pressure, and temperature also affect the absorption of hydrogel water. The ability of hydrogels to absorb and release water reversibly and their ability to respond to specific environmental stimuli make hydrogels suitable for use in a variety of engineering fields. Hydrogels are classified into two groups based on the nature of the crosslinking: physical or chemical. Physically crosslinked polymers have transient and temporary bonds. In this method, networking begins with pH, temperature, and other physical stimuli. In physically crosslinked hydrogels, a covalent bond is not established between the chains but is networked by physical interactions such as ionic interactions, hydrogen bonds, or hydrophilic interactions [3]. Chemically crosslinked hydrogels have permanent connections. These types of hydrogels are prepared by forming a covalent bond between different polymer chains. Increasing attention to these types of hydrogels is due to their good mechanical strength.

Polyvinyl alcohol is a synthetic hydrophilic polymer that can be chemically crosslinked by electron beam, gamma, and glutaraldehyde, or physically crosslinked by the freeze-thaw process. When aqueous solutions of polyvinyl alcohol are kept at room temperature, the gel gradually forms with low mechanical strength. Aqueous solutions of polyvinyl alcohol form a strong and highly elastic gel when exposed to the freezing-thawing process. The properties of the resulting gel depend on the molecular weight of polyvinyl alcohol, its concentration in water, temperature, freezing time, and the number of freezing-thawing cycles. Polyvinyl alcohol, part of which is hydrolyzed, has a lower melting/degradation temperature. Excessive hydrolysis reduces solubility and increases viscosity with increasing molecular weight. Polyvinyl alcohol can be used to make films and coatings that have high tensile strength and flexibility and are resistant to the penetration of oxygen, carbon dioxide and other vapors. Specific applications of polyvinyl alcohol vary with the degree of hydrolysis and viscosity. If the degree of hydrolysis is higher, water resistance will be better. Moisture in polyvinyl alcohol acts as a softener and reduces tensile strength, increases elongation and tear threshold [4-6].

Starch is a plant polysaccharide of the homo polysaccharide type that is stored in the roots, buds and seeds of the plant. Among the types of polysaccharides, starch is of special importance due to its low price and abundance in nature. The starchy powder is odorless, tasteless, soft, and white. Starch grains contain long-chain glucose polymers that are insoluble in water. Starch is a dense sugar that consists of two main components. One of them dissolves in boiled water and makes up about 10 to 20% of the total starch, which is called amylose. The next part, which makes up about 80 to 90% of starch and dissolves in boiling water, is called amylopectin. These compounds are made up of glucose units. Amylose forms a colloidal precipitate in hot water, while amylopectin remains insoluble. In the hydrolysis process, long polysaccharide chains are broken down into smaller carbohydrate chains. The network structure of starch has good biodegradability, high mechanical properties, and chemical stability. Starch films have advantages such as low thickness, flexibility, and transparency, but also have disadvantages, such as poor mechanical properties and its permeability to water vapor. To improve the mechanical properties of starch films, we can mention the creation of cross-links and the combination of starch with other natural polymers. The combination of starch with biodegradable polymers such as polyvinyl alcohol improves its properties such as strength, high thermal stability and flexibility [7-10]. Chitosan has various properties, including non-toxicity, low cost, availability, antimicrobial activity [11], physiological neutrality, significant protein affinity, anticoagulant, anti-tumor [12] and so on. Chitosan is insoluble in aqueous solutions with a pH above 7 but dissolves in dilute acids with a pH below 6 such as glutamic acid, hydrochloric acid, acetic acid, formic acid, and butyric acid. The method of dissolution is that the amino groups of the polymer are protonated in acid and lead to the production of soluble polysaccharides. Solubility is also strongly affected by the addition of salt to the solution. The higher the ionic strength, the lower the solubility. Degradation of chitosan depends on factors such as the degree of deacetylation and the pH of the solution. Structures that are highly deacetylated (DD > 85%) have a relatively slow degradation rate, while structures with a lower degree of deacetylation degrade faster. Also, enzymatic hydrolysis is higher in acidic conditions [11]. Chitosan is a polysaccharide with varying amounts of free amine groups and can participate in reactions by forming hydrogen or ionic bonds. Molecular shape, hydrogen bonding, electrostatic repulsion between the chains adjacent to

chitosan cause the movement of this polyelectrolyte in dilute solutions [12,13].

The aim of this study was to obtain a suitable hydrogel membrane as a wound dressing. Considering that dressings must have the ability to absorb liquid, have good moisture permeability and at the same

time have acceptable mechanical properties, according to the said properties for the three cheap, available and biocompatible materials" polyvinyl alcohol, starch and chitosan "This study was put on the agenda for the first time.

Table 1: Types of hydrogel membranes made in this research

CS (dry weight of PVA/St)	Starch (g)	Starch (mol)	PVA (g)	PVA (mol)	Hydrogel membranes	Number
-----	----	-----	15	0.34	PVA	1
-----	2.5	0.015	15	0.34	PVA/St	2
7 %	----	-----	15	0.34	CS PVA/	3
7 %	2.5	0.015	15	0.34	CS PVA/ St/	4

2. Materials and methods

The raw materials used in this study were polyvinyl alcohol with a molecular weight of 72000 g/mol from the German company Merck, corn starch from the company Sigma Aldrich, chitosan with an average molecular weight of 1224,000 g, and 90 % degree of deacetylation from the company Sigma Aldrich and acetic acid Made by Merck Germany.

2.1. Preparation of polymer membranes

At this stage, polymer solutions with specific concentrations were prepared according to Table 1 and networked using successive freezing and thawing cycles. This method is based on phase separation and crystallite formation in polymer solutions. When a polymer solution is placed at a low temperature, the solvent (water in the case of aqueous solutions) freezes, and during this process, the polymers in the solution accumulate in small areas called "unfrozen liquid microphases." In this region, the local concentration of polymers increases, and this polymer arrangement remains unchanged during melting and the connection points form physical bonds and cause structural strength.

2.1.1. Preparation of polyvinyl alcohol hydrogel

15 g of polyvinyl alcohol (0.34 mol) was mixed in 50 ml of distilled water at 80 ° C and placed on a magnetic stirrer for 6 hours to obtain a uniform solution of polyvinyl alcohol.

2.1.2. Preparation of polyvinyl alcohol/starch hydrogel

15 g of polyvinyl alcohol (0.34 mol) was mixed in 50 ml of distilled water at 80 ° C and placed on a magnetic stirrer for 6 hours to obtain a uniform solution of polyvinyl alcohol. Then 2.5 g of starch (0.015 mol) was mixed in 50 ml of distilled water at

70 ° C and placed on a magnetic stirrer for 4 hours to obtain a uniform solution of starch. The polyvinyl alcohol and starch solutions were then mixed and placed on a magnetic stirrer for 3 h to obtain a uniform solution of polyvinyl alcohol/starch.

2.1.3. Preparation of polyvinyl alcohol/chitosan hydrogel

15 g of polyvinyl alcohol (0.34 mol) was mixed in 50 ml of distilled water at 80 ° C and placed on a magnetic stirrer for 6 hours to obtain a uniform solution of polyvinyl alcohol. Then 1 g of chitosan (7 % dry weight of polymer) was dissolved in 50 ml of 1 % acetic acid and then mixed with a solution of polyvinyl alcohol for 24 hours at room temperature using a magnetic stirrer.

2.1.4. Preparation of polyvinyl alcohol/starch/ chitosan hydrogel

First, 15 g of polyvinyl alcohol (0.34 mol) was mixed separately in 50 ml of distilled water at 80 ° C and placed on a magnetic stirrer for 6 hours to obtain uniform solutions of polyvinyl alcohol. Then 2.5 g of starch (0.015 mol) was mixed in 50 ml of distilled water at 70 ° C and placed on a magnetic stirrer for 4 hours to obtain a uniform solution of starch. The solutions were mixed and placed on a magnetic stirrer for 3 hours to obtain a uniform solution. 7 % dry weight of polymer (polyvinyl alcohol and starch) chitosan was dissolved in 100 ml of acetic acid 1% and then the three solutions obtained (polyvinyl alcohol, starch, and chitosan) were dissolved for 24 hours. They were mixed at room temperature using a magnetic stirrer.

2.1.5. Preparation of hydrogel cross-linked membranes

The resulting hydrogels were poured into Petri dishes made of polystyrene and the bubbles inside

the hydrogel were removed using nitrogen gas. Consecutive freeze-thaw cycles were used to crosslink the resulting solution. In this way, first, the obtained hydrogel was frozen at $-20\text{ }^{\circ}\text{C}$ for 18 hours and then melted at $25\text{ }^{\circ}\text{C}$ for 6 hours. This operation was repeated 3 times. To remove unreacted material,

the crosslinked hydrogel was immersed in distilled water for 3 h and changed once every hour. The resulting hydrogel was dried in an incubator at $48\text{ }^{\circ}\text{C}$ for 48 h to a relative humidity of 53%. To maintain the obtained moisture, it was kept in a closed container at $4\text{ }^{\circ}\text{C}$ (Fig. 1) [14-17].

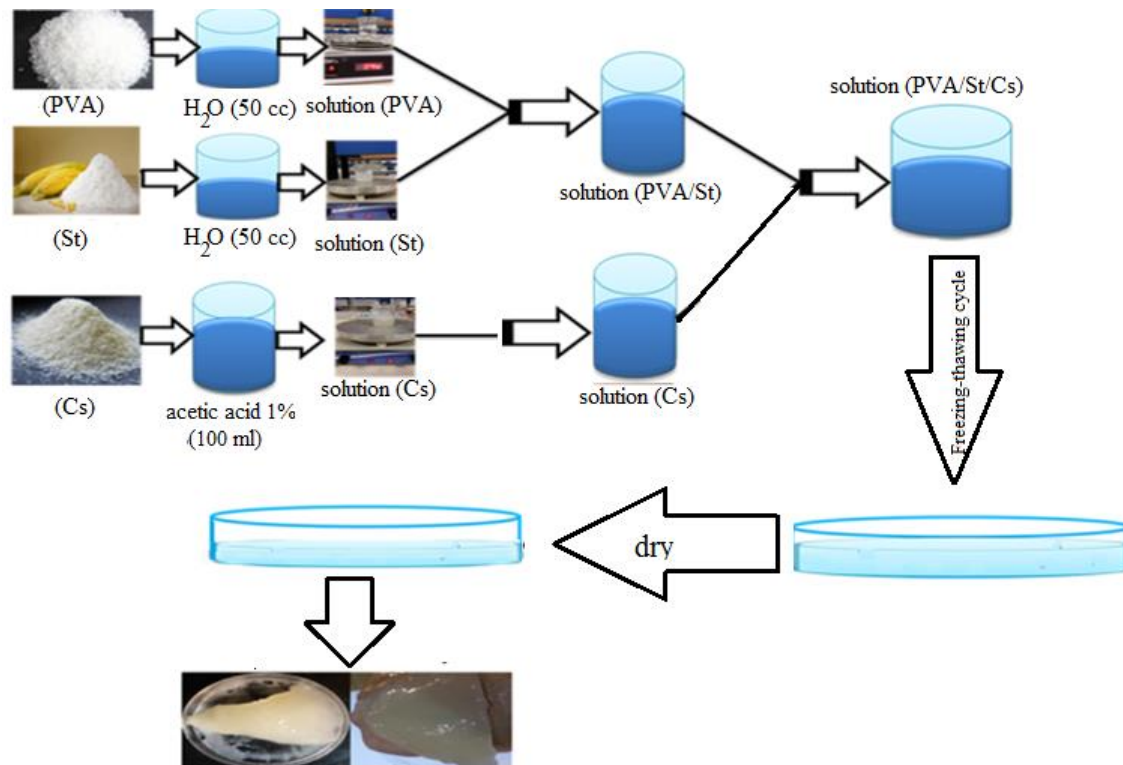


Fig.1. Hydrogel membrane containing PVA/St/CS

3. Investigating the properties of hydrogels

3.1. Equilibrium swelling ratio (ESR)

Samples of hydrogels ($2\text{ cm} \times 2\text{ cm}$ and 2 mm thick) were prepared. The samples were then dried at $60\text{ }^{\circ}\text{C}$ for 12 hours and their weight was measured using a digital scale. The phosphate buffer solution (PBS) was then placed in a laboratory at $37\text{ }^{\circ}\text{C}$ for 24 hours and its weight was measured every hour by removing the hydrogel and drying its surface and returning it to the container. The experiment was performed three times for each sample and the results were reported as average. The following formula was used to calculate the amount of hydrogel swelling [18].

$$\text{ESR} = \frac{W_w - W_d}{W_d} \quad (1)$$

The weight of the hydrogel is in the swollen state (W_w) and the initial weight of the hydrogel is dry (W_d).

3.2. Water Vapor Transmission Rate (WVTR)

Moisture permeability of a hydrogel membrane is possible by measuring the degree of water vapor

transfer using materials and using the ASTM standard. The standard for this test is the JIS1099A method. A round sample of hydrogel was placed on the nose of a 7 cm diameter cup containing 50 g of CaCl_2 so that no water vapor could pass through the edges. Teflon tapes were used for this purpose. Both were then placed in an incubator at 90% relative humidity at $40\text{ }^{\circ}\text{C}$. Water vapor transmission rate (WVTR) is calculated as follows [19].

$$\text{WVTR} \left(\text{g} / \text{m}^2 / \text{day} \right) = \frac{(W_2 - W_1)}{S} \times 24 \quad (2)$$

W_1 and W_2 the total weights of the cup in the first and second hours and 'S' is the surface area of the sample.

3.3. Mechanical test

Tensile strength and elongation of the specimens were determined using a model tensile tester (Instron 4464, UK). After freezing-thawing cycles, the hydrogel membranes were cut in a dumbbell-like

manner (6 cm long, 2 cm wide at both ends, and 1 cm wide at the center) and both ends of the sample were fixed with a special clamp. Samples were measured at a speed of 20 mm/min using a cell load of 0.5 N at room temperature to measure tensile strength, elongation, and maximum stress until failure of the samples. After the experiment, the stress-strain diagram was received from the device. The thickness of the sample was measured before the experiment. This test was performed 3 times for each sample and the result was reported as average [19].

3.4. Scanning electron microscope test (SEM)

In a Scanning Electron Microscopy (SEM) (Model VEGAX MU), a relatively high-energy electron beam travels over the sample surface. To perform this experiment, the prepared samples were first placed in liquid nitrogen to be completely frozen. They were then broken up with liquid pliers into the liquid nitrogen to completely preserve their cross-sectional morphology. After preparing the samples, their surface was covered with a thin sheet of gold. In this case, the samples are ready to be viewed with an electron microscope.

4. Results and discussion

In this section, first physical properties such as hydrogel swelling rate, water vapor permeability, and mechanical properties such as tensile strength, yield stress, fracture stress, toughness, and Young's modulus were studied, and then the morphology of hydrogel membrane fracture surfaces was investigated.

4.1. Hydrogel swelling rate

The swelling behavior of the hydrogel depends on the nature of the polymer network such as the presence of hydrophilic groups, crosslinking density, and the elasticity of the polymer network, pH, and

temperature of the swelling environment. Thus, any variation in the structure of the hydrogel network directly affects the swelling behavior. In this study, changes in the swelling capacity of hydrogel membranes over time were investigated. Fig. 2 shows the equilibrium swelling capacity of PVA/CS, PVA/St, and PVA/St/CS hydrogel membranes as a function of time. The increase in the swelling ratio of hydrophilic membranes containing starch and chitosan is due to the hydrophilic nature of the hydroxyl (OH) groups of starch and chitosan molecules in the gel networks. Because the presence of chitosan reduces the density of the polymer network and increases the porosity of the structure, it is obvious that it has higher water absorption than the hydrogel membrane containing starch. Higher bonding within hydrogel membranes limits the infiltration of water for swelling. The porous hydrogel network increases the water holding capacity and this helps to improve the swelling feature of the plates. Figure 3 also shows the equilibrium swelling capacity of PVA/St, PVA/CS, and PVA/St/CS hydrogel membranes at pH of 1.2 and 7.4 in different percentages of polyvinyl alcohol. It is observed that all hydrogel membranes have higher water absorption in an acidic environment than an alkaline environment, which is due to the presence of amine groups. The chitosan amine group contains protons in an acidic environment, resulting in electrostatic repulsion and the separation of hydrogen bonds between the polymer and the release of macromolecular chains, which ultimately leads to an increase in the swelling ratio. In a neutral or alkaline environment, chitosan amino groups become proton-free and electrostatic repulsion is reduced, leading to reduced swelling properties. Changing the pH of the environment causes the volume of holes in the polymer to fluctuate, which affects the swelling behavior of the hydrogel.

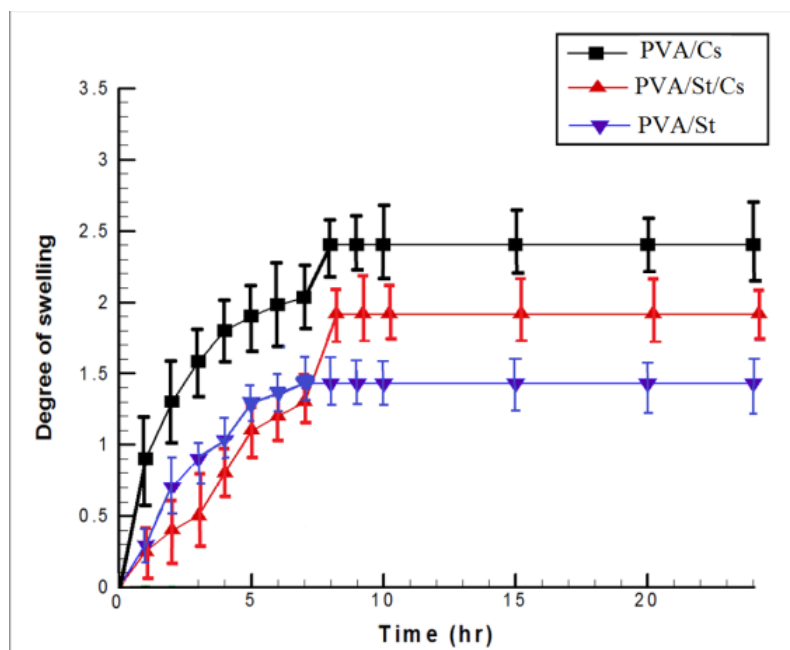


Fig. 2. Equilibrium swelling capacity of PVA/St, PVA/CS, and PVA/St/CS hydrogel membranes in PBS

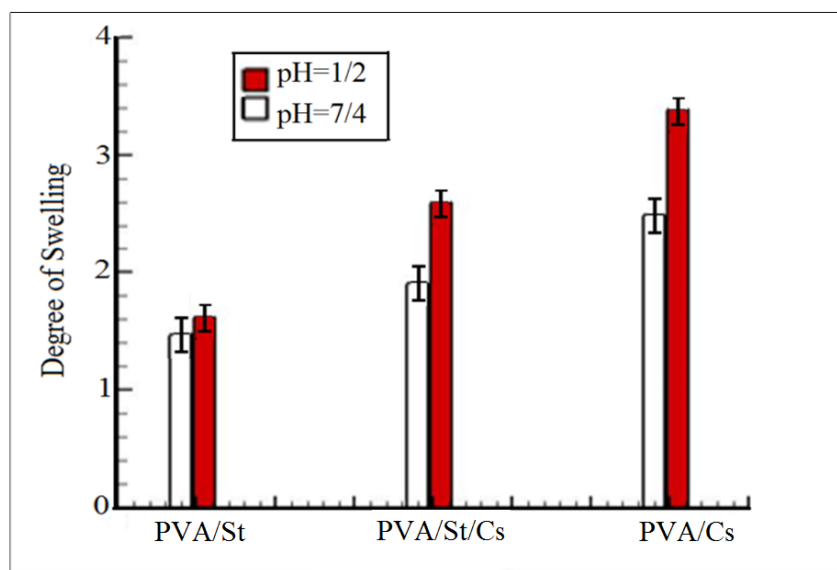


Fig. 3. Equilibrium swelling capacity of PVA/St, PVA/CS, and PVA/St/CS hydrogel membranes at pH = 2.1 and pH = 4.7 in PBS

4.2. Water Vapor Transmission Rate (WVTR)

Figure 4 shows the rate of passage of water vapor on different hydrogel membranes. It is observed that the hydrogel membrane, which contains only polyvinyl alcohol, has the lowest water vapor permeability. Polyvinyl alcohol hydrogel membranes allow less water vapor to pass through due to the greater crosslinking. Higher bonding within the hydrogel

membranes restricts the passage of water vapor. It is observed that the presence of starch increases the passage of water vapor. Starch has poor mechanical properties and high permeability to water vapor, and the use of starch alone to produce a hydrogel membrane limits its application. To improve the mechanical properties of starch films and at the same time increase their resistance to water vapor passage, crosslinking and starch composition with other polymers such as polyvinyl alcohol can be used. By

crosslinking the polyvinyl alcohol/starch hydrogel membrane, we see an increase in equilibrium swelling and water vapor permeability in polyvinyl alcohol. Polyvinyl alcohol/starch mixtures have hydrophilic surfaces that tend to get wet in aqueous media, and the hydrophilic nature of polyvinyl alcohol increases the compatibility with starch and prepares it for preparation as a polymer mixture. As can be seen in Figure 4, by adding chitosan to polyvinyl alcohol, the rate of water vapor passage in the hydrogel membrane reaches its highest level among the other membranes examined. This is due to the hydrophilic nature of the hydroxyl (OH) groups of chitosan molecules in hydrogel networks.

The presence of chitosan reduces the degree of crystallinity of polyvinyl alcohol. Chitosan reduces crosslinks within the polyvinyl alcohol network and creates a porous hydrogel network that has the highest water holding capacity and the highest water vapor transmission capability. This effect can be attributed to the reduction of polymer substrate cohesion in the presence of chitosan. The simultaneous presence of starch and chitosan in the hydrogel membrane fills the voids inside the gel network and increases the density of the network; therefore, the transfer of water vapor to the polyvinyl alcohol/chitosan hydrogel membrane is slightly reduced.

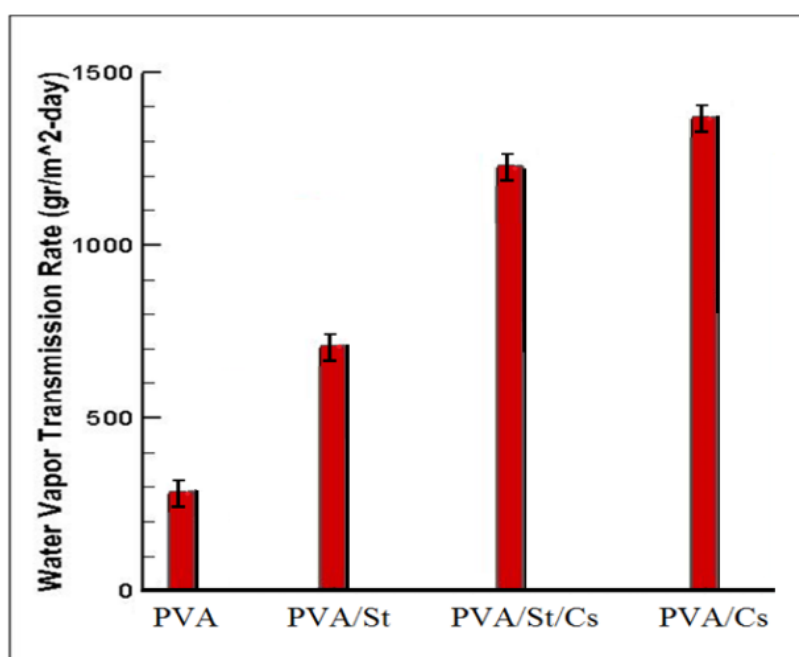


Fig. 4: Water vapor transmission rate on different hydrogel membranes

4.3. Mechanical test

The interaction between different components plays an important role in the properties of hydrogel membranes, especially mechanical properties. There are different interactions between different amounts of polyvinyl alcohol, starch, and chitosan. As a result, different amplitudes of hydrogen bonding occur in the hydrogel membranes, leading to different mechanical behavior in the samples. In this study, polyvinyl alcohol, polyvinyl alcohol/starch, polyvinyl alcohol/chitosan, and polyvinyl alcohol/starch/chitosan hydrogel membranes were synthesized and tested for mechanical properties. The stress-strain diagrams of the polyvinyl alcohol, polyvinyl alcohol/chitosan, polyvinyl alcohol/starch, and polyvinyl alcohol/starch/chitosan hydrogel

membranes are shown in Figure 5. According to the diagrams and Table 2, the fracture stress in polyvinyl alcohol was equal to 0.642 kgf/mm², which reached 0.372 kgf/mm² with the introduction of starch and 0.2475 kgf/mm² with the addition of chitosan. The polyvinyl alcohol hydrogel membrane has the maximum fracture strength among other hydrogel membranes due to the presence of more cross-links. Adding chitosan and starch to polyvinyl alcohol reduces the maximum force required for failure and the specimens change less length before failure. According to Table 2, when we add starch and chitosan to polyvinyl alcohol at the same time, the fracture stress reaches 0.261 kgf/mm². Starch has poor mechanical properties. To increase the strength and flexibility of starch, cross-linking and combining starch with polyvinyl alcohol can be used. The

presence of chitosan also reduces the degree of crystallinity of polyvinyl alcohol. According to Table 2, in the sample containing pure polyvinyl alcohol, the elastic strain is equal to 6.157 and with the addition of starch, this value reaches 4.625 and with the addition of chitosan, this value reaches 5.70. It can also be concluded that due to the stress applied to the polyvinyl alcohol/starch hydrogel membranes, the starch granules disappear as single structures and form a discontinuous membrane such as after swelling and gelatinization. The effect of high pressure on starch granules leads to limited swelling and begins to degrade, leading to failure at less stress and less change in length. Toughness is the amount of energy needed to reach the breaking point. In designing an ideal specimen, we often sacrifice the strength of the material to some extent to increase its toughness. The material is more elastic strain and toughness can be more before the break, pulled high. Adding starch and chitosan to polyvinyl alcohol increases the modulus and toughness and decreases the flexibility of the polyvinyl alcohol hydrogel membrane. Intermolecular interaction between starch, chitosan and polyvinyl alcohol polymers leads to a decrease in the density of crosslinking in polyvinyl alcohol.

Numerous synthetic and natural polymeric materials have been developed to treat burn wounds as antibacterial agents. However, due to poor mechanical

properties as well as low water absorption rate, their application is limited. The interaction between different components plays an important role in the properties of hydrogel membranes, especially mechanical properties. There are different interactions between different amounts of polyvinyl alcohol, starch and chitosan. As a result, different hydrogen bond domains are formed in the hydrogel membranes, leading to different mechanical behavior in the samples. Therefore, a completely homogeneous mixture must be prepared. The polyvinyl alcohol hydrogel membrane has the maximum force required for failure among other hydrogel membranes due to the presence of more crosslinks. Also, the largest change in length to the breaking point is related to polyvinyl alcohol, and by adding chitosan and starch to polyvinyl alcohol, the maximum force required for failure is reduced and the samples change less length before failure. Chitosan creates a porous hydrogel network by reducing the cross-links within the polyvinyl alcohol network, thus reducing the force required for failure and breaking the sample with less change in length. Due to its high tensile strength and flexibility, polyvinyl alcohol hydrogel membranes can be used to make wound dressings. However, adding starch and chitosan increases the density of the polyvinyl alcohol crystal lattice and reduces flexibility by reducing intermolecular distances.

Table 2. Mechanical properties of various types of hydrogel membranes made in this research

Young module kgf/mm ²	Toughness kgf/mm ²	Fracture stress kgf/mm ²	Yield stress kgf/mm ²	Elastic strain	Hydrogel membranes	No.
0.6056 ± 0.10	1.965 ± 0.18	0.642 ± 0.11	0.075 ± 0.16	6.157 ± 0.12	PVA	1
0.7025 ± 0.12	0.879 ± 0.12	0.372 ± 0.05	0.027 ± 0.02	4.625 ± 0.08	PVA/St	2
0.7909 ± 0.11	1.353 ± 0.21	0.475 ± 0.08	0.05 ± 0.01	5.70 ± 0.10	CS PVA/	3
0.7932 ± 0.09	2.168 ± 0.32	0.61 ± 0.12	0.05 ± 0.01	6.17 ± 0.07	CS PVA/ St/	4

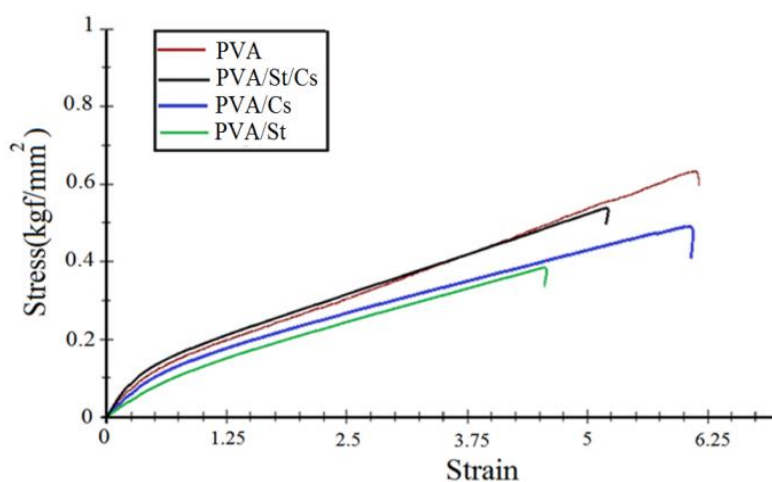


Fig. 5. Stress-strain diagram of PVA, PVA/CS, PVA/St, PVA/St/CS hydrogel membranes

4.4. Electron microscope images

SEM imaging is a promising method for studying the topography of samples that provides important information about the shape and size of the synthesized particles. SEM micrographs taken from the fracture cross-sections of the specimens are shown in Fig. 6. As can be seen, the cross-sectional area of the hydrogel membranes containing polyvinyl alcohol is very smooth and lacks the smallest cavities, and is quite uniform due to the presence of more cross-links. As can be seen, when starch and chitosan are added to the polyvinyl alcohol hydrogel membrane, the number of pores increases, which is consistent with the results of water absorption and water vapor permeability. The

larger the pores, the more hydrogel membranes can hold water and allow more water vapor to pass through. Adding starch and chitosan to polyvinyl alcohol reduces the degree of crystallinity and crosslinking within the polyvinyl alcohol network, resulting in a porous hydrogel network. In addition, the increase in porosity along with the decrease in the atomic distance leads to a decrease in the membrane's ability to stretch and an increase in length to failure. Since hydrogel membranes are synthesized with regular and alternating freeze-thaw cycles based on the presence of polyvinyl alcohol, it is observed that the presence of chitosan and starch in the membrane interferes with the physical bonds of polyvinyl alcohol and as a result, porosity is increased and we no longer see a smooth surface.

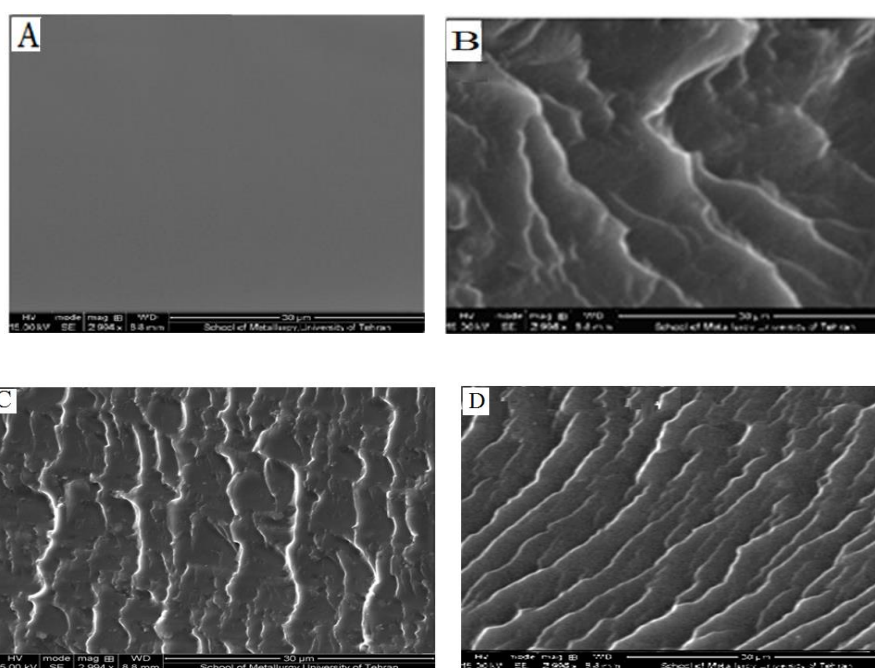


Fig. 6. The cross-sectional SEM image of A) PVA, B) PVA/St, C) PVA/CS, D) PVA/St/CS

5. Conclusion


Polyvinyl alcohol, polyvinyl alcohol/starch, polyvinyl alcohol/chitosan, and polyvinyl alcohol/starch/chitosan membranes were synthesized. The equilibrium swelling capacity of hydrogel membranes was investigated and it was found that all hydrogel membranes have higher water absorption in an acidic environment than alkaline environments due to the presence of amine groups. Also, due to the different amplitudes of hydrogen bonding between different components of hydrogel membranes, we see different mechanical behavior in the samples. The polyvinyl alcohol hydrogel membrane has the maximum fracture strength among other hydrogel membranes due to the presence of more cross-links. Adding chitosan and starch to polyvinyl alcohol reduces the maximum force required for failure and

the specimens change less length before failure. Chitosan creates a porous hydrogel network by reducing cross-links within the polyvinyl alcohol network, thus reducing the force required for failure and breaking the sample with less change in length. Adding starch and chitosan to polyvinyl alcohol increases the modulus and toughness and decreases the flexibility of the polyvinyl alcohol hydrogel membrane. Intermolecular interaction between starch, chitosan, and polyvinyl alcohol polymers leads to a decrease in the density of cross-links in polyvinyl alcohol. In the water vapor transmission rate, it was found that hydrogel membranes containing polyvinyl alcohol allow less water vapor to pass due to the presence of more crosslinks. Also, the presence of chitosan and starch increases the passage of water vapor in the range (720-1680 g/m²). Electron

microscope images were taken from the cross-sectional area of the hydrogel membrane for topographic study and it was observed that the hydrogel membranes containing polyvinyl alcohol were very smooth, without the smallest cavities, and perfectly uniform. When starch and chitosan were added to the polyvinyl alcohol hydrogel membrane, the number of pores is increased and the porosity is increased. As a result, the 3D network density is reduced.

References

- [1] Y. Xiong, X. Zhang, X. Ma, W. Wang, F. Yan, X. Zhao, X. Chu, W. Xu and Ch. Sun, "A review of the properties and applications of bioadhesive hydrogels", *Polymer Chemistry*, Issue 26, 2021, pp. 3721-3739.
- [2] I. A. Khalil, B. Saleh, D. M. Ibrahim, C. Jumelle,^f A. Yung, R. Dana and N. Annabi, "Ciprofloxacin-loaded bioadhesive hydrogels for ocular applications", *Biomater. Sci.*, 2020, 8, 5196-5209.
- [3] M.F. Akhtar, M. Hanif, N.M. Ranjha, "Methods of Synthesis of Hydrogels: A Review", *Saudi Pharm. J.*, Vol. 24, 2016, pp.554-559.
- [4] R. R-Rodríguez, H. E-Andrews, C. V-Martínez and Z. Y. G-Carvajal "Composite hydrogels based on gelatin, chitosan and polyvinyl alcohol to biomedical applications: a review", *International Journal of Polymeric Materials and Polymeric Biomaterials* Volume 69, 2020 - Issue 1
- [5] B. E. Karaogul, E. Altuntas, T. Salan and M. H. Alma "The Effects of Novel Additives Used in PVA/Starch Biohybrid Films", Submitted: July 2nd 2018 Reviewed: September 28th 2018 Published: December 19th 2018 DOI: 10.5772/intechopen.81727.
- [6] A. Jayakumar¹, H. K V¹, S. T S¹, M. Joseph¹, Sh. Mathew¹, P. G², I. C Nair³, R. E K⁴" Starch-PVA composite films with zinc-oxide nanoparticles and phytochemicals as intelligent pH sensing wraps for food packaging application". *Int J Biol Macromol.* 2019 Sep 1;136:395-403. doi: 10.1016/j.ijbiomac.2019.06.018. Epub 2019 Jun 4.
- [7] Y. Fan, F. Picchioni, "Modification of starch: A review on the application of "green" solvents and controlled functionalization", *Carbohydrate Polymers* Volume 241, 1 August 2020, 116350.
- [8] K. Bashir and M. Aggarwal, Physicochemical, structural and functional properties of native and irradiated starch: a review, *J Food Sci Technol.* 2019 Feb; 56(2): 513–523. Published online 2019 Jan 1. doi: 10.1007/s13197-018-3530-2. PMID: PMC6400748
- [9] Z.H. Xiong, P. Fei, "Physical and chemical modification of starches: A review", Vol. 13, 57(12), 2017, pp.2691-2705.
- [10] U. Shah, A. Gani, B. Ahmad Ashwar, A. Shah, M. Ahmad, A. Gani, A. Idrees, F.A. Wani Masoodi, "A review of the recent advances in starch as active and nanocomposite packaging film", Vol. 1, 2015, pp.1115640-1115649.
- [11] Ch. Sh.Karua, A.Sahoo, "Synthesis and characterization of starch/chitosan composites", *Materials Today*, Volume 33, Part 8, 2020, Pages 5179-5183
- [12] Gh.Sargazi, D.Afzali, A.Mostafavi, A.Shadman, B.Rezaee, P.Zarrintaj, M.Saeb, S.Ramakrishna, M.Mozafari, Chitosan/polyvinyl alcohol nanofibrous membranes: towards green super-adsorbents for toxic gases, *Materials Science*, Volume 5, Issue 4, April 2019, e01527.
- [13] H M Manal, Different fabrication methods of tissue engineering, *An International Journal of Medicine*, Volume 111, Issue suppl_1, December 2018, hcy200.224.
- [14] J. D. Carrera, D. A. V. Narváez, M. Leon, J. F. Alvarez, "Effect of Starch Oxidation Degree on the Properties of Hydrogels from Dialdehyde Starch and Polyvinyl Alcohol", *Journal A Bimonthly Peer-Review Journal* (ISSN: 2415-6698).
- [15] N. Mallick, D. Pal, and A. B. Soni, "Cornstarch/polyvinyl alcohol bio-composite film for food packaging application", *AIP Conference Proceedings* 2201, 020005 (2019); <https://doi.org/10.1063/1.5141429>.
- [16] Y. Ying, Y. Wu, J. Huang, Preparation and characterization of chitosan/poly(vinyl alcohol)/graphene oxide films and studies on their antibiofilm formation activity. *J Biomed Mater Res A.* 2020 Oct;108(10):2015-2022. doi: 10.1002/jbm.a.36961. Epub 2020 May 4.
- [17] I. P. Merlusca, D. S. Matiut, G. Lisa, M. Sillion, L. Gradinaru, S. Oprea & I. M. Popa, "Preparation and characterization of chitosan-poly(vinyl alcohol)-neomycin sulfate films", *Polymer Bulletin* vol. 75, pages3971–3986 (2018).
- [18] Gh.D.Afzali, A.Mostafavi, A.Shadman, B. Rezaee, P.Zarrintaj, M.Saeb, S.Ramakrishna M.Mozafari "Chitosan/polyvinyl alcohol nanofibrous membranes: towards green super-adsorbents for toxic gases", Volume 5, Issue 4, April 2019, e01527.
- [19] S. Nikzad, B. Hashemi, Z.M. Hassan, H. Mozdarani, "The cell survival of F10B16 melanoma and 4T1 breast adenocarcinoma irradiated to gamma radiation using the MTT assay based on two different calculation methods", *Journal of Biomedical Physics & Engineering*, Vol. 3(2), 2013, pp.29-36.

 DOR: 20.1001.1.2322388.2021.9.1.3.9

Research Paper

Fabricating the Tribological Properties and Investigating of Ni₃Al-MoS₂ Composite Coating

Mahdi Mirzaaghaei^{1*}, Mohammad-Hossein Enayati², Mahdi Ahmadi³*1. Student, Department of Materials Engineering, Naghshe Jahan University, Isfahan, Iran**2. Department of Materials Engineering, Isfahan University of Technology, Isfahan, 84154, Iran**3. Department of Materials Engineering, Naghshe Jahan University, Isfahan, 77142, Iran*

ARTICLE INFO

Article history:

Received 25 April 2020

Accepted 30 July 2020

Available online 1 January 2021

*Keywords:**Ni₃Al**MoS₂**magnetron sputtering**wear*

ABSTRACT

Self-lubricant coatings are among the newly improved type of coatings to reduce the coefficient of friction and protect the substrate in various conditions. Magnetron sputtering is the best technology to fabricate coatings with good morphology. In this paper, the tribological properties of magnetron sputtered Ni₃Al-MoS₂ coating on 4340 steel are reported. For this purpose, five tablets of Ni₃Al-30 wt.% MoS₂ were prepared as the target material and were placed in a copper holder. At last, we have sputtered from the target using the best sputtering condition to get a good morphology and microstructure of the coating. The morphology and microstructure of the coatings were characterized by X-ray diffraction (XRD) and scanning electron microscopy (SEM). The tribological properties of Ni₃Al-MoS₂ coating were investigated using a ball-on-disc tribometer at atmospheric conditions at room temperature. SEM was used to examine the morphology of the wear track after the ball-on-disc test. The Ni₃Al-MoS₂ composite coating showed lower frictions coefficient and higher wear resistance because of the hard Ni₃Al matrix and soft MoS₂ particles.

* Corresponding author:

E-mail address: mahdymirzaaghai@yahoo.com

1. Introduction:

Metal matrix composites with solid lubricants have attracted wide and promising applications [1-7]. Aluminides have served interesting properties such as high hardness, high-temperature stability, high creep resistance, high melting point and, low density [8,9]. A Combination of aluminides with solid lubricants particles has been considered as self-lubricating materials [10-16]. Solid lubricants have been classified into several subdivisions, such as lamellar solids (e. g., MoS₂, WS₂ and, graphite), soft metals (e. g., Ag and Pb), carbon-based solids (e. g., diamond and DLC), and organic materials/polymers (e. g., PTFE and waxes) [10-17]. MoS₂ has a lamellar structure, the bonding in the S-Mo-S sandwich is covalent and strong, but the layers of the lamellar structure are van der Waals and weak. It yields a low friction coefficient value and is mostly used in applications that need a solid lubricant [15-17]. The friction coefficient increases and the lifetime decreases when MoS₂ is used in humid air, therefore; this material can be only used in vacuum and in a water vapor-free environment [15-21]. In a previous study, composite coating of Cu-Ni₃Al-MoS₂ made using the PVD method and a complex target showed a coefficient of friction of about 0.5 after 60 minutes [16]. In this design, it is predicted that by removing copper, the coating will have a higher hardness and its tribological properties will be improved, So this

study aimed to synthesize Ni₃Al-MoS₂ coating by magnetron sputtering, and The tribological behavior of the coating was evaluated.

2. Experimental

2.1. Deposition

The Ni₃Al powder was synthesized by ball milling of elemental Ni (80-100µm, 99.9% purity) and Al (80-100µm, 99.9% purity) using planetary ball mill for 40 hours at a speed of 350rpm at room temperature under Ar atmosphere. The MA product was characterized by X-ray diffraction (Bruker X'PERT MPD diffractometer) using filtered Co K α radiation ($\lambda=0.1789\text{\AA}$), Ni₃Al-30wt.%MoS₂ composite tablets (30mm in diameter and thickness of 2mm) were made by single-axis Santam press under 350 MPa stress. Finally, five tabs were placed in a pure Cu holder which was covered by aluminum foil to prevent the copper element from penetrating into the coating. Depending on the coating conditions and the type of process used, the alumina formed on the foil acts as an insulator and the possibility of its penetration into the coating is reduced [22]. Ni₃Al-MoS₂ coating was deposited by DC magnetron sputtering on 4340 steel substrates. Fig.1 is a schematic diagram of the magnetron sputtering process with Ni₃Al-MoS₂ target tablets. Table 1 shows the coating deposition conditions.

Table 1 Shows the coating deposition parameters.

Target	Ni ₃ Al-MoS ₂
Substrate	4340
Substrate temperature	325°C
Substrate to target distance	15Cm
Voltage	850V
Current	1.2-2A
Deposition time	80min
Base pressure	10 ⁻⁷ mbar
Working pressure	1-5×10 ⁻³ mbar

The composite coatings with a thickness of 8µm were obtained by sputtering for 80 min. The Ni₃Al-MoS₂ coatings were examined by both X-ray diffraction (Philips X'PERT MPD CuK α) and scanning electron microscopy (SEM Leo 440i OXFORD).

2.2 Testing:

2.2.1. Tribological properties measurements

The tribological properties of 4340 steel substrate and composite coatings were studied by a ball-on-disc tribometer. Table 2 shows the initial conditions of the samples.

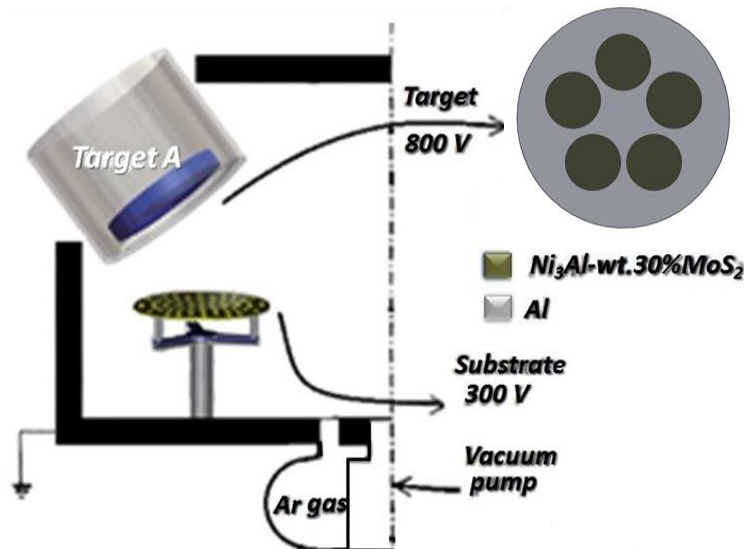


Fig.1. Schematic diagram of sputtering system for synthesizing Ni₃Al-MoS₂ composite coating.

Table 2 Different samples

Samples	Type	Hardness	Roughness (μm)
1	4340 steel	50HRC	$R_a = 0/2$
2	4340 steel with Ni ₃ Al-MoS ₂ coating	408HV	$R_a = 0/08$

All tests were carried out using a 5 mm diameter Si₃N₄ ball as the counterface. The tests were run under a load of 5 N at room temperature and a sliding speed of 0.1 m/s. The sliding load in the tribological test was monitored and recorded for 3600 seconds in order to determine the friction coefficient vs. time. The wear tracks of the coatings were examined by means of SEM.

2.2.2. Hardness measurement:

The hardness of the substrate was determined using a Rockwell C hardness with a Koopa attachment. The hardness measurements of the coatings were conducted according to ASTM 578-87 standard, using Wilson microhardness with Vickers diamond pyramid indenter under 25gr force in several points.

2.2.3. Roughness survey:

To determine the roughness of the substrate and coating surfaces was determined by a Mahr Germany device (M300C model).

2.2.4. Adhesion strength

The VDI 3198 standard specifies the well-known Rockwell C indentation test as a destructive quality test for coated compounds [23]. This technique does not give any absolute measurement of adhesion, but comparative results can be obtained with the same load for all samples. Fig. 2 gives qualitative adhesion properties considering the crack network from the indentation spot. This test also gives a qualitative measure of the toughness of the coating. The reported adhesion value ranges between HF1 to HF6 (HF is the German short form of adhesion strength) (Fig.2), with excellent adhesion property and a few crack networks in HF1 and the poorest adhesion properties indicating complete delamination of the coating in HF6 [24,25]

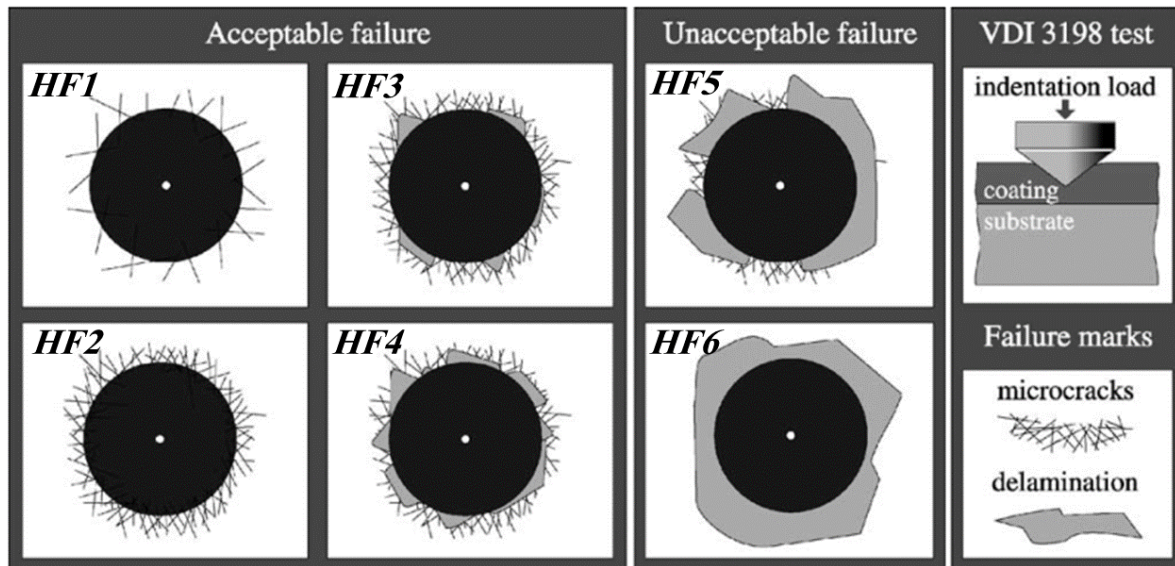


Fig.2. Adhesion strength quality based on Rockwell C indentation test [24].

3. Results and discussion

Fig. 3 indicates that the coating has a good flat surface. The observed bumps are a result of MoS₂ dots. A typical SEM image obtained from the surface and the elemental map of the Ni₃Al-MoS₂ composite coatings are shown in Fig.4. The chemical compositions which are determined by energy

dispersive spectroscopy (EDS) on SEM are given in table 3. Fig.5 shows backscatter electron (BSE) micrographs. The dark areas in the BSE image are MoS₂ because MoS₂ has a lower atomic mass. The Ni₃Al-MoS₂ composite coatings exhibit a dense structure. The thickness of the coating at the highest target current of 2A was 8μm. The measured microhardness of this coating was 408 HV.

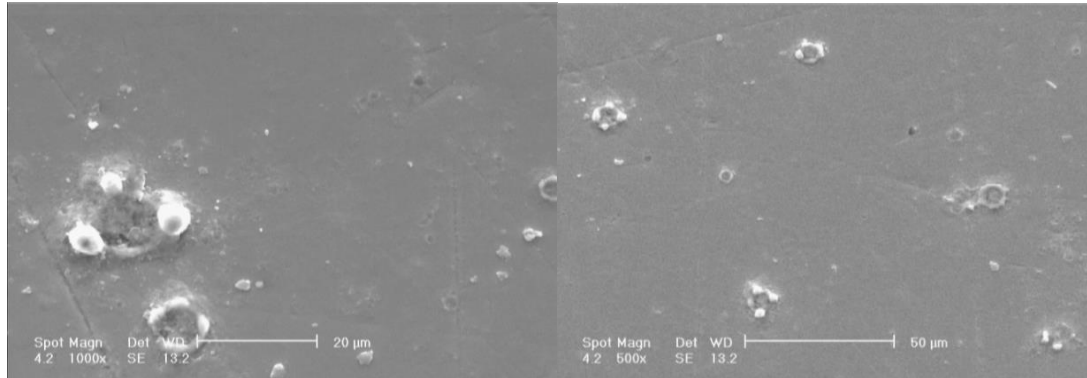


Fig.3. SEM images showing the surface of the Ni₃Al-MoS₂ composite coating.

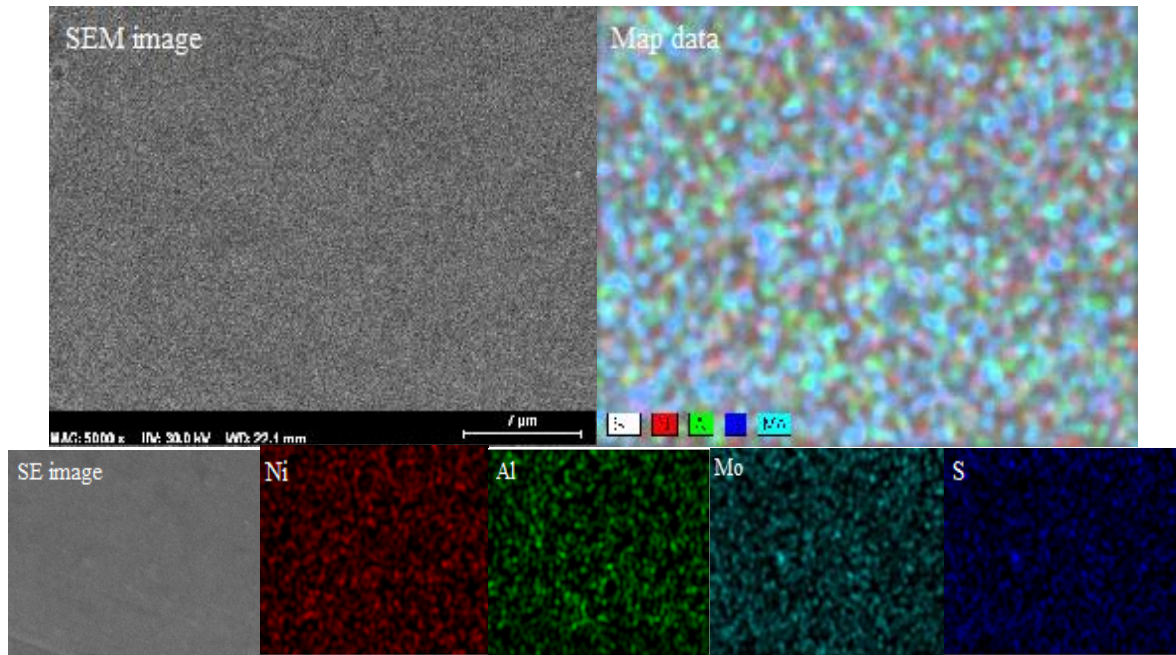


Fig. 4. SEM images showing the elemental map data of the Ni₃Al-MoS₂ composite coating.

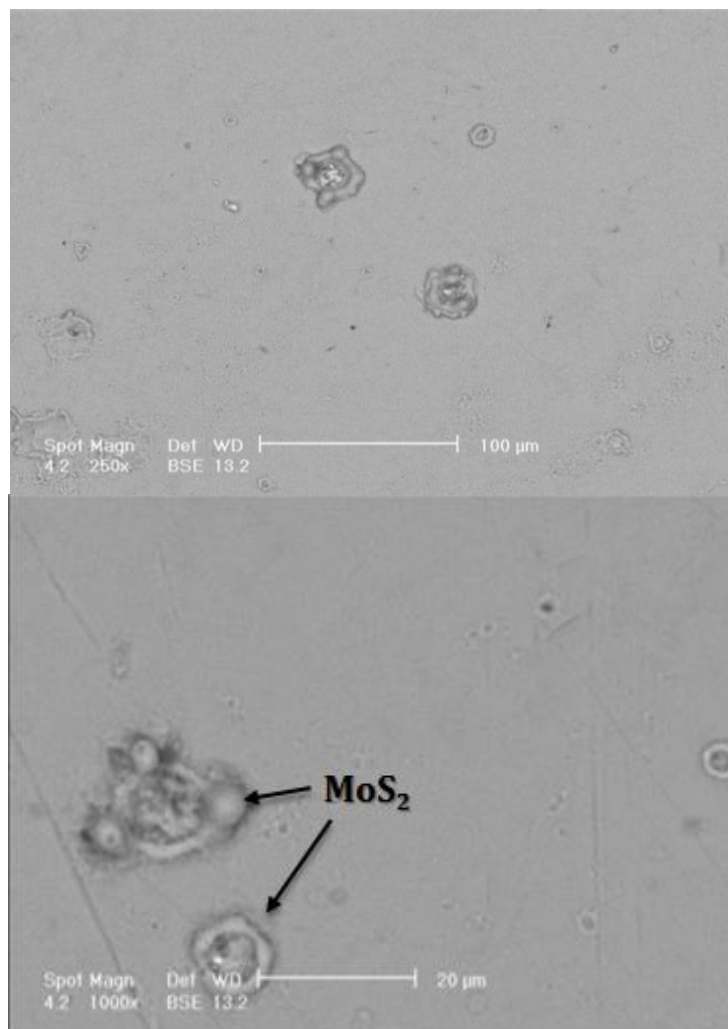
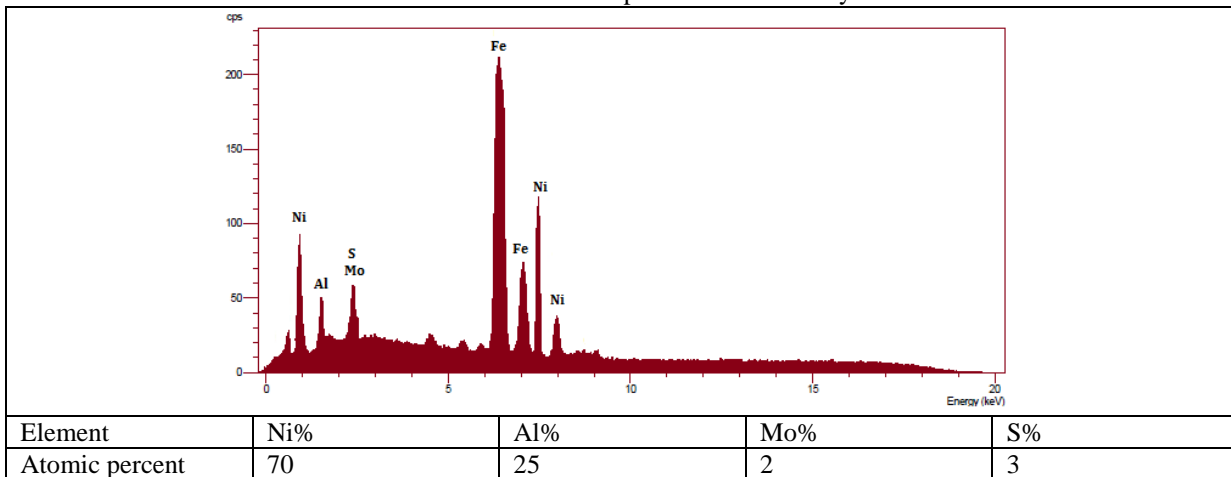


Fig. 5. BSE image of the Ni₃Al-MoS₂ composite coating.

Table 3 The chemical composition measured by EDS



3.1. XRD analyses

The X-ray diffraction pattern of Ni₃Al-MoS₂ composite coating is shown in Fig.6. The X-ray diffraction profile revealed that the coatings were

mainly consisted of Ni₃Al and MoS₂ phases, with no preferred orientation. Diffraction peaks of AlNi can be observed besides Ni₃Al. One definition can be the Al foil, which has covered the target surface.

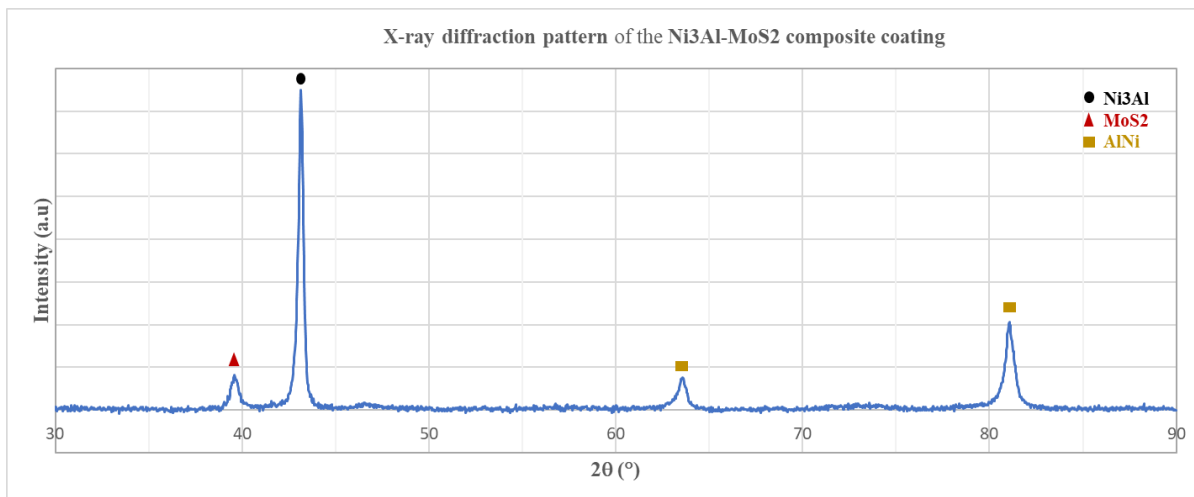


Fig. 6. XRD pattern of Ni₃Al-MoS₂ Composite Coating.

3.2. Adhesion strength

Fig.7 shows the optical micrographs of Rockwell-C indentation on Ni₃Al-MoS₂ coating. The Rockwell-C indentation test showed an acceptable adhesion.

According to the standards presented in the previous section [23-25], coating adhesion strength was evaluated to be HF3, which represents good adhesion and strength to the substrate.

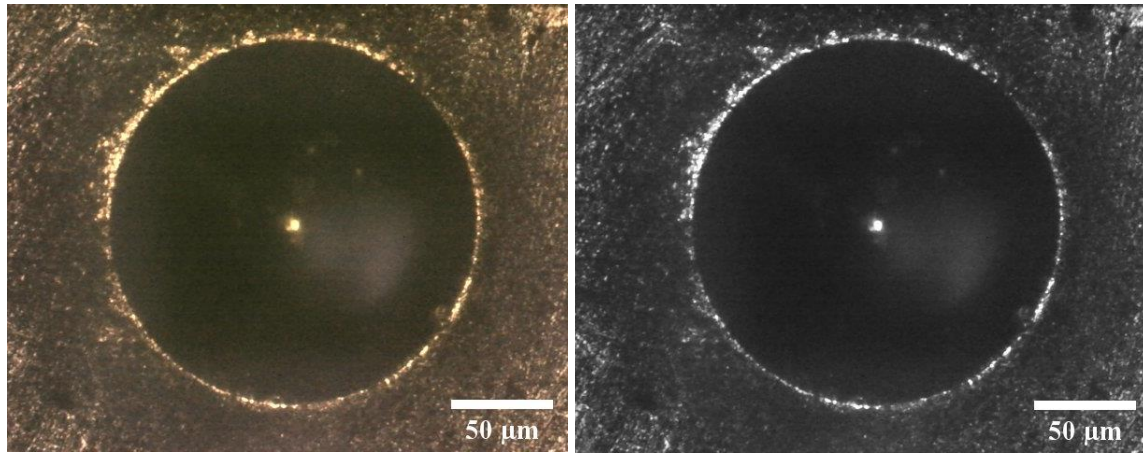


Fig. 7. Rockwell C adhesion test of Ni₃Al-MoS₂ coating (load 150kg).

3.3. Tribological properties measurements

Fig.8 (a) illustrates the evolution of the friction coefficient of the composite coating under dry sliding for the duration of 1 h at a sliding speed 0.1 m/s and an applied load of 5 N. The friction coefficients of the coating were approximately 0.2 in 25 °C. In comparison, the friction coefficients of the 4340-steel substrate were much higher (above 0.9) than that of the coating. These results prove that the Ni₃Al-MoS₂

coating exhibits excellent self-lubricating properties. Fig.8 (b) shows the mass loss results. The mass losses of substrate and coating were 0.02 and 0.005 gr, respectively. Humidity has a positive effect on friction coefficient, and decreases wear life which is probably because of dangling unsaturated bonds on the edge of basal plans reacting with moisture and oxygen in the environment to form tribooxidation products, such as MoO₃ [26-28].

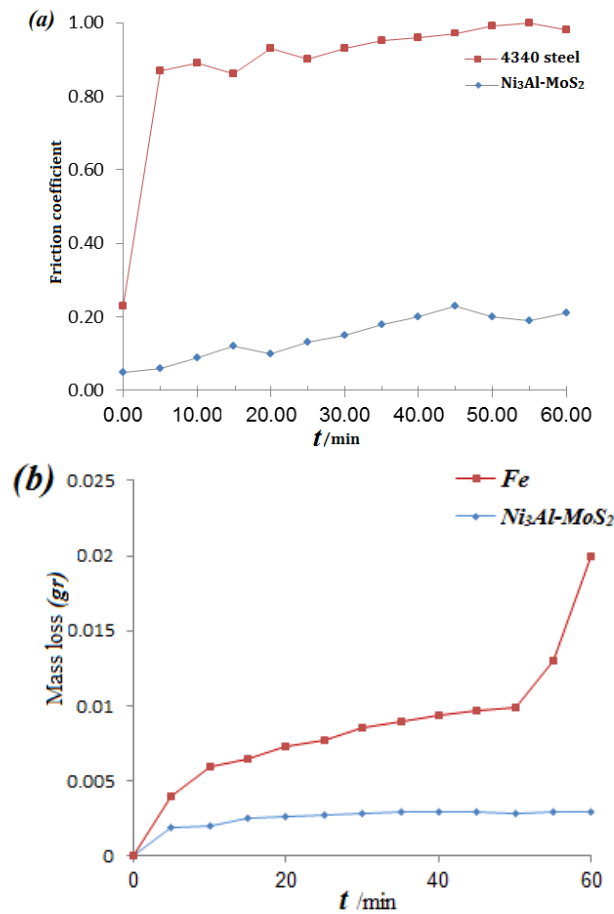


Fig. 8. (a)The friction coefficients and (b) mass loss of the coating at room temperature

Fig. 9 (a) shows the worn surfaces of the coating after wearing for 1 h at a load of 5 N and sliding speed of 0.1 m/s at room temperatures. The parallel furrows and spallation are observed, which reveal that the wear mechanism is abrasive. Fig. 9(b) given the EDS data taken from the wear area. EDS analysis was performed to determine the surface composition in the wear track. EDS confirmed the presence of Ni, Al, Mo and, S within the composite coating (Table 4). The worn area on the film counter body is smooth with patchy and powdery debris. Some worn debris piled up at both sides of the wear track with no abrasive wear effect. This is the reason why the friction coefficient remained very stable during the 1

h sliding test. The overall aspects of this worn surface image are typical for all coating studied here. The wear resistance of coatings depends on several factors, including the hardness, thickness, plastic deformation behavior, roughness and, lubricating properties. By properly adjusting these parameters, the wear behavior can be improved [29]. The microhardness test on the coating indicates that the coating hardness was 408 HV; due to the lower hardness of coating in comparison with the substrate, the coating half-life is low. However, the amount of lubricant material MoS₂ provides the condition for improving the lubrication.

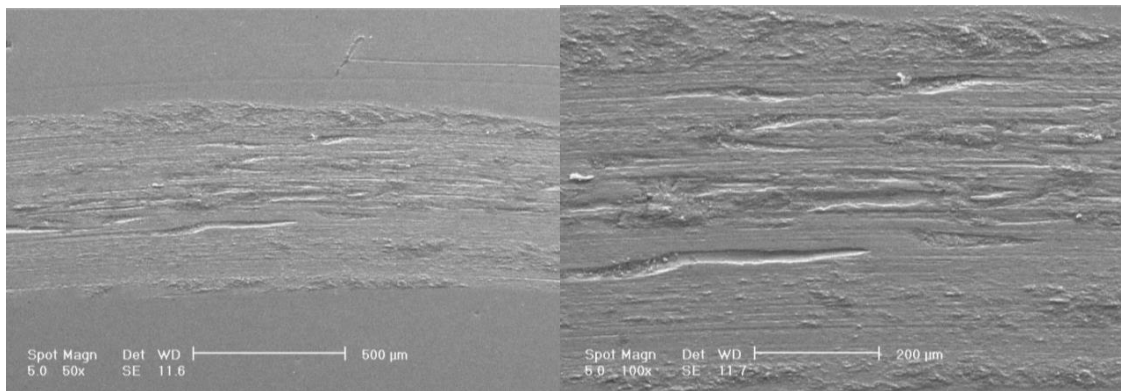
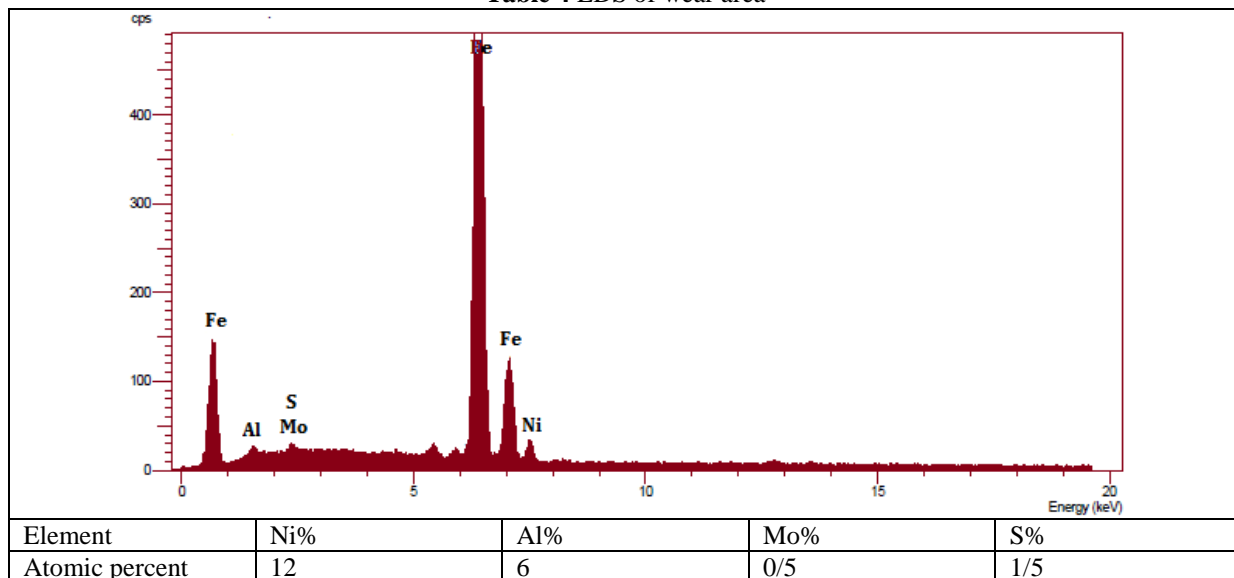


Fig. 9. SEM micrographs of worn surface of the coating (0.1 m/s, 5 N and 1 h).

Table 4 EDS of wear area



3.4. Investigation wear rate of the coating and substrate

Fig. 10 shows the wear rate of the as-received substrate and Ni₃Al-MoS₂ coating. The presence of the soft MoS₂ particles within the hard Ni₃Al matrix

and the smoothness of the surface, and the good adhesion strength of the coating to the substrate all contribute to the improvement of the substrate tribological properties reduces the wear rates. The wear rate of the coating was 50% smaller than that for the substrate.

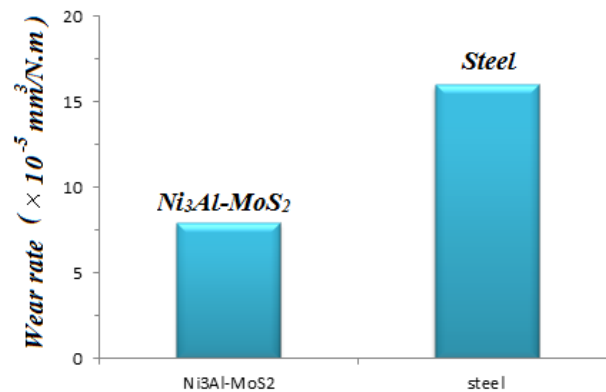


Fig.10. Wear rate of coating and substrate

4. Conclusions

XRD analysis indicated that the composite coating had no preferred orientation. In the BSE image, the dark area is the MoS₂ phase observed. The first coefficient of friction at room temperature is 0.24. These results prove that the coating provides a stable and low friction coefficient in stable conditions; in other words, it proves the coating exhibits self-lubricating properties. The main reason for the low coefficient of friction seems to be the presence of a composite structure containing hard matrix Ni₃Al with solid lubricant MoS₂. In addition, no failure(s) were observed during the wear test.

Acknowledgments

The authors are profoundly grateful to Freshte Surani for her generous help in this work.

References

- [1] S. Sun, J. Chen, Y. Wang, L. Wang, and Z. Sun, "Structural sensitivity of MoS₂-based films in solid space lubrication," *Surface Engineering*, vol. 36, pp. 106-113, 2020/01/02 2020.
- [2] Freschi, M., Di Virgilio, M., Zanardi, G., Mariani, M., Lecis, N., and Dotelli, G., 2021, "Employment of Micro- and Nano-WS₂ Structures to Enhance the Tribological Properties of Copper Matrix Composites," *Lubricants*, 9(5).
- [3] H. Torres, H. Rojacz, L. Čoga, M. Kalin, and M. Rodríguez Ripoll, "Local mechanical and frictional properties of Ag/MoS₂-doped self-lubricating Ni-based laser claddings and resulting high temperature vacuum performance," *Materials & Design*, vol. 186, p. 108296, 2020/01/15/ 2020.
- [4] M. S. Libório, G. B. Praxedes, L. L. F. Lima, I. G. Nascimento, R. R. M. Sousa, M. Naeem, et al., "Surface modification of M2 steel by combination of cathodic cage plasma deposition and magnetron sputtered MoS₂-TiN multilayer coatings," *Surface and Coatings Technology*, vol. 384, p. 125327, 2020/02/25/ 2020.
- [5] H. Du, C. Sun, W. Hua, T. Wang, J. Gong, X. Jiang, et al., "Structure, mechanical and sliding wear properties of WC-Co/MoS₂-Ni coatings by detonation gun spray," *J. Mater. Sci. Eng: A*. 445-446 (2007) 122-134.
- [6] Rajesh Kumar, L., Saravanakumar, A., Bhuvanewari, V., Jithin Karunan, M. P., Karthick Raja, N., and Karthi, P., 2020, "Tribological Behaviour of AA2219/MoS₂ Metal Matrix Composites under Lubrication," *AIP Conf. Proc.*, 2207(February).
- [7] Devaganesh, S., Kumar, P. K. D., Venkatesh, N., and Balaji, R., 2020, "Study on the Mechanical and Tribological Performances of Hybrid SiC-Al7075 Metal Matrix Composites," *J. Mater. Res. Technol.*, 9(3), pp. 3759-3766.
- [8] Liu, C., Chen, Y., Qiu, L., Liu, H., Bai, M., and Xiao, P., 2020, "The Al-Enriched γ' -Ni₃Al-Base Bond Coat for Thermal Barrier Coating Applications," *Corros. Sci.*, 167(2517), p. 108523.
- [9] Yang, Z. W., Lian, J., Wang, J., Cai, X. Q., Wang, Y., Wang, D. P., Wang, Z. M., and Liu, Y. C., 2020, "Diffusion Bonding of Ni₃Al-Based Alloy Using a Ni Interlayer," *J. Alloys Compd.*, 819, p. 153324.
- [10] K. P. Furlan, J. D. B. de Mello, and A. N. Klein, "Self-lubricating composites containing MoS₂: A review," *Tribology International*, vol. 120, pp. 280-298, 2018/04/01/ 2018.
- [11] S. Zhu, J. Cheng, Z. Qiao, and J. Yang, "High temperature solid-lubricating materials: A review," *Tribology International*, vol. 133, pp. 206-223, 2019/05/01/ 2019.
- [12] Yuan, J., Ph, D., Wang, Q., Liu, X., Lou, S., Li, Q., and Wang, Z., 2020, "Microstructures and High-Temperature Wear Behavior of NiAl / WC-Fe x Coatings on Carbon Steel by Plasma Cladding," *J. Alloys Compd.*, 842, p. 155850.
- [13] Shi, X., Song, S., Zhai, W., Wang, M., Xu, Z., Yao, J., Qamar ud Din, A., and Zhang, Q., 2014,

“Tribological Behavior of Ni3Al Matrix Self-Lubricating Composites Containing WS₂, Ag and HBN Tested from Room Temperature to 800°C,” *Mater. Des.*, 55, pp. 75–84.

[14] Yao, Q., Jia, J., Chen, T., Xin, H., Shi, Y., He, N., Feng, X., Shi, P., and Lu, C., 2020, “High Temperature Tribological Behaviors and Wear Mechanisms of NiAl-MoO₃/CuO Composite Coatings,” *Surf. Coatings Technol.*, 395(March), p. 125910.

[15] Dong, C., Cui, Q., Gao, X., Jiang, D., Fu, Y., Wang, D., Weng, L., Hu, M., and Sun, J., 2020, “Tribological Property of MoS₂-Cr₃O₄ Nanocomposite Films Prepared by PVD and Liquid Phase Synthesis,” *Surf. Coatings Technol.*, 403(July), p. 126382.

[16] Mirzaaghaei, M., Enayati, M. H., and Ahmadi, M., 2016, “The Tribological Properties of Cu-Ni 3 Al-MoS₂ Composite Coating Deposited by Magnetron Sputtering,” 4(4), pp. 37–45.

[17] A. Erdemir, in: B. Bhushan (Eds.), *Modern Tribology Handbook*, vol. II, CRC Press, Boca Raton, FL, 2001, p. 736.

[18] E. Arslan, F. Bülbül, A. Alsaran, A. Celik, and I. Efeoglu, The effect of deposition parameters and Ti content on structural and wear properties of MoS₂Ti coatings, *Wear* 259 (2005) 814-819.

[19] F. Bülbül, İ. Efeoglu, E. Arslan, The effect of bias voltage and working pressure on S/Mo ratio at MoS₂-Ti composite films, *Appl. Surf. Sci.* 253 (2007) 4415-4419.

[20] N. M. Renevier, V. C. Fox, D. G. Teer, J. Hampshire, Coating characteristics and tribological properties of sputter-deposited MoS₂/metal composite coatings deposited by closed field

unbalanced magnetron sputter ion plating, *Surf. Coat. Technol.* 127 (2000) 24-37.

[21] W. Heinke, A. Leyland, A. Matthews, G. Berg, C. Friedrich, E. Broszeit, Evaluation of PVD nitride coatings, using impact, scratch and Rockwell-C adhesion tests, *Thin Solid Films* 270 (1995) 431-438.

[22] S. Tokumaru and M. Hashimoto, "High resistivity AlO_x thin films deposited by a novel two-step sputtering process," *Surface and Coatings Technology*, vol. 54-55, pp. 303-307, 1992/11/16/1992.

[23] Verein Deutscher Ingenieure Normen, VDI 3198, VDI-Verlag, Dusseldorf, 1991.

[24] Vidakis N., Antoniadis A., and Bilalis N., The VDI 3198 in dentationtest evaluation of areliable qualitative control for layered compounds. *J. Mater. Proc. Technol.*, pp. 143-144, 2003.


[25] Heinke W., Leyland A., Matthews A., Berg G., Friedrich C., and Broszeit E., Evaluation of PVD nitrid ecoatings, using impact, scratch and Rockwell-C adhesion tests. *Thin Solid Films.*, pp. 431-270, 1995.

[26] Brainard, W.A. (1969) The thermal stability and friction of the disulfides, diselenides and ditellurides of molybdenum and tungsten in vacuum (10⁻⁹ to 10⁻⁶ torr). NASA TN D-5141.

[27] H. E. Sliney, Solid lubricant materials for high temperatures—a review, *Tribol. Int.* 15 (1982) 303-315.

[28] S. V. Prasad, J. S. Zabinski, Tribology of tungsten disulphide (WS₂): characterization of wear-induced transfer films, *J. Mater. Sci. Lett.* 12 (1993) 1413-1415.

[29] T. W. Scharf, S. V. Prasad, Solid lubricants: a review, *J. Mater. Sci.* 48 (2010) 511-513.

 DOR: 20.1001.1.2322388.2021.9.1.4.0

Research Paper

Influence of Power Law Distribution with Pressure on the Frequencies of Supported Functionally Graded Material Cylindrical Shell with C-SL and F-SS Boundary Conditions

Mohammadreza Isvandzibaei*

Department of Mechanical Engineering, Andimeshk Branch, Islamic Azad University, Andimeshk, Iran

ARTICLE INFO

Article history:

Received 24 July 2020
Accepted 6 August 2020
Available online 1 January 2021

Keywords:

Power law distribution
Frequency
Pressure
Cylindrical Shell
FGM

ABSTRACT

In this paper, influence power-law distribution with pressure on frequencies of the supported functionally graded cylindrical shell is studied. This shell is constructed from a functionally graded material (FGM) with two constituent materials. FGMs are graded through the thickness direction, from one surface of the shell to the next. The supported FGM shell equations are created based on FSDT. The governing equations of the movement were utilized by the Ritz method. The boundary conditions are clamp-sliding and free-simply support. The influence of the various values of the power-law distribution with pressure supported and different conditions on the frequencies characteristics are studied. This study shows that the frequencies decreased with the increase in the amounts of the power-law distribution with pressure. Thus, the constituent power-law distribution with pressure effects on the frequencies. The results show the frequencies with different power-law distribution under pressures are various for different conditions.

* **Corresponding author:**

E-mail address: esvandzibaei@yahoo.com

1. Introduction

In all of the world, applications of cylindrical shells have developed in science. Cylindrical shells have extensive applications in engineering and industry. The study of the vibratory response of cylindrical shells is very significant for the behavior and applications of these structures. Some of these applications are found in the aerospace, civil, mechanical, and maritime construction development [1].

Some researchers for eschew failure are used stiffener shells [2-7]. Vibration cylindrical shells are an important subject of research by scientists, and it was first presented via love [8]. Natural frequencies, several theories, and boundary conditions were introduced via Leissa [9], Blevins [10], Soedel [11], Chung [12], Reddy [13], and Forsberg [14].

Functionally graded materials (FGMs) are constructed by mixing various materials, and they are graded in thickness. These materials comprise a blend of metal and ceramic or other different materials. Also, the physical properties of one level vary from the other level, and these materials are generated by the composition of two or more materials.

For the sample, one level has thermo resistant, and the other level has mechanical properties. The main benefit of FGMs is their application in environments with high temperatures. FGM structures are utilized as coatings space schemes, spacecraft, reactors, turbines, components in engines, and others [15]. Research on the shells made of FGM is significant in the engineering applications.

The significant research on FGM shell was reported by Loy [16]. The finite element method on FGM cylindrical shells was used by Patel et al. [17]. Study frequencies with effects of radius published by Zhi and Hu [18]. Arshad et al. [19] and Shah et al. [20] investigated the frequency characteristic of FGM cylindrical shells. Hosseini et al. [21] investigated rotating functionally graded cylindrical shell. Amirabadi et al. [22] studied vibration FGM GPL-reinforced truncated thick conical shells under different boundary conditions. They showed that dispersing more GPL reinforcements near the inner and outer surfaces of the rotating shells leads to a remarkable increase in both forward and backward wave frequencies. Mohammadi et al. [23] investigated numerical investigation of nonlinear vibration analysis for triple-walled carbon nanotubes conveying viscous fluid. Amirabadi et al. [24] studied wave propagation in rotating functionally graded GPL-reinforced cylindrical shells based on the third-order shear deformation theory.

The object of this study is to the analysis influence of power-law distribution with pressure on frequencies of the supported functionally graded cylindrical shell. The

analysis is done based on the first-order theory. The governing equations of the movement were utilized by Ritz method. The boundary conditions are clamp-sliding (C-SL) and free-simply support (F-SS).

The influence of the various values of the power-law distribution with pressure supported and different conditions on the frequencies characteristics are discussed. The accuracy of this procedure is confirmed by comparisons the present results with other ones that existed in literature.

2. Functionally Graded Materials

FGMs are made of the variation of composition and different materials. The volume fraction distribution of each phase of material varies with a specific gradient. The E_{fgm}, ν_{fgm} and ρ_{fgm} are given as:

$$E_{fgm}(T, z) = (E_2(T) - E_1(T)) \left(z + \frac{h}{2} / h \right)^N + E_1(T) \quad (1)$$

$$\nu_{fgm}(T, z) = (\nu_2(T) - \nu_1(T)) \left(z + \frac{h}{2} / h \right)^N + \nu_1(T) \quad (2)$$

$$\rho_{fgm}(T, z) = (\rho_2(T) - \rho_1(T)) \left(z + \frac{h}{2} / h \right)^N + \rho_1(T) \quad (3)$$

3. First order Shear Deformation Theory

Consider figure 1, in which a geometrical sketch of reinforced FGM cylindrical shell under pressure is given. The displacement field with first-order theory is written as

$$u(x, \theta, z) = u_0(x, \theta) + z\psi_x(x, \theta) \quad (4)$$

$$v(x, \theta, z) = v_0(x, \theta) + z\psi_\theta(x, \theta)$$

$$w(x, \theta, z) = w_0(x, \theta)$$

The strain displacement relationships are expressed by

$$\epsilon_{11} = \frac{1}{A_1} \frac{\partial u(x, \theta, z)}{\partial x} + \frac{1}{A_1 A_2} \frac{\partial A_1}{\partial \theta} v(x, \theta, z) + \frac{w(x, \theta, z)}{R_1} \quad (5)$$

$$\epsilon_{22} = \frac{1}{A_2} \frac{\partial v(x, \theta, z)}{\partial \theta} + \frac{1}{A_1 A_2} \frac{\partial A_2}{\partial x} u(x, \theta, z) + \frac{w(x, \theta, z)}{R_2} \quad (6)$$

$$\epsilon_{12} = \frac{A_2}{A_1} \frac{\partial}{\partial x} \left(\frac{v(x, \theta, z)}{A_2} \right) + \frac{A_1}{A_2} \frac{\partial}{\partial \theta} \left(\frac{u(x, \theta, z)}{A_1} \right) \quad (7)$$

$$\epsilon_{13} = A_1 \frac{\partial}{\partial z} \left(\frac{u(x, \theta, z)}{A_1} \right) + \frac{1}{A_1} \frac{\partial w(x, \theta, z)}{\partial x} \quad (8)$$

$$\epsilon_{23} = A_2 \frac{\partial}{\partial z} \left(\frac{v(x, \theta, z)}{A_2} \right) + \frac{1}{A_2} \frac{\partial w(x, \theta, z)}{\partial \theta} \quad (9)$$

$$\epsilon_{33} = 0 \quad (10)$$

where A1 and A2 are the parameters of Lamé [25].

$$A_1 = \frac{\partial r}{\partial x} \quad A_2 = \frac{\partial r}{\partial \theta} \quad (11)$$

Substituting Eq. (4) into Eqs. (5-9), thus

$$\bar{\varepsilon}_{11} = \frac{\partial u_0(x, \theta)}{\partial x} + z \frac{\partial \psi_x(x, \theta)}{\partial x} \quad (12)$$

$$\bar{\varepsilon}_{22} = \frac{\partial v_0(x, \theta)}{R \partial \theta} + z \frac{\partial \psi_\theta(x, \theta)}{R \partial \theta} + \frac{w_0(x, \theta)}{R} \quad (13)$$

$$\bar{\varepsilon}_{12} = \frac{\partial v_0(x, \theta)}{\partial x} + \frac{\partial u_0(x, \theta)}{R \partial \theta} + z \left(\frac{\partial \psi_x(x, \theta)}{R \partial \theta} + \frac{\partial \psi_\theta(x, \theta)}{\partial x} \right) \quad (14)$$

$$\bar{\varepsilon}_{13} = \psi_x(x, \theta) + \frac{\partial w_0(x, \theta)}{\partial x} \quad (15)$$

$$\bar{\varepsilon}_{23} = \psi_\theta(x, \theta) + \frac{\partial w_0(x, \theta)}{R \partial \theta} \quad (16)$$

The stress-strain equations are written by $\{\bar{\sigma}\} = [\bar{Q}] \{\bar{\varepsilon}\}$ (17)

where $\{\bar{\sigma}\}^T = \{\bar{\sigma}_{11} \quad \bar{\sigma}_{22} \quad \bar{\sigma}_{12} \quad \bar{\sigma}_{13} \quad \bar{\sigma}_{23}\}$ (18)

$$\{\bar{\varepsilon}\}^T = \{\bar{\varepsilon}_{11} \quad \bar{\varepsilon}_{22} \quad \bar{\varepsilon}_{12} \quad \bar{\varepsilon}_{13} \quad \bar{\varepsilon}_{23}\} \quad (19)$$

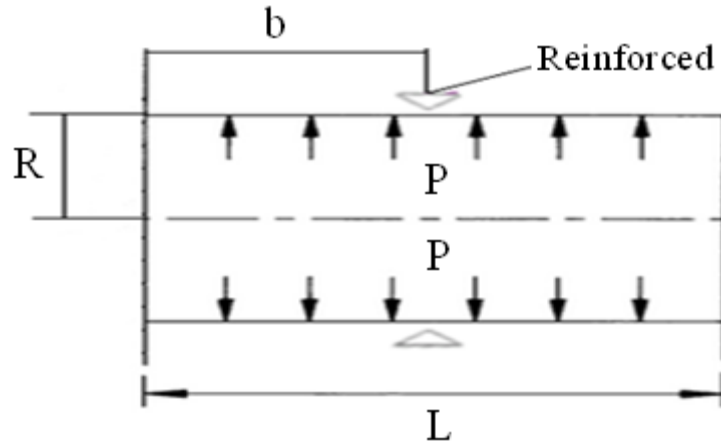


Fig. 1. The supported FGM cylindrical shell with pressure

$$[\bar{Q}] = \begin{bmatrix} \bar{Q}_{11} & \bar{Q}_{12} & 0 & 0 & 0 \\ \bar{Q}_{21} & \bar{Q}_{22} & 0 & 0 & 0 \\ 0 & 0 & \bar{Q}_{66} & 0 & 0 \\ 0 & 0 & 0 & \bar{Q}_{55} & 0 \\ 0 & 0 & 0 & 0 & \bar{Q}_{44} \end{bmatrix} \quad (20)$$

$$\bar{Q}_{55} = K \frac{E(z)}{2(1-\nu(z))} \quad A = 1 + \frac{z}{R} \quad (25)$$

where $K = 5/6$ [26].

The moment resultants are:

$$\{N_x, N_\theta, N_{x\theta}, H_x, H_\theta\} = \int_{-h/2}^{h/2} \{\bar{\sigma}_{11} \quad \bar{\sigma}_{22} \quad \bar{\sigma}_{12} \quad \bar{\sigma}_{13} \quad \bar{\sigma}_{23}\} dz \quad (26)$$

$$\{M_x, M_\theta, M_{x\theta}\} = \int_{-h/2}^{h/2} \{\bar{\sigma}_{11} \quad \bar{\sigma}_{22} \quad \bar{\sigma}_{12}\} z dz \quad (27)$$

Applying Eqs.(12-16) into Eq.(21) and substituting in Eqs.(26) and (27) the following equation is got

$$\{N\} = [I] \{\bar{\varepsilon}\} \quad (28)$$

where $\{N\}$, $\{\bar{\varepsilon}\}$ and $[I]$ are

$$\{N\}^T = \{N_x, N_\theta, N_{x\theta}, M_x, M_\theta, M_{x\theta}, H_x, H_\theta\} \quad (29)$$

$$\{\bar{\varepsilon}\}^T = \{\bar{\varepsilon}_{11} \quad \bar{\varepsilon}_{22} \quad \bar{\varepsilon}_{12} \quad \bar{\varepsilon}_{13} \quad \bar{\varepsilon}_{23}\} \quad (30)$$

Then equation (17) can be expressed as

$$\begin{Bmatrix} \bar{\sigma}_{11} \\ \bar{\sigma}_{22} \\ \bar{\sigma}_{12} \\ \bar{\sigma}_{13} \\ \bar{\sigma}_{23} \end{Bmatrix} = \begin{bmatrix} \bar{Q}_{11} & \bar{Q}_{12} & 0 & 0 & 0 \\ \bar{Q}_{21} & \bar{Q}_{22} & 0 & 0 & 0 \\ 0 & 0 & \bar{Q}_{66} & 0 & 0 \\ 0 & 0 & 0 & \bar{Q}_{55} & 0 \\ 0 & 0 & 0 & 0 & \bar{Q}_{44} \end{bmatrix} \begin{Bmatrix} \bar{\varepsilon}_{11} \\ \bar{\varepsilon}_{22} \\ \bar{\varepsilon}_{12} \\ \bar{\varepsilon}_{13} \\ \bar{\varepsilon}_{23} \end{Bmatrix} \quad (21)$$

The stiffness is written as

$$\bar{Q}_{11} = \frac{E(z)}{1-\nu^2(z)}, \quad \bar{Q}_{12} = \frac{\nu(z)E(z)}{A(1-\nu^2(z))} \quad (22)$$

$$\bar{Q}_{21} = \frac{\nu(z)E(z)}{1-\nu^2(z)}, \quad \bar{Q}_{22} = \frac{E(z)}{A(1-\nu^2(z))} \quad (23)$$

$$\bar{Q}_{66} = \frac{E(z)}{2A(1-\nu(z))}, \quad \bar{Q}_{44} = K \frac{E(z)}{2(1-\nu(z))} \quad (24)$$

$$[I] = \begin{bmatrix} X_{11} & X_{12} & X_{16} & Y_{11} & Y_{12} & Y_{16} & 0 & 0 \\ X_{12} & X_{22} & X_{26} & Y_{12} & Y_{22} & Y_{26} & 0 & 0 \\ X_{16} & X_{26} & X_{66} & Y_{16} & Y_{26} & Y_{66} & 0 & 0 \\ Y_{11} & Y_{12} & Y_{16} & Z_{11} & Z_{12} & Z_{16} & 0 & 0 \\ Y_{12} & Y_{22} & Y_{26} & Z_{12} & Z_{22} & Z_{26} & 0 & 0 \\ Y_{16} & Y_{26} & Y_{66} & Z_{16} & Z_{26} & Z_{66} & 0 & 0 \\ 0 & 0 & 0 & 0 & 0 & 0 & kV_{44} & kV_{45} \\ 0 & 0 & 0 & 0 & 0 & 0 & kV_{45} & kV_{55} \end{bmatrix} \quad (31)$$

in which X_{ij}, Y_{ij}, Z_{ij} and V_{ij} are

$$(X_{ij}, Y_{ij}, Z_{ij}) = \int_{-h/2}^{h/2} Q_{ij}(1, Z, Z^2) dz \quad V_{ij} = K \int_{-h/2}^{h/2} Q_{ij} dz \quad (32)$$

4 Energy Equations

The strain energy is expressed as

$$U = \frac{1}{2} \int_0^L \int_0^{2\pi} \left\{ \begin{matrix} \varepsilon \\ \varepsilon \end{matrix} \right\}^T [II] \left\{ \begin{matrix} \varepsilon \\ \varepsilon \end{matrix} \right\} R d\theta dx \quad (33)$$

The kinetic energy is given by

$$T = \frac{1}{2} \int_0^L \int_0^{2\pi} \rho T \left\{ \left(\frac{\partial u_0(x, \theta)}{\partial t} \right)^2 + \left(\frac{\partial v_0(x, \theta)}{\partial t} \right)^2 + \left(\frac{\partial w_0(x, \theta)}{\partial t} \right)^2 + \left(\frac{\partial \psi_x(x, \theta)}{\partial t} \right)^2 + \left(\frac{\partial \psi_\theta(x, \theta)}{\partial t} \right)^2 \right\} R d\theta dx \quad (34)$$

The potential energy of pressure is

$$V = \int_0^L \int_0^{2\pi} \frac{P}{2} \left\{ \frac{\partial^2 w_0(x, \theta)}{\partial \theta^2} + w_0(x, \theta) \right\} w_0(x, \theta) d\theta dx \quad (35)$$

Therefore, the energy functional can be written as

$$F = U - T + V \quad (36)$$

5 Boundary Conditions

The displacement field can be expressed as

$$\begin{aligned} u_0(x, \theta) &= \bar{E}_1 \frac{\partial \Omega(x)}{\partial x} \cos(n\theta) \cos(\omega t) \\ v_0(x, \theta) &= \bar{E}_2 \Omega(x) \sin(n\theta) \cos(\omega t) \\ w_0(x, \theta) &= \bar{E}_3 \Omega(x) \prod_{i=1}^H (x - b_i)^{\mu_i} \cos(n\theta) \cos(\omega t) \\ \psi_x(x, \theta) &= \bar{E}_4 \frac{\partial \Omega(x)}{\partial x} \cos(n\theta) \cos(\omega t) \\ \psi_\theta(x, \theta) &= \bar{E}_5 \Omega(x) \sin(n\theta) \cos(\omega t) \end{aligned} \quad (37)$$

where $\Omega(x)$ is beam function can be expressed as

$$\begin{aligned} \Omega(x) &= \Psi_1 \cosh\left(\frac{\Phi_m x}{L}\right) + \Psi_2 \cos\left(\frac{\Phi_m x}{L}\right) - \mu_m (\Psi_3 \sinh\left(\frac{\Phi_m x}{L}\right) \\ &+ \Psi_4 \sin\left(\frac{\Phi_m x}{L}\right)) \end{aligned} \quad (38)$$

6 Ritz Method

The energy functional, F expressed with Lagrangian function

$$F = U_{\max} - T_{\max} + V_{\max} \quad (39)$$

Substituting Eq. (37) in Eqs. (33), (34) and (35) and minimizing:

$$\left. \begin{aligned} \frac{\partial (U_{\max} - T_{\max} + V_{\max})}{\partial \bar{E}_1} &= 0 \\ \frac{\partial (U_{\max} - T_{\max} + V_{\max})}{\partial \bar{E}_2} &= 0 \\ \frac{\partial (U_{\max} - T_{\max} + V_{\max})}{\partial \bar{E}_3} &= 0 \\ \frac{\partial (U_{\max} - T_{\max} + V_{\max})}{\partial \bar{E}_4} &= 0 \\ \frac{\partial (U_{\max} - T_{\max} + V_{\max})}{\partial \bar{E}_5} &= 0 \end{aligned} \right\} \quad (40)$$

The governing equation with matrix form is

$$\begin{bmatrix} C_{11} & C_{12} & C_{13} & C_{14} & C_{15} \\ C_{21} & C_{22} & C_{23} & C_{24} & C_{25} \\ C_{31} & C_{32} & C_{33} & C_{34} & C_{35} \\ C_{41} & C_{42} & C_{43} & C_{44} & C_{45} \\ C_{51} & C_{52} & C_{53} & C_{54} & C_{55} \end{bmatrix} \begin{Bmatrix} \bar{E}_1 \\ \bar{E}_2 \\ \bar{E}_3 \\ \bar{E}_4 \\ \bar{E}_5 \end{Bmatrix} = \begin{Bmatrix} 0 \\ 0 \\ 0 \\ 0 \\ 0 \end{Bmatrix} \quad (41)$$

The determinant of matrix C equals to zero

$$|C_{ij}| = 0 \quad (42)$$

with solution equation (42):

$$\delta_0 \omega^{10} + \delta_1 \omega^8 + \delta_2 \omega^6 + \delta_3 \omega^4 + \delta_4 \omega^2 + \delta_5 = 0 \quad (43)$$

The equation (43) is consists of ten roots, and the smallest positive root is the natural frequency in the present research. The properties of materials are specified in Table 2.

Table 1 Values of Ψ_i, Φ_m and μ_m for asymmetric boundary conditions [5].

BC	$\Psi_i (i=1, \dots, 4)$	Φ_m	μ_m
C-SL	$\Psi_1 = 1, \Psi_2 = -1$ $\Psi_3 = 1, \Psi_4 = -1$	$(4m - 1)\pi / 4$	$\frac{\cosh \Phi_m - \cos \Phi_m}{\sinh \Phi_m - \sin \Phi_m}$
F-SS	$\Psi_1 = 1, \Psi_2 = 1$ $\Psi_3 = 1, \Psi_4 = 1$	$(4m + 1)\pi / 4$	$\frac{\cosh \Phi_m - \cos \Phi_m}{\sinh \Phi_m - \sin \Phi_m}$

Table 2 Mechanical properties of materials [16].

Coefficients of temperature	Stainless Steel			Nickel		
	$E(Nm^{-2})$	ν	$\rho(kgm^{-3})$	$E(Nm^{-2})$	ν	$\rho(kgm^{-3})$
Q^0	201.04×10^9	0.3262	8166	223.95×10^9	0.3100	8900
Q^{-1}	0	0	0	0	0	0
Q^1	3.079×10^{-4}	-2.002×10^{-4}	0	-2.794×10^{-4}	0	0
Q^2	-6.534×10^{-7}	3.797×10^{-7}	0	-3.998×10^{-9}	0	0
Q^3	0	0	0	0	0	0
Q	2.07788×10^{11}	0.317756	8166	2.05098×10^{11}	0.3100	8900

Table 3 Natural frequency of FGM cylindrical shell without support and pressure ($R = 1, N = 1, L/R = 20$).

h/R	m	n	Natural frequency (Hz)	
			Loy et al. [16]	Present
0.002	1	1	13.211	13.186
	1	2	4.480	4.4200
	1	3	4.1569	4.0346
	1	4	7.0384	7.0240
	1	5	11.241	11.124
	1	6	16.455	16.221
	1	7	22.635	22.306
	1	8	29.771	30.111
	1	9	37.862	37.560
	1	10	46.905	46.397

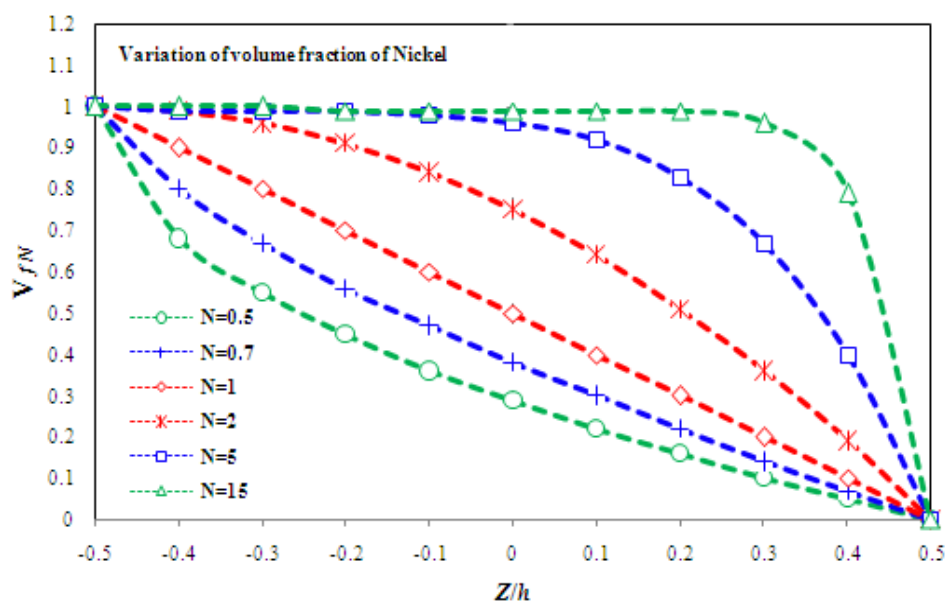


Fig. 2. Volume fraction of Nickel V_{fN} with thickness variable Z/h

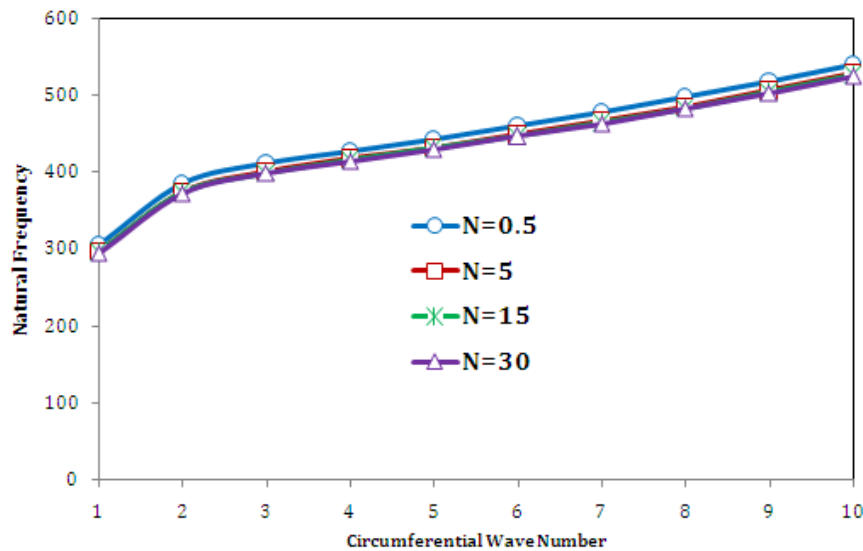


Fig. 3. Changes of frequency with support and pressure for different power law under C-SL (P = 700 KPa, h/R = 0.002, L/R = 20, b= 0.5L)

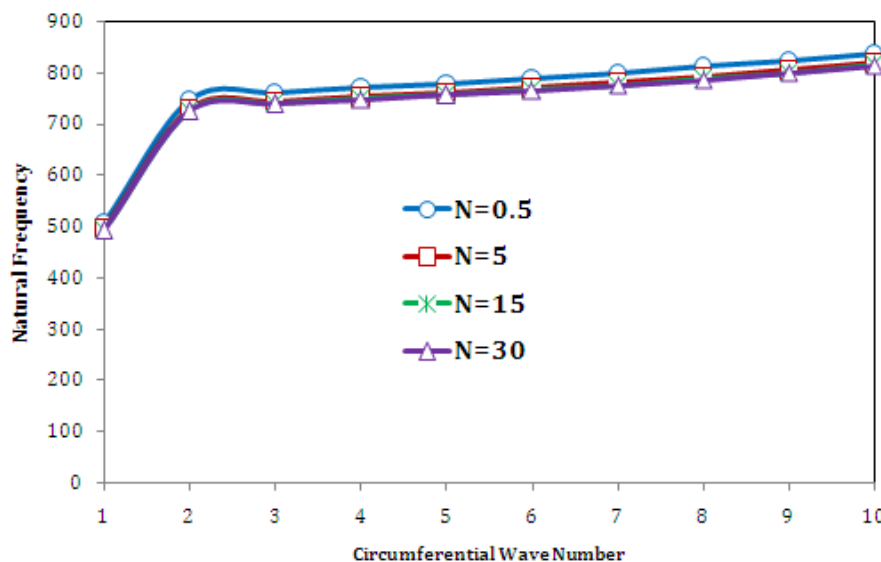


Fig. 4. Changes of frequency with support and pressure for different power law under F-SS (P = 700 KPa, h/R = 0.002, L/R = 20, b= 0.5L)

7 Comparison Study

To validate of the present study, the results of the FGM cylindrical shell without pressure and support are evaluated with the results in other literature. Table 3 shows the variation of the frequency for the FGM cylindrical shell without pressure and support with two different h/R ratios. The comparisons presented in Table 3, show good agreeable results with published works.

8 Results and Discussion

Variation of volume fractions of Nickel is shown in Fig. 2. In this figure the volume fraction of nickel V_{fN} decreased from value 1 at $z/h = -0.5$ to its least value 0 at $z/h = +0.5$. For $z/h < 0$ and $N < 1$, the decrease of V_{fN} is rapid. For $z/h < 0$ and $N > 1$, the rate of

decrease of V_{fN} is slow while for $z/h > 0$ and $N > 1$, it decreases rapidly. It is observed that the variations of the constituent material for FGMs are influenced by the volume fraction laws.

Tables 4 and 5 show variations of the frequency with different power-law distribution with pressure. The frequencies are discussed for different (N). In these tables, different values of power-law with pressures efficacy frequency of supported FGM cylindrical shell. In these tables, $m=1$ and it is mean first axial wave mode used in this analysis. For $m>1$ simulation result was found to yield similar trends for two asymmetric boundary conditions. The decrease in the frequencies from $N = 0.5$ to $N = 30$ is about 3.156% at $n = 1$ and 3.095% at $n = 10$. Therefore, the arrangement of constituent materials in FGMs will determine the

increment and decrements in the natural frequency with power-law distribution. The results show the natural frequencies for various power-law with pressure are various for boundary conditions.

Figures 3 and 4 depict a variation of frequency with support and pressure for a different power-law distribution. In both cases C–SL and F–SS, the frequencies for the different power-law with pressure increase with the circumferential wave number.

In these figures, when reinforcement is used, significant changes in the natural frequency are

observed at low circumferential wave numbers. It can be seen from these figures that the increase in natural frequency is significant when n increased from 1 to 2, and for n greater than 2, the natural frequency increases gradually as the circumferential wave number n is increased. The results show that power-law distribution has an effect on the natural frequency, and frequencies decreased with the increase in the power-law distribution.

Table 4 Variation of the natural frequency (Hz) with the different power-law exponent for C-SL boundary conditions ($h/R = 0.002, L/R = 20$)

n	m	$P = 700 \text{ kPa}, a/L = 0.5$			
		$N = 0.5$	$N = 5$	$N = 15$	$N = 30$
1	1	342.546	334.567	332.903	331.509
2	1	429.875	419.132	417.519	416.220
3	1	456.345	445.094	442.763	442.729
4	1	473.980	461.342	458.093	458.228
5	1	487.124	475.228	473.773	472.541
6	1	502.569	490.632	488.387	487.118
7	1	519.320	506.096	504.531	503.539
8	1	537.671	524.667	521.335	521.447
9	1	556.905	543.491	541.822	540.731
10	1	577.428	564.611	561.747	561.983

Table 5 Variation of the natural frequency (Hz) with the different power-law exponent for F-SS boundary conditions ($h/R = 0.002, L/R = 20$)

n	m	$P = 700 \text{ kPa}, a/L = 0.5$			
		$N = 0.5$	$N = 5$	$N = 15$	$N = 30$
1	1	480.679	469.240	466.942	466.670
2	1	800.226	780.754	777.405	775.051
3	1	810.076	791.744	787.116	785.565
4	1	817.676	797.311	793.242	792.111
5	1	826.913	806.962	800.899	800.533
6	1	833.346	812.670	808.920	807.872
7	1	842.118	822.749	818.442	817.276
8	1	853.842	833.286	829.091	827.878
9	1	866.894	845.462	841.295	838.369
10	1	879.643	858.961	854.581	853.665

9 Conclusions


This study presents the influence of power-law distribution with pressure on frequencies of the supported functionally graded cylindrical shell. The governing equations of the movement were utilized by the Ritz method. The boundary conditions are clamp-

sliding and free- simply support. Natural frequencies with different amounts of the power-law with pressure for different boundary conditions are affected by the variation of the circumferential wave number. This study shows that the frequencies decreased with the increase in the amounts of the power-law distribution

with pressure. Thus the constituent power-law distribution with pressure effects on the frequencies. The results show the frequencies with different power-law distribution under pressures are various for different conditions.

References

- [1] Sechler, E.E., 1974. Thin-shell structures theory experiment and design. Englewood Cliffs, NJ: Prentice-Hall, California.
- [2] Yan, J., Li, T.Y., Liu, T.G. & Liu, J.X. 2006. Characteristics of the vibrational power flow propagation in a submerged periodic ring-stiffened cylindrical shell. *Applied Acoustics*. (67): 550-569.
- [3] Wang, R.T. & Lin, Z.X. 2006. Vibration analysis of ring-stiffened cross-ply laminated cylindrical shells. *Journal of Sound and Vibration*. (295): 964-987.
- [4] Pan, Z., Li, X. & Ma, J. A. 2008. Study on free vibration of a ring-stiffened thin circular cylindrical shell with arbitrary boundary conditions. *Journal of Sound and Vibration*. (314): 330-342.
- [5] Gan, L., Li, X. & Zhang, Z. 2009. Free vibration analysis of ring-stiffened cylindrical shells using wave propagation approach. *Journal of Sound and Vibration*. (326): 633-646.
- [6] Zhou, X. 2012. Vibration and stability of ring-stiffened thin-walled cylindrical shells conveying fluid. *Acta Mechanica Sinica*. (25): 168-176.
- [7] Qu, Y., Chen, Y., Long, X., Hua, H. & Meng, G. 2013. A modified variational approach for vibration analysis of ring-stiffened conical-cylindrical shell combinations. *European Journal of Mechanics endash; A/Solids*. (37): 200-215.
- [8] Love, A.E.H. 1944. A treatise on the mathematical theory of elasticity [M]. New York: Dover Publication.
- [9] Leissa, A.W. 1993. Vibration of shells. NASA SP-288, 1973; Reprinted by Acoustical Society of America, America Institute of Physics.
- [10] Blevins, R.D. 1979. Formulas for natural frequency and mode shape. Van Nostrand Reinhold, New York.
- [11] Soedel, W. 1980. A new frequency formula for closed circular cylindrical shells for a large variety of boundary conditions. *Journal of Sound and Vibration*. (70): 309-317.
- [12] Chung, H. 1981. Free vibration analysis of circular cylindrical shells. *Journal of Sound and Vibration*. (74): 331-359.
- [13] Reddy, J.N. 2004. Mechanics of laminated composite plates and shells. 2nd edn. CRC Press, New York.
- [14] Forsberg, K. 1964. Influence of boundary conditions on modal characteristics of cylindrical shells. *AIAA Journal*. (2): 182-189.
- [15] Miyamoto, Y., Kaysser, W.A., Rabin, B.H., Kawasaki, A. & Ford, R.G. 1999. Functionally graded materials: design, processing and applications, Kluwer Academic Publishers, London.
- [16] Loy, C.T., Lam, K.Y. & Reddy, J.N. 1999. Vibration of functionally graded cylindrical shells. *International Journal of Mechanical Sciences*. (41): 309-324.
- [17] Patel, B.P., Gupta, S.S., Loknath, M.S. & Kadu, C.P. 2005. Free vibration analysis of functionally graded elliptical cylindrical shells using higher order theory. *Composite Structures*. (69): 259-270.
- [18] Zhi, C. & Hua, W. 2007. Free vibration of FGM cylindrical shells with holes under various boundary conditions. *Journal of Sound and Vibration*. (306): 227-237.
- [19] Arshad, S. H., Naeem, M. N., & Sultana, N. 2007. Frequency analysis of functionally graded material cylindrical shells with various volume fraction laws. *Proceedings of the Institution of Mechanical Engineers, Part C: Journal of Mechanical Engineering Science*. (221): 1483-1495.
- [20] Shah, A.G., Mahmood, T. & Naeem, M.N. 2009. Vibrations of FGM thin cylindrical shells with exponential volume fraction law. *Applied Mathematics and Mechanics (English Edition)*. (5): 607-615.
- [21] Hosseini-Hashemi, sh., Ilkhani, M.R and Fadaee, M. Accurate natural frequencies and critical speeds of a rotating functionally graded moderately thick cylindrical shell. *International Journal of Mechanical Sciences* 76 (2013) 9-20.
- [22] Amirabadi, H., Farhatnia, F., Eftekhari, S.A., Hosseini-Ara, R. 2020. Free vibration analysis of rotating functionally graded GPL-reinforced truncated thick conical shells under different boundary conditions. *Mechanics Based Design of Structures and Machines*, Published online: 30 Sep 2020. pp. 1-32.
- [23] Mohamadi, B., Eftekhari, S.A., Toghraie, D. 2020. Numerical investigation of nonlinear vibration analysis for triple-walled carbon nanotubes conveying viscous fluid. *International Journal of Numerical Methods for Heat & Fluid Flow*, Vol. 30 No. 4, pp. 1689-1723.
- [24] Amirabadi, H., Farhatnia, F., Eftekhari, S.A., Hosseini-Ara, R. 2021. Wave propagation in rotating functionally graded GPL-reinforced cylindrical shells based on the third-order shear deformation theory. *Waves in Random and Complex Media*, Published online: 03 Feb 2021.
- [25] Soedel, W. 2004. Vibration of shells and plates. 3rd edn. Marcel Dekker Inc, New York.
- [26] Reddy, J.N. 2004. Mechanics of laminated composite plates and shells: Theory and analysis, 2nd ed. CRC Press, Boca Raton.

 **DOR: 20.1001.1.2322388.2021.9.1.5.1**

Research Paper

Nanoporous Carbon Spheres Derived from the Leather Leaf as Electrode Materials for Supercapacitors

Azam Asadi¹, Hamid Oveisi^{*1, 2}

1. Department of Materials and Polymer Engineering, Hakim Sabzevari University, Sabzevar 9617976487, Iran

2. Nanotechnology Research Center, Hakim Sabzevari University, Sabzevar 9617976487, Iran

ARTICLE INFO

Article history:

Received 2 August 2020

Accepted 2 October 2020

Available online 1 January 2021

Keywords:

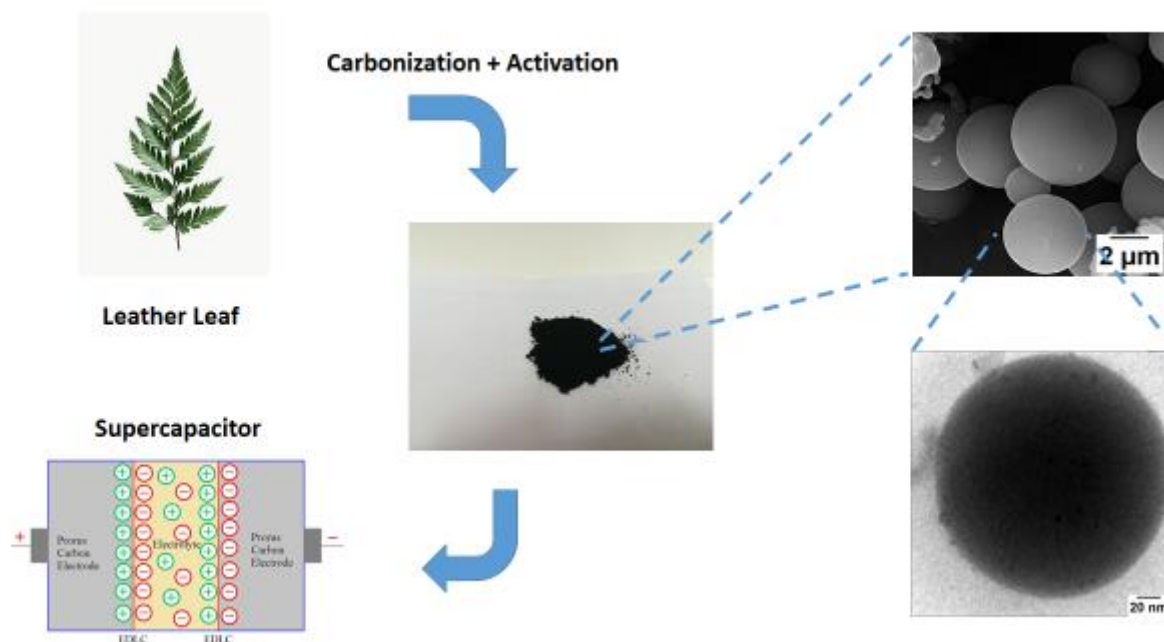
*Nanoporous Carbon**Biomass**Leather Leaf**Spherical Morphology**Supercapacitor*

ABSTRACT

In this study, nanostructured carbon spheres were fabricated from leather leaf via hydrothermal carbonization and chemically activated with KOH. Different hydrothermal carbonization temperatures were used. The microtopographic, compositional, and structural characteristics and the surface properties of the synthesized material were then investigated via scanning electron microscopy, transmission electron microscopy, X-ray diffraction, nitrogen adsorption-desorption, and Raman spectroscopy. Results indicated that the KOH-activated sample synthesized with hydrothermal procedure leads to spheroidal nano-porous amorphous carbon particles with an average size of 3-5 micrometers. The nano-porous carbon spheres exhibited remarkable material properties such as high specific surface area ($1342 \text{ m}^2 \text{ g}^{-1}$) and a well-developed porosity with a distribution of micropores 2 nm wide. These properties led to good electrochemical performance as supercapacitor electrodes. The electrochemical investigations through a three-electrode cell in an aqueous electrolyte have also confirmed the capability of the synthesized activated carbon nano-particles as promising candidates for supercapacitor applications. In particular, a specific capacitance of 374 F g^{-1} was achieved at a current density of 2 A g^{-1} .

* Corresponding Author:

E-mail: hamid.oveisi@hsu.ac.ir



Graphical abstract of hydrothermal carbonization of nanoporous carbon spheres derived from the leather leaf

1- Introduction

The development of green, renewable, and highly efficient methods of energy conversion, as well as new energy storage technologies, is in high demand [1-3]. As an energy storage device, supercapacitors are an effective and practical technology for electrochemical energy conversion and storage. Supercapacitors, also known as EDLC (electric double-layer capacitors) or Ultracapacitors, can store tremendous amounts of energy. Operating based on their electrochemical properties, supercapacitors have found incredible recognition for novel applications. Their outstanding electrochemical performance, including optimal reversibility, power capability, and cycle life, makes them great options in different areas, such as intelligent automobiles, portable power tools, and uninterrupted power sources [4].

Fabricating supercapacitors requires cost-effective production materials. Carbonaceous materials, which are popular base materials for electrodes, are an incredible option since they provide an easy fabrication process, potentially significant specific capacitance, and considerable mechanical flexibility [5]. Among various carbonaceous materials, nanoporous carbon spheres have gained considerable attention due to their optimal electrical conductivity and the ability to minimize viscous effects and finely tune the porosity [6-8]. The discovery of fullerenes, carbon nanotubes, nano-porous carbon, and graphene, with optimal nanostructures and

functionalization patterns, has made the areas related to advanced carbon materials mainly thriving. However, these carbon nanomaterials strongly depend on precursors based on fossil fuels, such as CH_4 , phenol, and pitch, and extreme synthetic conditions requiring massive energy levels. These methods and techniques are not optimally cost-effective and can damage the environment because they use unsafe toxic compounds that are environmentally unfriendly. Hence, the development of nanoporous carbon derived from renewable biomass is of growing importance for creating sustainable energy-storage systems [9-14].

Hence, various synthetic strategies, including hydrothermal carbonization [15], nanocasting technique [16], and emulsion polymerization method [17], have been developed for the preparation of carbon spheres. In addition to the kinds of synthetic methods, carbon materials also can be fabricated by hydrothermal carbonization [18-21] for creating nanoporous carbon spheres.

In this work, we demonstrate a simple hydrothermal assisting pyrolysis method by using a green, renewable, cost-effective, and widespread plant as the precursors and explored as an electrode for supercapacitors. Due to its special characteristics, such as emulsifying, gelling, and stabilizing abilities, the leather leaf has been extensively used in medical and ornamental usage. However, to the best of our knowledge, this natural material has not been used as a source of carbon materials for energy applications.

Many electrode types have been tested, and the most frequent systems today are synthesized on the electrochemical double-layer capacitor based on carbon and an organic electrolyte and convenient operability [22]. Yin et al. used KOH as an activator agent and coconut fibers to produce activated carbon to produce a supercapacitor electrode, which displayed a particular capacitance of 266 F/g at a current of 0.1 A/g. Many studies highlight the potential of crops and agricultural residues as a significant carbon source. Izan Izwan Misnon et al. used oil palm kernel shells to synthesize supercapacitors with outstanding performance. In comparison, those samples that were chemically activated represented a particular capacitance of 210 F/g at 0.5 A/g, while the same quality in physically activated samples was 50% lower [23].

2- Experimental

2-1- Synthesis

The raw material (leather leaf) was initially dried, and then the powder (3 g) was dissolved in water (50 mL) under stirring. The resulting solution was sealed into a Teflon-lined autoclave of 150 mL capacity, and maintained for 12 h and three different temperatures (100, 150, and 200 °C) were applied in the hydrothermal carbonization stage, ensuring the complete progression of the reaction. After the autoclave was cooled to room temperature, the obtained hydrothermal carbon as dark precipitate was collected by centrifugation, washed with water and ethanol several times, and dried at 70 °C for 8 h. The obtained hydrothermal carbon was mixed with the selected activation agents of KOH with the powder/KOH weight ratio of 1:2. The mixture was heated up to 900 °C temperature in a tube furnace under N₂ atmosphere for 2 h, with a temperature ramp of 5 °C min⁻¹. The obtained activated carbon was washed with 2 M hydrochloric acid and water to remove potassium species thoroughly and finally dried at room temperature.

2-2- Characterization

The phase analysis of the samples was carried out via a Top metrology-GNR Explorer X-ray diffractometer (XRD, $\lambda=0.154$ nm, continuous scanning mode (0.02°/min)). Raman spectroscopy was also performed using a Raman Microscope (Teksan Co.) at room temperature in the wavelength range 45 to

4700 cm⁻¹ on the Hamamatsu detection system and with the signal-to-noise ratio of 300:1 (estimated spectral resolution of 6 cm⁻¹). The sample excitement was aided by an Nd:YAG laser (785 nm with DPSS 785nm Laser, exposure time of 16s). The nitrogen adsorption-desorption method was applied in the mesostructural parameters investigations in which the samples were initially degassed at 353 K for 24 h. The Bruaauer–Emmett–Teller (BET) technique and Barrett–Joyner–Halenda (BJH) model were used in the measurements of specific surface area and pore diameters of the nano-carbon particles, respectively. The microstructural characterizations were carried out using a field-emission scanning electron microscope (FE-SEM, TESCAN Mira 3-XMU) and a transmission electron microscope (TEM, Philips CM120, operation voltage of 100 kV).

A ZIVE-SP1 potentiostat-galvanostat (Wonatech-Korea) was used in the electrochemical analysis of the samples. The test setup was designed as a three-electrode system, including a platinum wire as a counter electrode, saturated calomel as the reference electrode, and samples as the working electrodes. The working electrodes were prepared using a mixture of the synthesized carbon particles and silver paste, coated on cleaned FTO glass (1×1 cm²) sheets. An aqueous solution of 0.5 M Na₂SO₄ was also applied as the electrolyte.

The cyclic voltammetry (CV) vs. SCE curves were then captured in the potential range of -0.2 to 0.5 V through the varying scan rates of 10 to 100 mV s⁻¹. The galvanostatic charge-discharge measurements were then carried out at 2-10 A g⁻¹ over a voltage range of -0.2 to 0.5 V vs. SCE. The electrochemical impedance spectroscopy (EIS) measurements were also performed in the frequency range of 10⁻² to 10⁵ Hz at an open-circuit voltage (the amplitude of 0 V).

3- Results and discussion

The obtained hydrothermal carbon at three different temperatures (100, 150, and 200 °C) are shown in Fig. 1. These powders were collected by centrifugation after the autoclave was cooled to room temperature. It can be observed that the best temperature is 200 °C because the product color was not black in two other temperatures, indicating the carbon was not formed completely.



Fig. 1. Obtained hydrothermal carbon derived from the leather leaf at three different temperatures; a) 100, b) 150, and c) 200 °C

The XRD pattern of nano-porous carbon spheres shown in Fig. 2 indicates two broad peaks around 23° and 43°. The peaks are respectively attributed to the (002) and (100) planes of the graphite-like carbon.

However, based on the broadness of the peaks, the activated nano-porous carbon can be considered semi-crystalline materials.

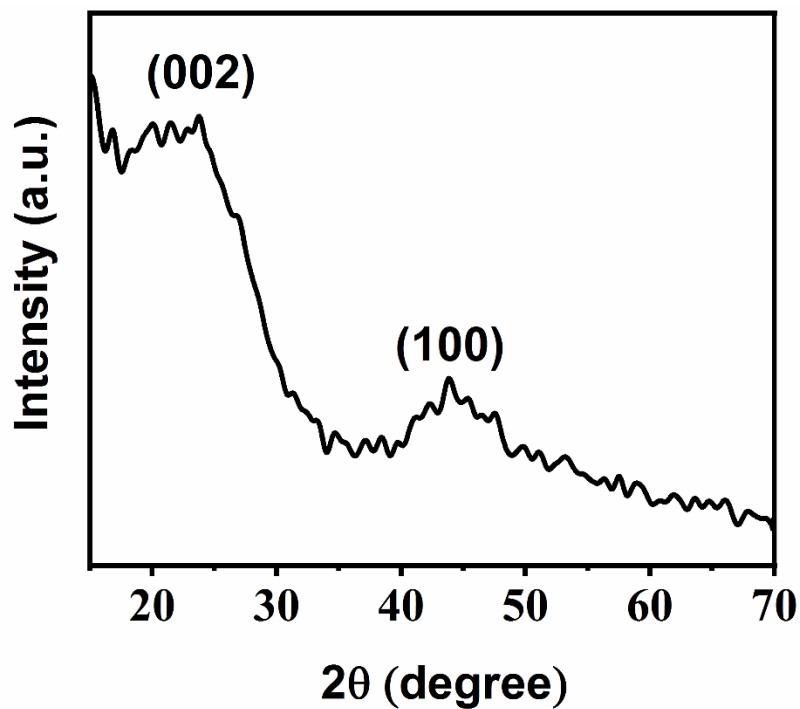


Fig. 2. X-ray diffraction (XRD) patterns of nanoporous carbon spheres derived from leather leaf

While the presence of graphitic structure in the obtained carbon particles cannot be well-indicated by the XRD, any ordered/disordered structure of the graphite flakes, known as a witness of graphene formation, can be detected via Raman spectroscopy. The typical Raman spectra of the activated nanoporous carbon particles are presented in Fig. 3. As can be seen, two peaks can be observed at 1320 and 1585 cm^{-1} , which are assigned to the characteristic D

(defects and disorder) and G (graphitic) bands of carbon, respectively [24]. The G/D ratio of band intensities can be considered as an indicator of disordering and/or defects in the graphitic structure [25]. The G/D intensity ratio of carbon spheres was determined to be about 1.04. This result indicates that the porous carbons were relatively graphitized at low temperatures.

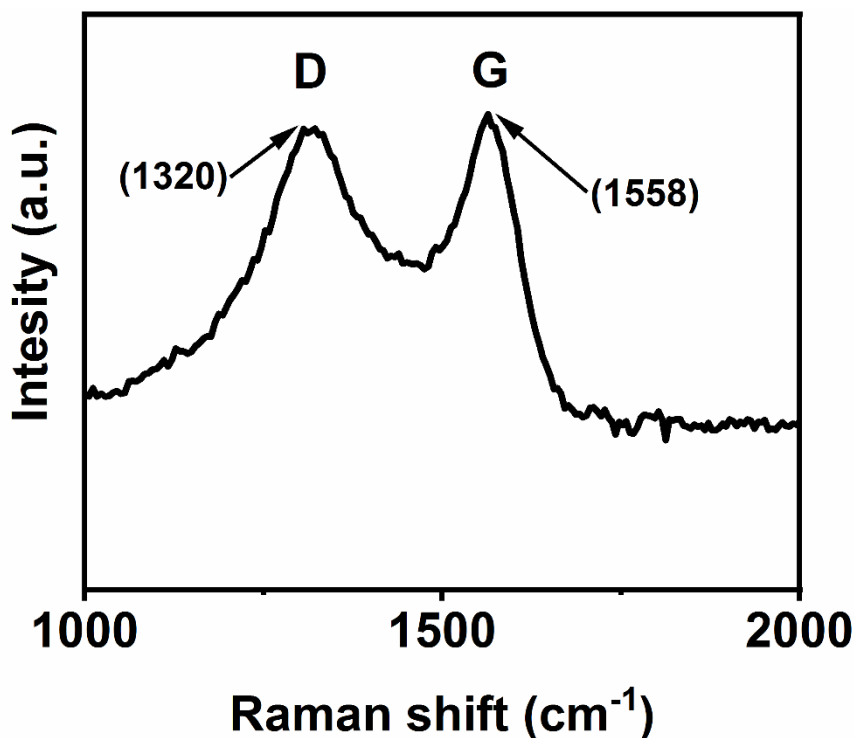


Fig. 3. Typical Raman spectra of the activated carbon particles obtained by hydrothermal carbonization

As shown in Fig. 4, the hydrothermal carbonization of leather leaf resulted in 2-5 μm diameter spherical carbon particles. This kind of spherical micro-sized particles was commonly observed for the hydrothermal carbons derived from mono- and polysaccharides (e.g., sucrose, glucose, starch, and cellulose) [26-29]. Upon KOH activation, the

spherical morphology was still maintained in activated carbon, as evidenced by the SEM and the TEM images (Fig. 4 and 5). Fig. 5 shows the TEM image of the synthesized porous spheres with nanopores. These results reveal good stability of nanoporous carbon spheres, which are without any collapse during the high-temperature carbonization.

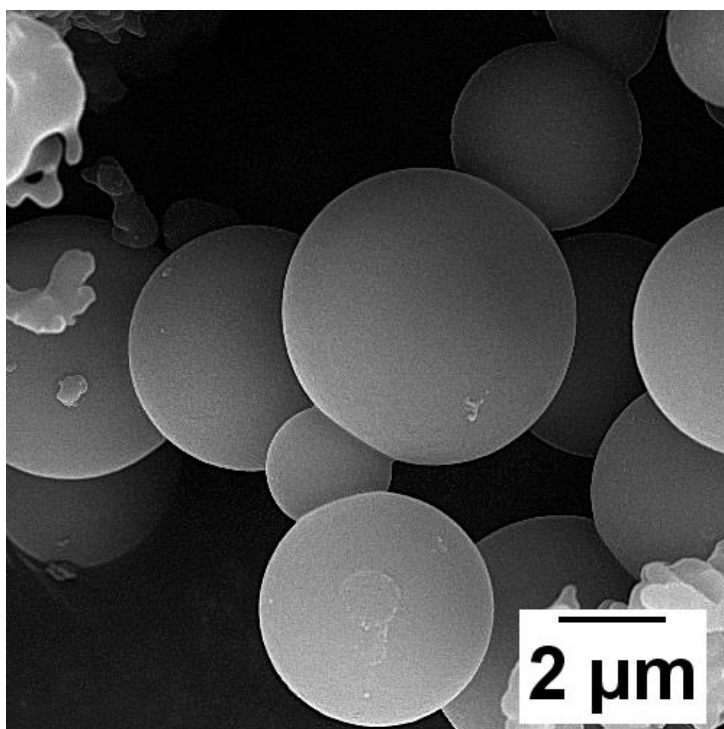


Fig. 4. FE-SEM images of nanoporous carbon spheres derived from leather leaf with spherical morphology

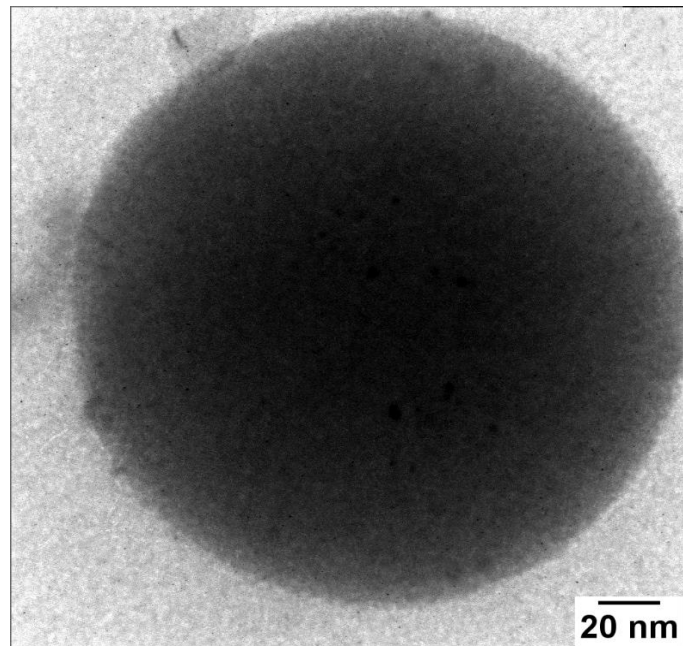


Fig. 5. TEM image of a single particle of nanoporous carbon

To further investigate the porosity, the surface area of the obtained nano-porous carbon particles was quantitatively measured through the Brunauer–Emmett–Teller (BET) method. Nitrogen adsorption-desorption isotherms of carbons are shown in Fig. 6. As can be seen, the adsorption isotherms are strongly dependent on the preparation conditions, which address the significance of the chemical activation process in controlling the surface area of the synthesized materials. The clear nitrogen uptakes, observed at low relative pressures ($P/P_0 < 0.1$), address the reversible type I isotherm that is commonly

observed in microporous solids with relatively small external surfaces. Such limited uptake behavior is mainly derived by the volume of the accessible micro-pores rather than the internal surface area. Moreover, a slight increase in nitrogen uptake is observed at higher relative pressures. A small hysteresis loop was also observed at a higher relative pressure region. These situations have been often seen in nano-porous materials with randomly arranged pores having various sizes. The BET-specific surface area of nano-porous carbon spheres is calculated to be $1342 \text{ m}^2\text{g}^{-1}$.

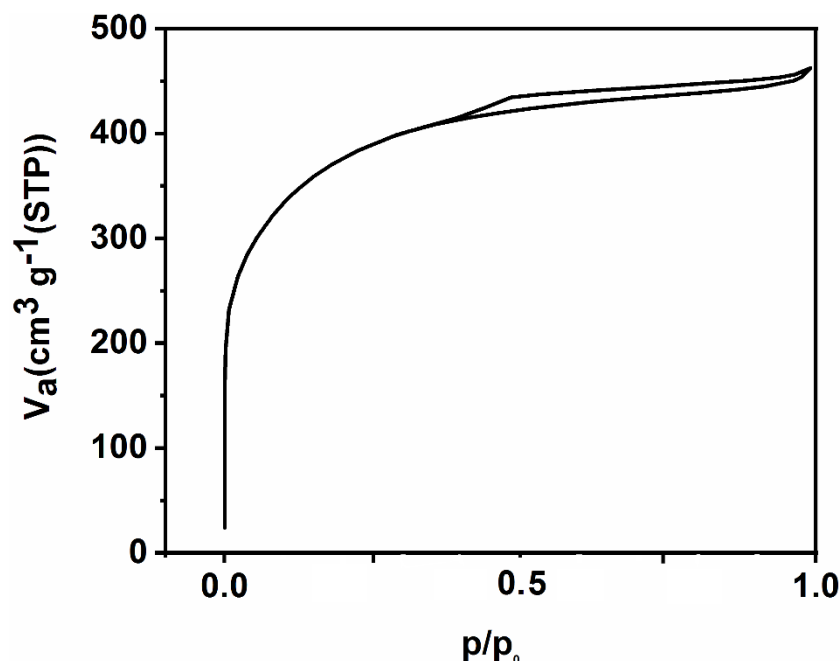


Fig. 6. Nitrogen adsorption and desorption isotherms measured at 77 K for the nanoporous carbon spheres

The pore size distribution (PSD) plot calculated by the Barrett-Joyner-Halenda (BJH) method is presented in Fig. 7. It resembles materials with narrow pore size distributions, a high ratio of micro-

pores, and near mono-modal PSD curves with average diameters of 2 nm. Accordingly, smaller pores (1 ~ 2 nm) are detected in the carbon nanospheres obtained from the KOH-activated samples.

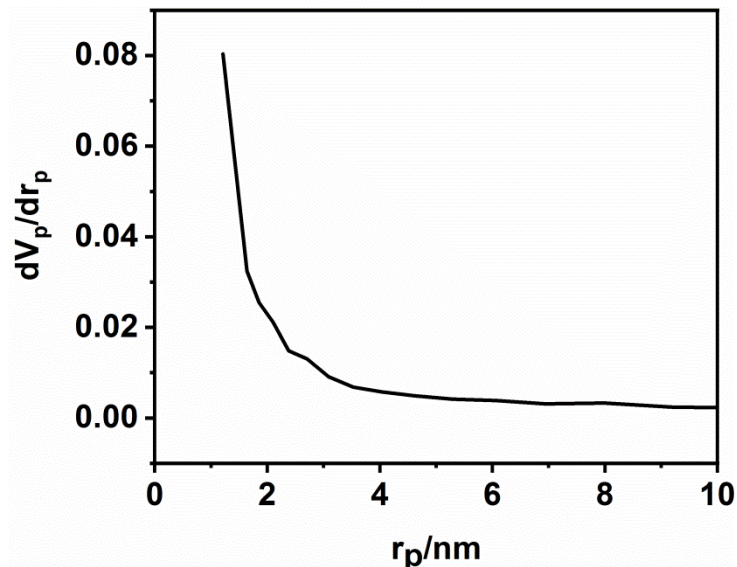


Fig. 7. Barrett-Joyner-Halenda (BJH) pore size distributions isotherm of nanoporous carbon spheres

The electrochemical capacitive properties of leather leaf-derived carbon materials were measured in 0.5 M Na₂SO₄ electrolyte using a three-electrode system. Fig. 8 depicts the CV curves of the carbon at the scan rate ranging from 10 to 100 mV s⁻¹. The relatively rectangular-shaped CV curves of all the activated

carbons resemble the typical characteristic of double-layer capacitance. Moreover, as shown in Fig. 8, the porous carbon still presents a relatively rectangular CV shape at a high scan rate of 100 mV s⁻¹, which confirms the efficient charge transfer and electrolyte diffusion within the nanoporous carbon spheres [30].

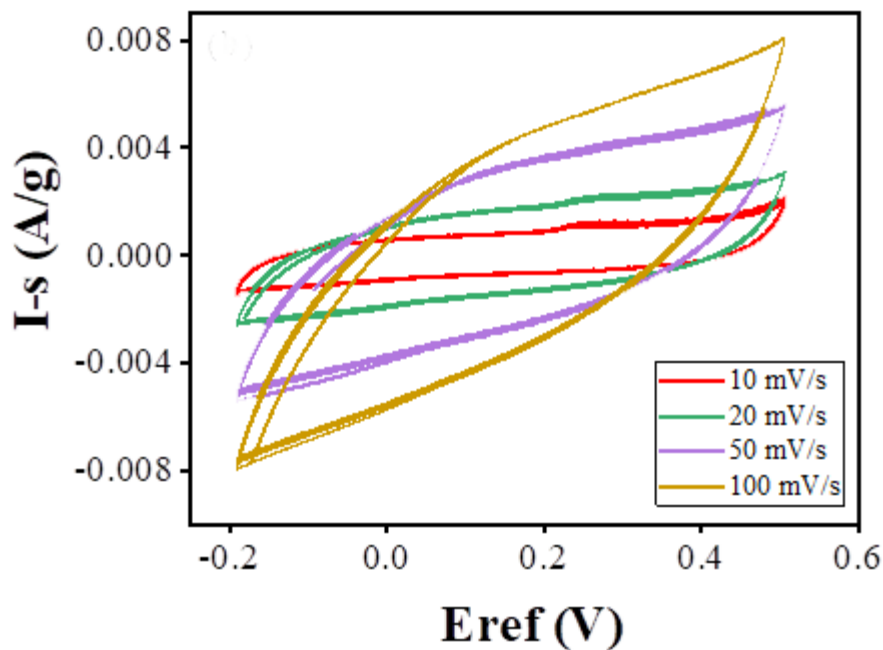


Fig. 8. Cyclic voltammetry (CV) curves of carbon spheres at various scan rate ranging from 10 to 100 mV s⁻¹

The galvanostatic charge-discharge curves of the carbons at a current density of 2 A g^{-1} are shown in Fig. 9. The relatively triangular shape curves indicate good reversibility of the carbon materials. The specific capacitance was calculated according to the

following equation: $C = i\Delta t / m\Delta V$, where i is discharge current (A), Δt is discharge time (s), and ΔV is a potential window (V) [31, 32]. The obtained specific capacitances value is 374 F g^{-1} .

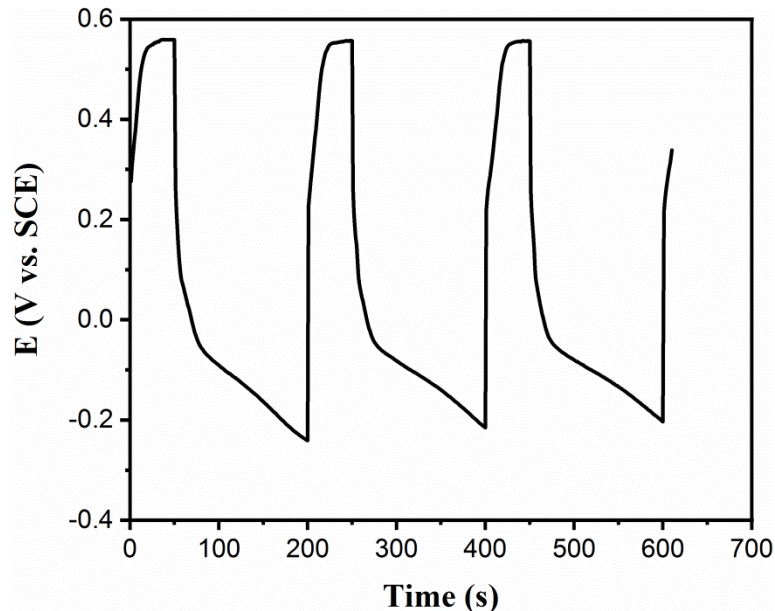


Fig. 9. Galvanostatic charge-discharge curves (chronopotentiometry) of the nanoporous carbons

Fig. 10 shows the Nyquist plots of carbons in the frequency range of 10^{-2} to 10^5 Hz under open circuit potential. As can be seen, the nanoporous carbon particles show good capacitive behavior, including a vertical slope at the low-frequency region. At higher frequencies, the intercept of the plot with the real axis represents the equivalent series resistance (ESR) R_s , which is occurred due to the combination of the effects of ionic resistance of the electrolyte, intrinsic resistance of the active materials, and contact

resistance with the current collector [33]. At medium frequencies, Nyquist plots exhibit a Warburg-type line with a slope of about 45° . Projecting the length of the Warburg line on the real axis can result in increased diffusion of ions at the electrode-electrolyte interface [34]. As shown in Fig. 9, the carbon spheres demonstrate the short Warburg-type line, indicating superior ion diffusion in the mesoporous structure of carbon spheres.

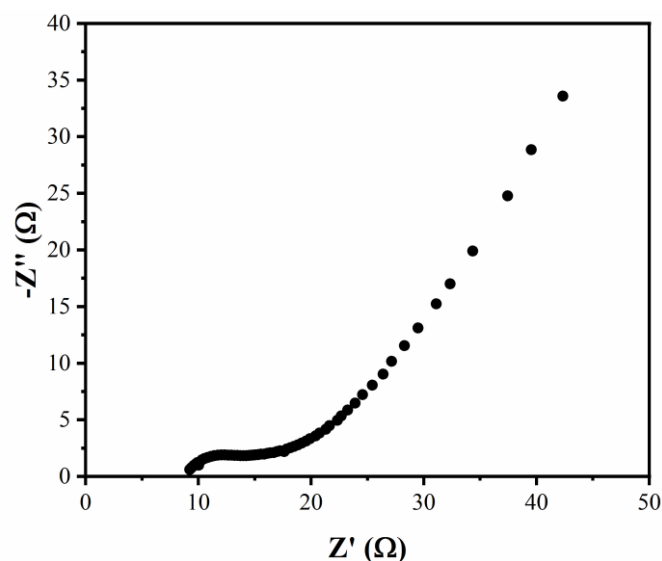


Fig. 10. Electrochemical impedance spectra (EIS) or Nyquist plot of the activated carbons

4. Conclusion

Nano-porous carbon spheres have been successfully synthesized via a template-free hydrothermal assisting pyrolysis method using the leather leaf as a low-cost precursor material. Results showed that the best temperature for the hydrothermal stage is 200 °C. Compared with the products obtained by single hydrothermal treatment or annealing treatment, the carbon spheres have the largest specific surface area, exhibit suitable electric double-layer capacitance. The results of porosimetry through the N₂ adsorption-desorption method indicated the highest surface area of 1342 m²g⁻¹.

The rectangular shape of the CV curves in this study showed the typical characteristics of double-layer capacitance. Notably, the synthesized carbon particles derived by the KOH activation agents presented a high capacitance of 374 F g⁻¹. The superior capacitive properties of carbon spheres are closely related to their high surface area, optimized microporous structure, and narrow pore size distribution. This work demonstrates that the textural properties of carbon materials derived from biomass can be finely modulated by KOH activation. The leather-leaf derived carbon sphere materials have promising potential in the application of energy storage devices.

References

- [1] Y. Yang, M. Luo, W. Zhang, Y. Sun, X. Chen, S. Guo, "Metal surface and interface energy electrocatalysis: Fundamentals, performance engineering, and opportunities", *Chem*, Vol. 4, No. 9, 2018, pp. 2054-2083.
- [2] S. Zhang, Q. Fan, R. Xia, T.J. Meyer, "Co2 reduction: From homogeneous to heterogeneous electrocatalysis", *Accounts of Chemical Research*, Vol. 53, No. 1, 2020, pp. 255-264.
- [3] C. Touriño, F. Oveisi, J. Lockney, D. Piomelli, R. Maldonado, "Faah deficiency promotes energy storage and enhances the motivation for food", *Int J Obes (Lond)*, Vol. 34, No. 3, 2010, pp. 557-68.
- [4] Y.S. Yun, M.H. Park, S.J. Hong, M.E. Lee, Y.W. Park, H.J. Jin, "Hierarchically porous carbon nanosheets from waste coffee grounds for supercapacitors", *ACS Appl Mater Interfaces*, Vol. 7, No. 6, 2015, pp. 3684-90.
- [5] R. Srinivasan, E. Elaiyappillai, H.P. Pandian, R. Vengudusamy, P.M. Johnson, S.-M. Chen, R. Karvembu, "Sustainable porous activated carbon from polyalthia longifolia seeds as electrode material for supercapacitor application", *Journal of Electroanalytical Chemistry*, Vol. 849, No. 2019, pp. 113382.
- [6] J.P. Paraknowitsch, Y. Zhang, B. Wienert, A. Thomas, "Nitrogen- and phosphorus-co-doped carbons with tunable enhanced surface areas promoted by the doping additives", *Chemical Communications*, Vol. 49, No. 12, 2013, pp. 1208-1210.
- [7] H. Zhang, J. Chen, Y. Li, P. Liu, Y. Wang, T. An, H. Zhao, "Nitrogen-doped carbon nanodots@nanospheres as an efficient electrocatalyst for oxygen reduction reaction", *Electrochimica Acta*, Vol. 165, No. 2015, pp. 7-13.
- [8] S. Chao, Q. Cui, K. Wang, Z. Bai, L. Yang, J. Qiao, "Template-free synthesis of hierarchical yolk-shell co and n codoped porous carbon microspheres with enhanced performance for oxygen reduction reaction", *Journal of Power Sources*, Vol. 288, No. 2015, pp. 128-135.
- [9] M. Li, H. Xiao, T. Zhang, Q. Li, Y. Zhao, "Activated carbon fiber derived from sisal with large specific surface area for high-performance supercapacitors", *ACS Sustainable Chemistry & Engineering*, Vol. 7, No. 5, 2019, pp. 4716-4723.
- [10] R. Wang, P. Wang, X. Yan, J. Lang, C. Peng, Q. Xue, "Promising porous carbon derived from celtuce leaves with outstanding supercapacitance and CO₂ capture performance", *ACS Appl Mater Interfaces*, Vol. 4, No. 11, 2012, pp. 5800-6.
- [11] S. Yaglikci, Y. Gokce, E. Yagmur, Z. Aktas, "The performance of sulphur doped activated carbon supercapacitors prepared from waste tea", *Environmental Technology*, Vol. 41, No. 1, 2020, pp. 36-48.
- [12] B. Zhu, C. Shang, Z. Guo, "Naturally nitrogen and calcium-doped nanoporous carbon from pine cone with superior CO₂ capture capacities", *ACS Sustainable Chemistry & Engineering*, Vol. 4, No. 3, 2016, pp. 1050-1057.
- [13] J. Tang, J. Liu, N.L. Torad, T. Kimura, Y. Yamauchi, "Tailored design of functional nanoporous carbon materials toward fuel cell applications", *Nano Today*, Vol. 9, No. 3, 2014, pp. 305-323.
- [14] P. Liu, Y. Wang, J. Liu, "Biomass-derived porous carbon materials for advanced lithium sulfur batteries", *Journal of Energy Chemistry*, Vol. 34, No. 2019, pp. 171-185.
- [15] S. Gao, Y. Chen, H. Fan, X. Wei, C. Hu, H. Luo, L. Qu, "Large scale production of biomass-derived n-doped porous carbon spheres for oxygen reduction and supercapacitors", *Journal of Materials Chemistry A*, Vol. 2, No. 10, 2014, pp. 3317-3324.
- [16] R. Liu, D. Wu, X. Feng, K. Müllen, "Nitrogen-doped ordered mesoporous graphitic arrays with high electrocatalytic activity for oxygen reduction", *Angew Chem Int Ed Engl*, Vol. 49, No. 14, 2010, pp.

2565-9.

[17] P.A. Lovell, F.J. Schork, "Fundamentals of emulsion polymerization", *Biomacromolecules*, Vol. 21, No. 11, 2020, pp. 4396-4441.

[18] D. Kim, K. Lee, K. Park, "Upgrading the characteristics of biochar from cellulose, lignin, and xylan for solid biofuel production from biomass by hydrothermal carbonization", *Journal of Industrial and Engineering Chemistry*, Vol. 42, No. 2016, pp. 95-100.

[19] A.Y. Krylova, V.M. Zaitchenko, "Hydrothermal carbonization of biomass: A review", *Solid Fuel Chemistry*, Vol. 52, No. 2, 2018, pp. 91-103.

[20] X. Xu, E. Jiang, "Treatment of urban sludge by hydrothermal carbonization", *Bioresour Technol*, Vol. 238, No. 2017, pp. 182-187.

[21] S. Nizamuddin, H.A. Baloch, G.J. Griffin, N.M. Mubarak, A.W. Bhutto, R. Abro, S.A. Mazari, B.S. Ali, "An overview of effect of process parameters on hydrothermal carbonization of biomass", *Renewable and Sustainable Energy Reviews*, Vol. 73, No. 2017, pp. 1289-1299.

[22] K. Mensah-Darkwa, C. Zequine, P.K. Kahol, R.K. Gupta, "Supercapacitor energy storage device using biowastes: A sustainable approach to green energy", *Sustainability*, Vol. 11, No. 2, 2019, pp. 414.

[23] L. Yin, Y. Chen, D. Li, X. Zhao, B. Hou, B. Cao, "3-dimensional hierarchical porous activated carbon derived from coconut fibers with high-rate performance for symmetric supercapacitors", *Materials & Design*, Vol. 111, No. 2016, pp. 44-50.

[24] I.I. Misnon, N.K.M. Zain, R.A. Aziz, B. Vidyadharan, R. Jose, "Electrochemical properties of carbon from oil palm kernel shell for high performance supercapacitors", *Electrochimica Acta*, Vol. 174, No. 2015, pp. 78-86.

[25] Y. Fan, X. Yang, B. Zhu, P.-F. Liu, H.-T. Lu, "Micro-mesoporous carbon spheres derived from carrageenan as electrode material for supercapacitors", *Journal of Power Sources*, Vol. 268, No. 2014, pp. 584-590.

[26] A.C. Ferrari, J. Robertson, "Interpretation of raman spectra of disordered and amorphous carbon", *Physical Review B*, Vol. 61, No. 20, 2000, pp. 14095-14107.

[27] C.A. Nieves, L.M. Martinez, A. Meléndez, M. Ortiz, I. Ramos, N.J. Pinto, N. Zimbovskaya, "Temperature-dependent charge transport mechanisms in carbon sphere/polyaniline composite", *AIP Advances*, Vol. 7, No. 12, 2017, pp. 125229.

[28] G. Wen, B. Wang, C. Wang, J. Wang, Z. Tian, R. Schlögl, D.S. Su, "Hydrothermal carbon enriched with oxygenated groups from biomass glucose as an efficient carbocatalyst", *Angewandte Chemie*

International Edition, Vol. 56, No. 2, 2017, pp. 600-604.

[29] J. Serrano, P. Pico, M. Amín, A. Pinilla, D. Torrado, C. Murillo, N. Bardin-Monnier, N. Ratkovich, F. Muñoz, O. Dufaud, "Experimental and cfd-dem study of the dispersion and combustion of wheat starch and carbon-black particles during the standard 20l sphere test", *Journal of Loss Prevention in the Process Industries*, Vol. 63, No. 2020, pp. 103995.


[30] S. Yu, W. Li, Y. Fujii, T. Omura, H. Minami, "Fluorescent spherical sponge cellulose sensors for highly selective and semiquantitative visual analysis: Detection of hg²⁺ and cu²⁺ ions", *ACS Sustainable Chemistry & Engineering*, Vol. 7, No. 23, 2019, pp. 19157-19166.

[31] H. Yang, "Graphene-based supercapacitors for energy storage applications", *Proc.* 2013, pp.

[32] X. Liu, M. Zheng, Y. Xiao, Y. Yang, L. Yang, Y. Liu, B. Lei, H. Dong, H. Zhang, H. Fu, "Microtube bundle carbon derived from paulownia sawdust for hybrid supercapacitor electrodes", *ACS Applied Materials & Interfaces*, Vol. 5, No. 11, 2013, pp. 4667-4677.

[33] I. Gaztelumendi, M. Chapartegui, R. Seddon, S. Flórez, F. Pons, J. Cinquin, "Enhancement of electrical conductivity of composite structures by integration of carbon nanotubes via bulk resin and/or buckypaper films", *Composites Part B: Engineering*, Vol. 122, No. 2017, pp. 31-40.

[34] L. Sun, C. Tian, M. Li, X. Meng, L. Wang, R. Wang, J. Yin, H. Fu, "From coconut shell to porous graphene-like nanosheets for high-power supercapacitors", *Journal of Materials Chemistry A*, Vol. 1, No. 21, 2013, pp. 6462-6470.

 **DOR: 20.1001.1.2322388.2021.9.1.6.2**

Research Paper

Effect of Tool Pin Shape on Defect-Free FSP and Particles Distribution in SiC/Al6061 Composites

Mortza Ezzati¹, Parviz Asadi^{*2}, Mostafa Akbari³

1. Student, Department of Mechanical Engineering, Faculty of Engineering, Imam Khomeini International University, Qazvin, Iran.

2. Assistant professor, Department of Mechanical Engineering, Faculty of Engineering, Imam Khomeini International University, Qazvin, Iran.

3. Assistant professor, Department of Mechanical Engineering, Technical and Vocational University (TVU), Tehran, Iran

ARTICLE INFO

Article history:

Received 23 July 2020

Accepted 11 August 2020

Available online 1 January 2021

Keywords:

*FSP**Pin Shape**Material flow**Defect formation**Reinforcing particles distribution*

ABSTRACT

In this research, Al-SiC composites were produced using FSP tools with different pin shapes to investigate the distribution of reinforcing particles in the base metal. First, to obtain the optimal rotational and traverse speed and tilt angle, several tests were performed on different parameters. The results showed that the rotational speed of 1250 rpm and the traverse speed of 100 mm/min in all tools produced flawless samples. Then, tools with different tool pin profiles of triflate, cylindrical, threaded, triangular, square, and hexagonal were utilized in this study. The distribution of reinforcing particles in the base metal was studied using a light microscope. The results showed that the cylindrical tool was not able to distribute particles in the base metal even after four passes of the process and was not a suitable tool for composite production. Tools with flat surfaces, such as square and triangular tools, have performed better in distributing reinforcing particles in the base metal. The results showed that the presence of a kind of eccentricity and pulse production in these tools had improved the distribution of particles. Threaded and hexagonal tools have the best performance in the distribution of reinforcing particles in the base metal and can be introduced as a suitable tool for composite products in the FSP process. The results of this study also showed that the change in the direction of tool rotation improved the distribution of reinforcing particles in all tools.

* Corresponding Author:

Emails Address: asadipar@gmail.com; parvizasadi@ut.ac.ir

1. Introduction

Aluminum and its alloys are widely used in the construction of aircraft, ships, and means of transport due to their special appeal in the production of lightweight products. 6061 aluminum alloy is used for structural applications due to its exceptional resistance to corrosion, machinability, and strength. When it comes to structural applications, 6061 aluminum alloy angle is one of the most commonly used shapes. However, these alloys are not strong enough for all engineering purposes, especially in applications where surface contact is present. For this reason, their use has been limited. To this end, several methods have been used by researchers to improve the performance of these alloys. Maurya et al. [1] fabricated composites with different weight percent of SiC content via the stir casting method, and their result showed that hardness and tensile strength were significantly improved up to 5 wt% of SiC particles. Chandla et al. [2] fabricate low-cost, lightweight metal matrix composite using Al 6061 as matrix material and alumina (Al_2O_3) and bagasse ash as reinforcing material through the stir casting process. They did not achieve a good distribution of reinforcing particles in the metal phase using this method, although the hardness of the composites relative to the base metal increased.

Friction stir processing was developed based on the principles of friction stir welding [3, 4]. Basically, the parameters and microstructural changes of these two processes are similar. However, the purpose of friction stir processing is not to join or weld two metal sheets but to modify the structure, change the grain size, increase the strength, make the structure uniform in terms of grain size, sediment distribution, and the creation of surface composites are the achievements of this process [5]. In friction stir processing, the rotating tool sinks into the integrated sheet to make local microstructural modification after processing to enhance the desired properties. Later, this process was used to produce surface layer composites, homogenize parts produced by powder metallurgy, modify the microstructure of metal-based composites, and improve the properties of cast alloys. Obtaining uniform distribution of reinforcing particles in the metal matrix is quite a challenging task. One of the significant problems in composite production is reinforcement particle agglomeration that worsens the composites' mechanical properties [6]. In FSP, the material flow pattern mainly depends on the tool pin profile so, the tool pin profile is the most influencing parameter on the distribution of reinforcing particles in the metal matrix. Various tool pin profiles like conical, triangular, threaded, square, cylindrical, etc., have been used in different

investigations. Elangovan et al. [7] investigated the effect of tool pin shape and tool shoulder diameter on the quality of aluminum stir zone. In their research, they used five tools (simple cylinder, threaded cylinders, conical, triangular, and square) and three different shoulder diameters (18, 15, and 21 mm). They reported that two pins with square and triangular geometry produce defect-free areas and have the highest hardness compared to other geometries among the five pins used. In this study, only the effect of tool pin shape on the microstructure enhancement, such as grain size in the SZ, has been investigated, and no reinforcing particles have been used. Khodaverdizadeh et al. [8] investigated the microstructural and mechanical properties of the joints produced between the copper sheets using different pins of the FSW tool. They concluded that using a square pin produced a joint with finer grains and thus improved mechanical properties. However, Faraji et al. [9] stated that the triangular tool creates more refined grains in the SZ than the square tool. Azizieh et al. [10] found that threaded tools are the most suitable tool for composite production. Zhao et al. [11] concluded that a threaded taper pin had the best material flow in comparing four pins of different shapes. Also, the sample produced with this pin had better strength and appearance than other pins such as threadless cylindrical, threaded cylindrical, and threadless taper. Another essential point in this study is the undeniable superiority of threaded tools over non-threaded tools. Also, the flow of materials in threadless pins (both conical and cylindrical) is not suitable, and the lack of materials in the processed area causes tunnel defects in the advancing side. Khojastehnezhad et al. [12] investigated of mechanical properties of friction stir processed Al 6061/ Al_2O_3 -Tib2 hybrid metal matrix composite. In this study, they examined the main welding parameters such as rotational speed and linear velocity and did not study the geometry of the tool. Material flow during FSP is the reason for distributing reinforcing particles in the metal matrix. As a result, the study of material flow patterns is crucial to understand the effect of tool pin profiles on particle distribution. However, it is challenging to use experimental methods to study the flow of matter during the process due to severe deformation as well as high temperatures. Therefore, numerical methods based on the FEM have been developed to model material flow. Akbari et al. [13] investigated the flow of material generated by the circular and threaded tool pin profiles during the fabrication of composite using FSP. Their material flow results clearly identified the reason for the proper distribution of ceramic particles when using the threaded tool.

Akbari et al. [5, 14] simulated material flow in dissimilar friction stir lap welding of brass and aluminum using coupled Eulerian and Lagrangian method. The material flow simulation results clearly showed how brass and aluminum are mixed in the stir zone. Akbari et al. [13] investigated the material flow of different locations in the stir zone (SZ), including the advancing side, the retreating side, the shoulder-affected area, and the pin-affected area 3D finite element method.

In this study, the different pin shapes used in several previous studies were collected, and the effect of these pins on the distribution of reinforcing particles in the base metal was systematically investigated. In previous research, as mentioned, one or more limited

pins were generally used to produce the composite, which did not allow for a comprehensive comparison between the performance of the different pins. For this purpose, by using different pins of the tool, the performance of each of them will be examined, and the appropriate pin shape will be introduced.

2. Experimental method

In order to produce the composite, 6061-O aluminum sheets with a thickness of 5 mm were used. The chemical composition of this alloy is given in Table 1. The dimensions of 6061 plates for the FSP experiments are illustrated in Figure 1a.

Table 1. Chemical composition of 6061 aluminum plates (wt%).

Al	Mg	Si	Cu	Fe	Mn	Cr	Zn	Ti
97.265	0.89	0.61	0.265	0.56	0.106	0.271	0.001	0.015



Fig. 1. FSW tools dimensions used in this study

SiC reinforcing particles with an average size of 5 microns were used in this study. To produce the composite by the FSP method, first, grooves were made with dimensions of 0.8mm width and 1.4mm depth in aluminum samples, and particles were embedded inside these grooves. The surface of the aluminum specimens was then sealed with a pinless tool to prevent reinforcing particles from escaping during the process. The FSP process was then performed using different input parameters to produce the composite.

To investigate the effect of tool pin shape on the distribution of reinforcing particles in the base metal, FSP tools with different pin shapes of triflate, cylindrical, threaded, triangular, square, and hexagonal were employed (Figure 1). Moreover, the pitch distance of the threaded pin profile tool was 1mm. 2344 steel was used to make the tools. After making the tools, the heat treatment process was performed.

The composite samples were polished and etched according to metallurgical methods to investigate their microstructural properties. Olympus optical microscope with 50, 100, 200, and 500x magnifications was used to examine the macrostructure and microstructure.

3. Simulation of friction stir processing

The FSP is simulated by the finite element method using Deform 3D software and based on the

Lagrangian method to predict the material flow in the stir zone [15, 16]. In order to simulate the material flow, it is necessary to introduce the properties of 6061 aluminum alloy in Deform software, which was selected from the Deform materials library. These properties include plastic, elastic, and thermal data, depending on the type of application. The plastic behavior of the samples is determined by the flow stress function or flow stress data. The current stress in this software is expressed for aluminum alloys under Eq. (1).

$$\bar{\sigma} = \bar{\sigma}(\bar{\varepsilon}, \dot{\bar{\varepsilon}}, T) \quad (1)$$

In this relation, $\bar{\sigma}$ is the stress flow, $\bar{\varepsilon}$ is the effective plastic strain, $\dot{\bar{\varepsilon}}$ is the effective strain rate, and T is the temperature.

The constant shear friction model was used for modeling friction between the FSP tool and the workpiece. The tool was meshed with about 7500 tetrahedral elements with an average size of 0.85 mm. The workpiece was also meshed with about 35,000 tetrahedral elements (Figure 2). The size of the elements in the workpiece is divided into three parts. The average size of the elements in part under the pin was considered 0.85 mm for contact accuracy. By moving away from the tool, the size of the elements was considered larger to reduce the process analysis time.

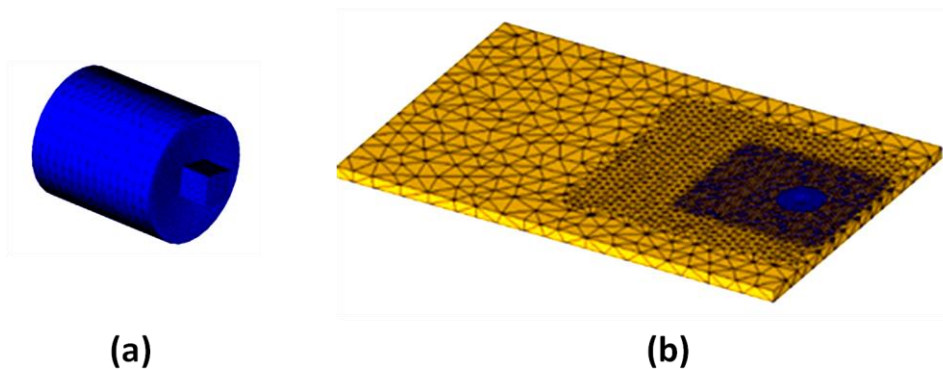


Fig 2. Meshed tool and workpiece.












4. Result and discussion

4-1- The effect of rotational and traverse speed

Table 2 shows the number of processed samples with different parameters. The results show that at rotational speeds higher than 1250 rpm, more heat is generated in the SZ, which leads to irregular material flow. At speeds below 1250 rpm, the heat generated is not sufficient to soften the stir zone material and

causes surface defects and tunnel cavities. Defects also occur at traverse speeds above 100 mm/min due to insufficient time to distribute the reinforcing particles. At traverse speeds below 100 mm/min, the heat generated increases, causing the material to overflow and causing cavities and tunnels in the processed zone. In this research, composite samples will be produced with a rotational speed of 1250 rpm and a traverse speed of 100 mm/min.

Table 2. Processed samples with different parameters

Pin shape	speed		Sample cross-section image	Defect	quality
	Rotational	Traverse			
Cylindrical	800	31.5		Hole	Defective
Cylindrical	1000	63.5		Hole	Defective
Cylindrical	1000	63.5		Hole	Defective
Cylindrical	1600	160		Hole	Defective
Cylindrical	1250	100		-	Sound
Triangular	1250	100		-	Sound
Triangular	1250	100		-	Sound
Hexagonal	1250	100		-	Sound
Triflate	1250	100		-	Sound
Threaded taper	1250	100		-	Sound
Threaded cylindrical	1250	100		-	Sound

4-2- Effect of tilt angle on defect formation

Tilt angle is one of the most influencing parameters on FSPed quality, such as mechanical and microstructural properties. Moreover, tool tilt angle has a significant effect on the heat generation and material flow and, as a result, the formation of defects such as tunnels and wormholes during the composite fabrication.

This parameter usually was selected in previous investigations without any investigation, and the optimum value of this parameter may not be used. In this study, to choose the proper value of tilt angle, three different values of 0, 2, and 3 degrees were numerically and experimentally investigated to produce composites (Figure 3).

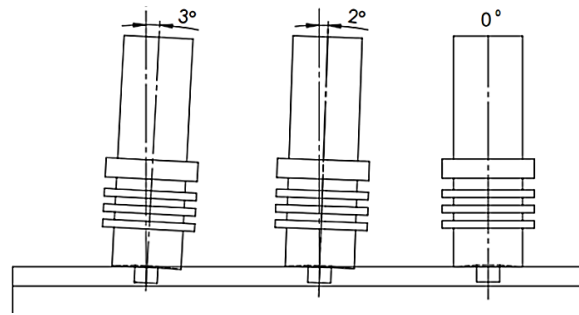


Fig 3. Different tilt angles used in this study

The simulation result of FSP using different tilt angles is shown in Figure 4. Using a tilt angle of 0° results in forming a large tunnel on the advancing side, as shown in this figure. The tunnel size is

decreased by increasing the tilt angle to 2° . As shown from this figure, no defect can be found by using a tilt angle of 3° .

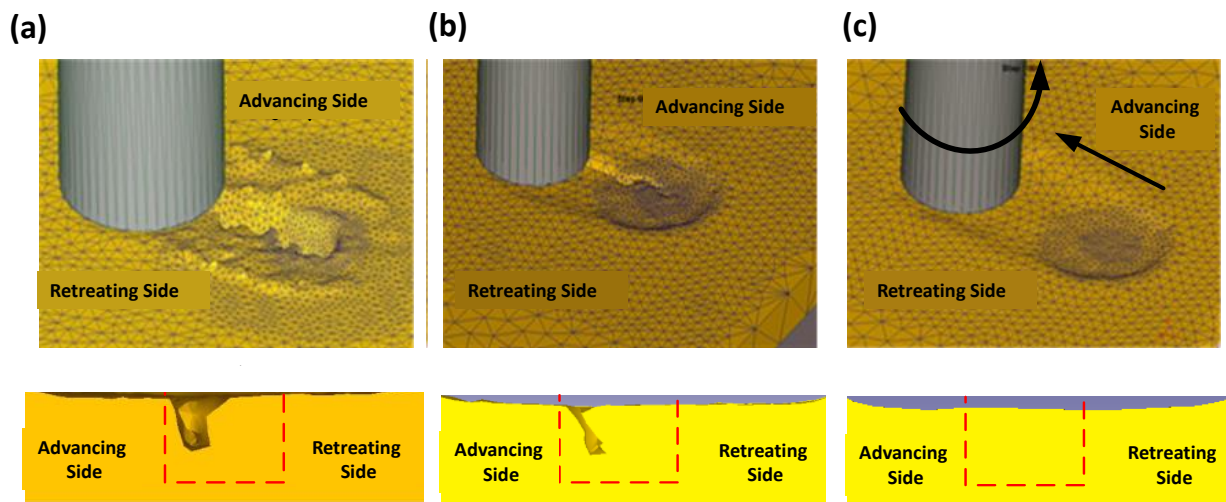


Fig 4. Simulation results of FSP by using different tilt angles at the surface of a workpiece

The experimental results of different samples proceed by different tilt angles are shown in Figure 5. As shown from this figure, numerical results are in good agreement with the experimental results. Moreover, the tilt angle of 3 results in the sound sample. When the tilt angle is zero, the material in contact with the tool shoulder flows in a direction parallel to the shoulder surface. However, a tilt given to the tool results in pushing the material downward from retreating to advancing side along the trailing edge due to the combined action of rotational and translational movement of the tool. This downward movement of material at the shoulder's trailing end

can be considered a forging action due to the tool tilt angle [17, 18].

An increase of tool tilt angle results in an increase of forging action on the trailing edge of the weld, thereby filling the cavities which otherwise remain at a lower tool tilt angle. Moreover, the increase in tool tilt results in reduced material to be transported from, leading to a trailing edge on the top material surface. There is a slight increase in temperature due to an increase in the plastic deformation heat associated with the forging action of the FSP tool. An increase in the temperature decreases the material's viscosity, leading to increased material flow moving with high velocity filling the surface defects.

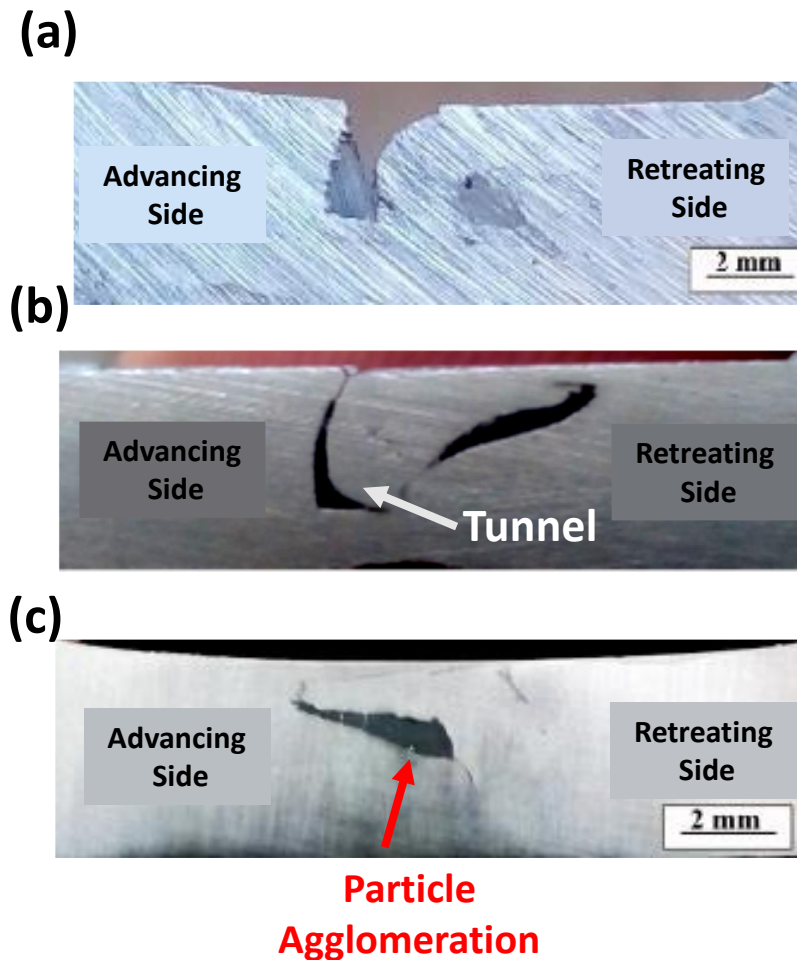


Fig 5. Experimental results of FSP by using different tilt angles of a) 0°, b) 2° and c) 3°

4-3. Effect of pin shape on particles distribution


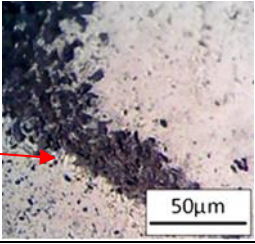

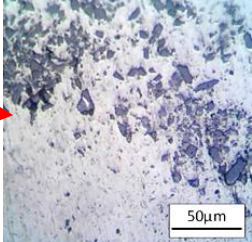

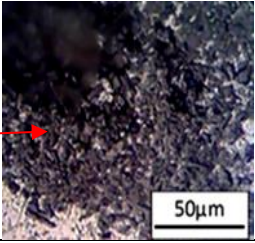
Non-uniform distribution of reinforcing particles in metal-based composites has significant effects on the failure characteristics and plastic deformation of composites. Uniform distribution of reinforcement in the metal matrix phase is one of the challenges encountered in metal matrix composite during processing which highly influences its strength. There are many parameters that constitute this issue; however, FSP pin shape is the most influencing factor in distributing particles. As a result, investigating the effect of pin profile on particle distribution seems crucial. To study the effect of pin shape and pass number on particle dispersion in the base alloy, a microstructural investigation was carried out.

Macroscopic and microscopic images of the FSPed sample fabricated by cylindrical pin profile are shown in Table 3. Samples were produced in one, two, and four pass processes. As shown in the table, the cylindrical tool could not disperse the reinforcing particles homogeneously in the base metal even after four passes. Reinforcing particles were agglomerated

mainly at the pin root in all samples, so a circular pin profile cannot distribute particles in the metal matrix. It can be concluded that cylindrical tools are not suitable tools for composite production using the FSP method.

In order to investigate the cause of the accumulation of reinforcing particles when using a cylindrical tool, the material flow during the process is modeled. Figure 6 shows the material flow during FSP. Several points are located along the centerline to study the dispersion of the reinforcing particles during the process. The results show that the material flow patterns at the upper and lower levels of the composite layer thickness were different. In this way, the material in part close to the shoulder due to more heat production became softer and had more material flow than the lower part of the stir zone. Therefore, the main driver of the material flow is the cylindrical tool. It is clear that due to the lack of oscillating mixing and the ability to move the material by the pin, the distribution of particles in the processing area is entirely irregular and accumulated.

Table 3. Macro and micro images of FSPed sample fabricated with circular pin profile

Pass number	Macroscopic image	Microscopic image
1		
2		
4		

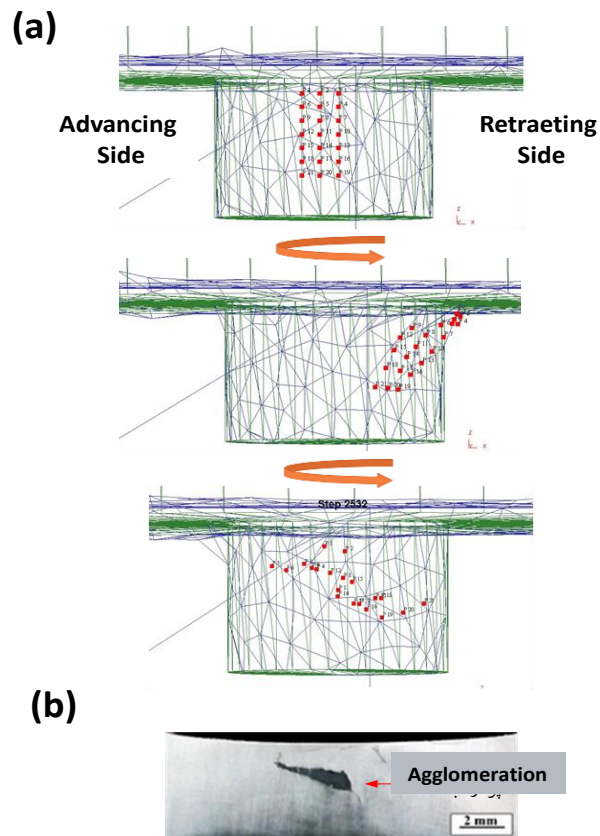


Fig. 6. a) The material flow during FSP using circular pin profile, b) Experimental particle distribution

Macroscopic and microscopic images of the FSPed samples fabricated by triangular pin profile are shown in Figure 7. The sample fabricated with one pass of the process shows the inhomogeneous distribution of particles in the metal matrix. By increasing the pass number, the distribution of particles in the metal matrix is enhanced. Moreover, FSPed samples were fabricated with and without changing the rotational direction between passes. As shown in Figure 7, the microstructural inhomogeneity is more evident in the FSPed samples fabricated without changing the tool rotational direction. The

reinforcing particles are mainly accumulated on the advancing side (AS), and the asymmetric distribution of particles around the SZ center can be seen. Change in the tool rotational direction between passes results in alteration of the location of the AS and RS together and consequently the material flow pattern, which improves the distribution of the particles. Moreover, the particles are not distributed near the plate top surface, and a bond with a very low percentage of particles can be found in this area that may be related to the absence of vertical material motion.

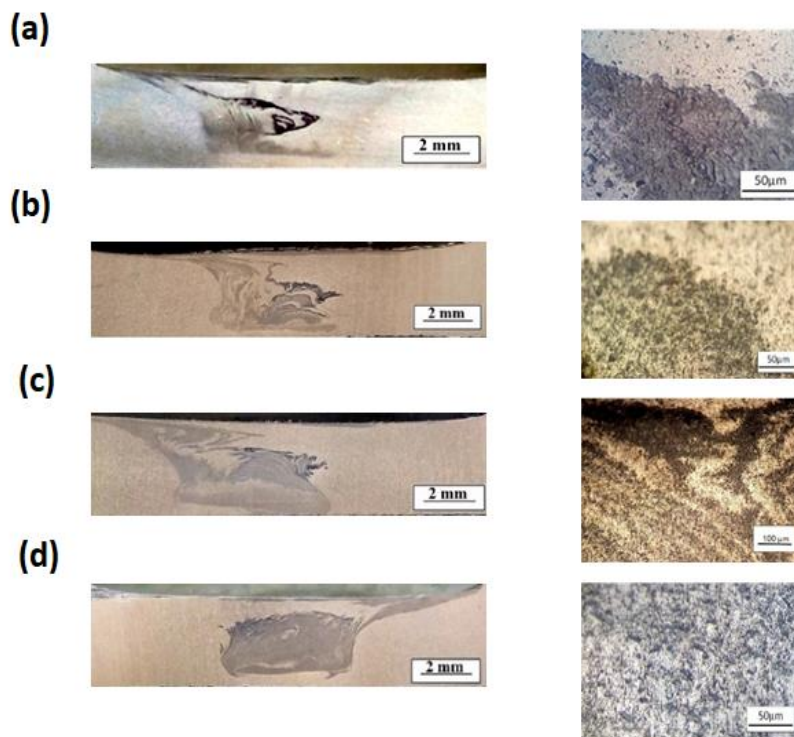


Fig. 7. Macro and micro images of FSPed sample fabricated with triangular pin profile at a) one pass, b) two passes, c) four passes, d) four passes with direction change

Macroscopic and microscopic images of samples fabricated by square pin profile are shown in Figure 8. Like the triangular pin profile, reinforcing particle distribution in the FSPed sample fabricated with four passes and with change in the rotational direction is the best. However, different bands involving different percentages of reinforcing particles were found in the SZ. Particle distribution is improved compared to cylindrical tools, which is due to the higher eccentricity and pulsation effect of the pin shape with a flat surface which increases the material flow.

Macroscopic and microscopic images of samples fabricated by hexagonal pin profile are illustrated in Figure 9. Reinforcing particles are distributed uniformly in the metal matrix in the FSPed sample fabricated with four passes with a change in the rotational direction. However, particles are not distributed uniformly in FSPed samples fabricated by one, two, and four passes without change in tool rotational speed.

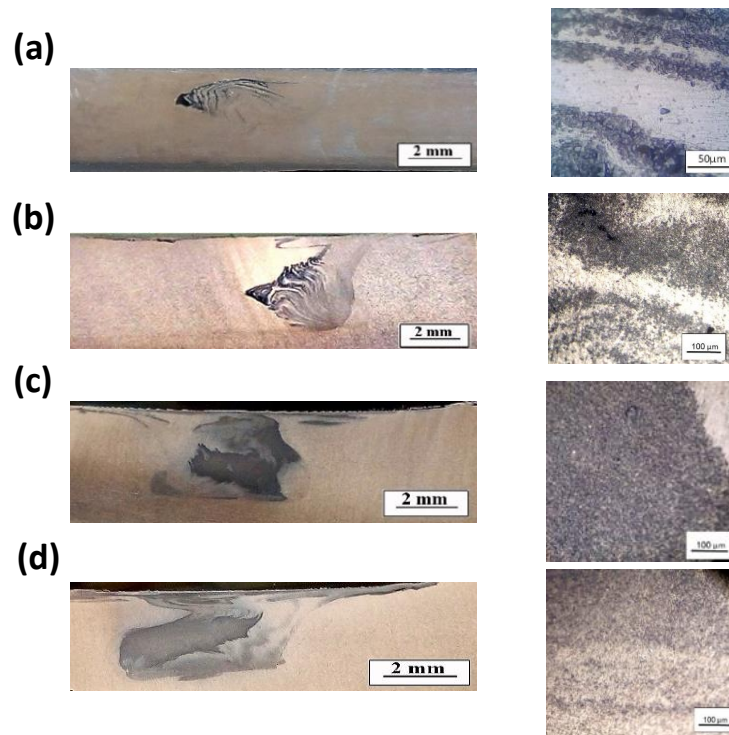


Fig. 8. Macro and micro images of FSPed sample fabricated with square pin profile at a) one pass, b) two passes, c) four passes, d) four passes with direction change

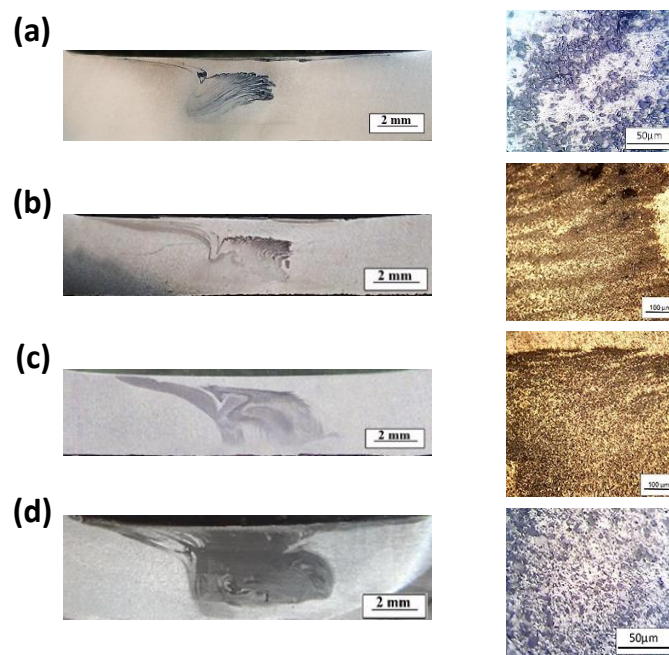


Fig. 9. Macro and micro images of FSPed sample fabricated with hexagonal pin profile at a) one pass, b) two passes, c) four passes, d) four passes with direction change

Macroscopic and microscopic images of workpieces fabricated by triflate pin profile are shown in Figure 10. The particle distribution of the FSPed sample fabricated with one pass is much better than circular, triangular, square pin profiles. The distribution of particles in the SZ in the FSPed sample fabricated by two passes is almost uniform. Moreover, increasing pass number or changing rotational direction has less

impact on particle distribution than other pin profiles. By changing tool rotational direction between passes or increasing passes from two to four, the particle distribution does not improve significantly. As a result, compared to hexagonal pin profile, using triflate pin leads to achieving uniform particle distribution at lower passes, leading to savings in time and cost.

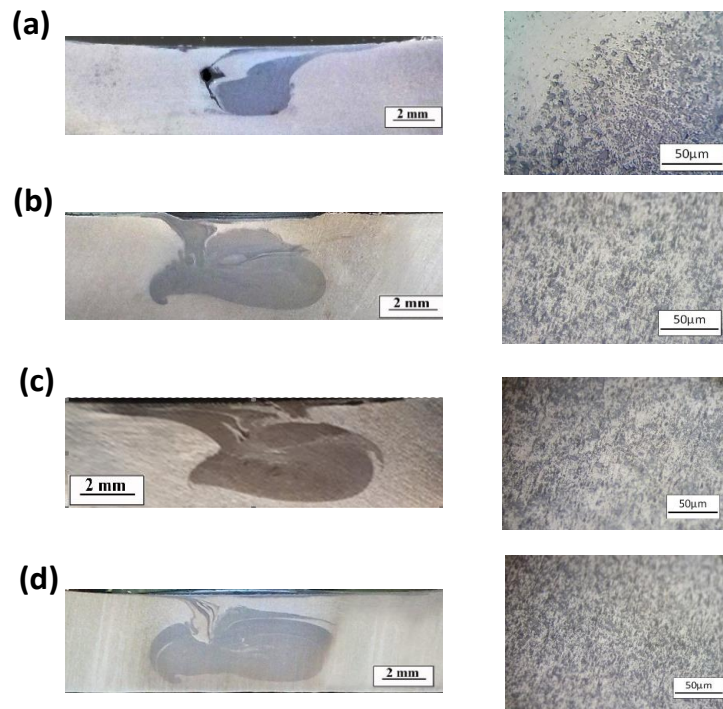


Fig .10. Macro and micro images of FSPed sample fabricated with triflate pin profile at a) one pass, b) two passes, c) four passes, d) four passes with direction change

Macroscopic and microscopic images of the workpieces produced by the threaded pin profile are shown in Figure 11. As shown from the table, excellent particle distribution is achieved by using a threaded pin profile. The patterns of material flow caused by threaded pin profiles are simulated numerically to consider the particle distribution pattern in the aluminum matrix (Figure 12). As can be seen from this figure, the particles, in addition to

rotating around the pin, also experience vertical motion due to the presence of a thread in the pin. This vertical motion eliminates the difference in the number of particles distributed in the different layers of the composite. Moreover, the threads of the tool also crush the reinforcing particles, making them more refined and preventing them from accumulating [13, 19, 20].

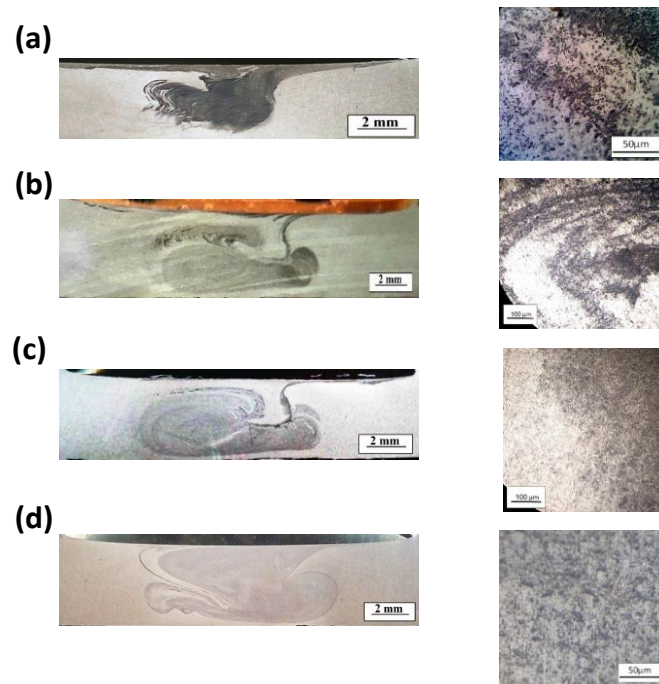


Fig. 11. Macro and micro images of FSPed sample fabricated with hexagonal pin profile at a) one pass, b) two passes, c) four passes, d) four passes with direction change

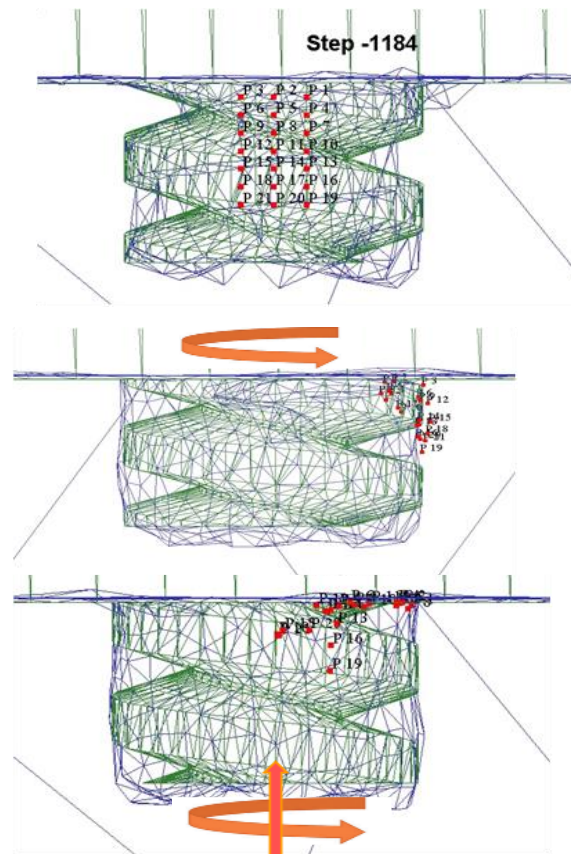







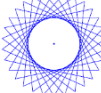








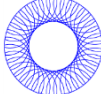


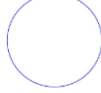
Fig. 12. the material flow during FSP using threaded pin profile

Tool pin profiles with flat faces, including triangular, hexagonal, square, and triflate pin profiles, are associated with eccentricity, which is defined as the ratio of the dynamic volume swept by the tool to its static volume. This ratio equal to 1, 2.41, 1.2, and 1.5 for triangular, hexagonal, square, and triflate, respectively (see Table 4), determines the direction of plasticized material flow from the advancing to the retreating side of the tool. In addition, the eccentricity of the pin shape is associated with dynamic orbit. The dynamic orbits of all pin profiles utilized in this study are demonstrated in Table 4. The pin profiles with flat faces produce a pulsating stirring action in the flowing material because of flat faces. As shown from the table, triangular, hexagonal, square, and triflate pin profiles produce 62.5, 125, 83.3, and 125 pulses/s when the tool rotates at a speed of 1250 rpm (Table 4). There is no such pulsating action in the case of cylindrical profiles. It illustrates that the pulsation effect of the hexagonal pin is severe than the square and the number of pulses generated by the hexagonal pin is 50% more than the square pin; however, the rotating arm is bigger for the square pin. As illustrated before, particle distribution in the FSPed sample fabricated with hexagonal pin profile is more uniform than square pin profile. This may show that the pulsation effect of the pin is dominated factor in distributing particles.

Moreover, the triflate pin profile has a higher dynamic to static ratio than the hexagonal pin profile, and the number of pulses made by both pin profiles is the same. Therefore, as stated before, FSPed fabricated with triflate pin profile could distribute particles uniformly at lower passes that may be due to higher dynamic to static ratio amount of triflate pin profile. As a result, in a pin with flat surfaces, two critical parameters influence the distribution of particles in the matrix (a) first, the pulsation effect of the tool is the most influential parameter, and (b) dynamic to static ratio.

As illustrated from the previous section, hexagonal, triflate, and threaded pin profiles are appropriate for distributing particles in the metal matrix by two different mechanisms. Comparing the threaded and hexagonal pin shapes, the revolving arm in the hexagonal pin is much bigger and is planer rather than threaded. However, it should be noticed that fine threads on a small scale cause higher material flow in the threaded pin. As a result, well particle distribution in metal matrix fabricated by the hexagonal and triflate pin is due to the pulsing effect of the flat surface, where the distribution of particles in metal matrix fabricated bay threaded pin profile is due to vertical motion generated by this pin profile.

Table 4. Impact of tool pin profile on perturbation area

Pin profile	Static Area (mm ²)	Area Occupied by the Pin in Dynamic Condition	Dynamic Area (mm ²)	Dynamic/Static	The portion of Dynamic Orbit	No. of pulses per second
	28.27		28.27	1		-
	11.7		28.27	2.41		62.5
	17.98		28.27	1.57		83.5
	23.38		28.27	1.2		125
	18.8		28.27	1.5		125
	25.5		28.27	1.1		-

5. Conclusion

In this research, the effect of pin shape on the distribution of reinforcing particles within the base metal during the production of composites by the FSP method is investigated. First, some experiments were performed to find the optimal parameters of rotational speed, traverse speed, and tilt angle. The results showed that 3-degree tilt angle, 1250 rpm rotational speed, and 100 mm/min linear speed could produce perfect samples. The results showed that the cylindrical tool was not able to distribute the particles evenly even after the fourth pass of the process. The square and triangular tools showed better powder distribution than the circular tools due to the edge surfaces of the pins. The triflate tool distributes the particle process evenly in the first and second passes, and this distribution does not improve much as the number of passes increases. Hexagonal and threaded tools in the fourth pass of the process evenly distribute the particles in the base metal. The distribution of particles using threaded and hexagonal tools in the fourth pass was better than the triflate tool, although the edge tool in the second pass compared to other tools after two passes had the best distribution process.

References

- [1] N. Kumar Maurya, M. Maurya, A.K. Srivastava, S.P. Dwivedi, A. kumar, S. Chauhan, "Investigation of mechanical properties of al 6061/sic composite prepared through stir casting technique", *Materials Today: Proceedings*, Vol. 25, No. 2020, pp. 755-758.
- [2] N.K. Chandla, Yashpal, S. Kant, M.M. Goud, C.S. Jawalkar, "Experimental analysis and mechanical characterization of al 6061/alumina/bagasse ash hybrid reinforced metal matrix composite using vacuum-assisted stir casting method", *Journal of Composite Materials*, Vol. 54, No. 27, 2020, pp. 4283-4297.
- [3] Z.Y.M. R.S. Mishra, I. Charit, "Friction stir processing: A novel technique for fabrication of surface composite", *Materials Science and Engineering*, Vol. A341, No. 2003, pp. 307-310.
- [4] R.S. Mishra, Z.Y. Ma, "Friction stir welding and processing", *Materials Science and Engineering: R: Reports*, Vol. 50, No. 1-2, 2005, pp. 1-78.
- [5] M. Akbari, P. Asadi, R.A. Behnagh, "Modeling of material flow in dissimilar friction stir lap welding of aluminum and brass using coupled eulerian and lagrangian method", *The International Journal of Advanced Manufacturing Technology*, Vol. 113, No. 3, 2021, pp. 721-734.
- [6] M.H. Shojaeefard, M. Akbari, P. Asadi, A. Khalkhali, "The effect of reinforcement type on the

- microstructure, mechanical properties, and wear resistance of a356 matrix composites produced by fsp", *The International Journal of Advanced Manufacturing Technology*, Vol. No. 2016, pp. 1-17.
- [7] K. Elangovan, V. Balasubramanian, "Influences of tool pin profile and tool shoulder diameter on the formation of friction stir processing zone in aa6061 aluminium alloy", *Materials & Design*, Vol. 29, No. 2, 2008, pp. 362-373.
- [8] H. Khodaverdizadeh, A. Heidarzadeh, T. Saeid, "Effect of tool pin profile on microstructure and mechanical properties of friction stir welded pure copper joints", *Materials & Design*, Vol. 45, No. 0, 2013, pp. 265-270.
- [9] G. Faraji, O. Dastani, S.A. Mousavi, "Effect of process parameters on microstructure and micro-hardness of az91/al₂O₃ surface composite produced by fsp", *J. of Materi Eng and Perform*, Vol. 20, No. 9, 2011, pp. 1583-1590.
- [10] M. Azizieh, A.H. Kokabi, P. Abachi, "Effect of rotational speed and probe profile on microstructure and hardness of az31/al₂O₃ nanocomposites fabricated by friction stir processing", *Materials & Design*, Vol. 32, No. 4, 2011, pp. 2034-2041.
- [11] Y.-h. Zhao, S.-b. Lin, L. Wu, F.-x. Qu, "The influence of pin geometry on bonding and mechanical properties in friction stir weld 2014 al alloy", *Materials Letters*, Vol. 59, No. 23, 2005, pp. 2948-2952.
- [12] V.M. Khojastehnezhad, H.H. Pourasl, A. Bahrami, "Estimation of mechanical properties of friction stir processed al 6061/al₂O₃-tib₂ hybrid metal matrix composite layer via artificial neural network and response surface methodology", *Proceedings of the Institution of Mechanical Engineers, Part L: Journal of Materials: Design and Applications*, Vol. No. 2021, pp. 14644207211034527.
- [13] M. Akbari, M.H. Shojaeefard, P. Asadi, A. Khalkhali, "Wear performance of a356 matrix composites reinforced with different types of reinforcing particles", *J. of Materi Eng and Perform*, Vol. 26, No. 9, 2017, pp. 4297-4310.
- [14] M. Akbari, P. Asadi, "Dissimilar friction stir lap welding of aluminum to brass: Modeling of material mixing using coupled eulerian-lagrangian method with experimental verifications", *Proceedings of the Institution of Mechanical Engineers, Part L: Journal of Materials: Design and Applications*, Vol. 234, No. 8, 2020, pp. 1117-1128.
- [15] G. Buffa, J. Hua, R. Shivpuri, L. Fratini, "A continuum based fem model for friction stir welding—model development", *Materials Science and Engineering: A*, Vol. 419, No. 1–2, 2006, pp. 389-396.
- [16] G. Buffa, J. Hua, R. Shivpuri, L. Fratini, "Design of the friction stir welding tool using the continuum based fem model", *Materials Science and Engineering: A*, Vol. 419, No. 1–2, 2006, pp. 381-388.
- [17] P. Chauhan, R. Jain, S.K. Pal, S.B. Singh, "Modeling of defects in friction stir welding using coupled eulerian and lagrangian method", *Journal of Manufacturing Processes*, Vol. 34, No. 2018, pp. 158-166.
- [18] N. Dialami, M. Cervera, M. Chiumenti, *Effect of the tool tilt angle on the heat generation and the material flow in friction stir welding*, ed., 2019,
- [19] M. Akbari, M.H. Shojaeefard, P. Asadi, A. Khalkhali, "Hybrid multi-objective optimization of microstructural and mechanical properties of b4c/a356 composites fabricated by fsp using topsis and modified nsga-ii", *Transactions of Nonferrous Metals Society of China*, Vol. 27, No. 11, 2017, pp. 2317-2333.
- [20] M. Akbari, M.H. Shojaeefard, P. Asadi, A. Khalkhali, "Wear and mechanical properties of surface hybrid metal matrix composites on al–si aluminum alloys fabricated by friction stir processing", *Proceedings of the Institution of Mechanical Engineers, Part L: Journal of Materials: Design and Applications*, Vol. 233, No. 5, 2017, pp. 790-799.